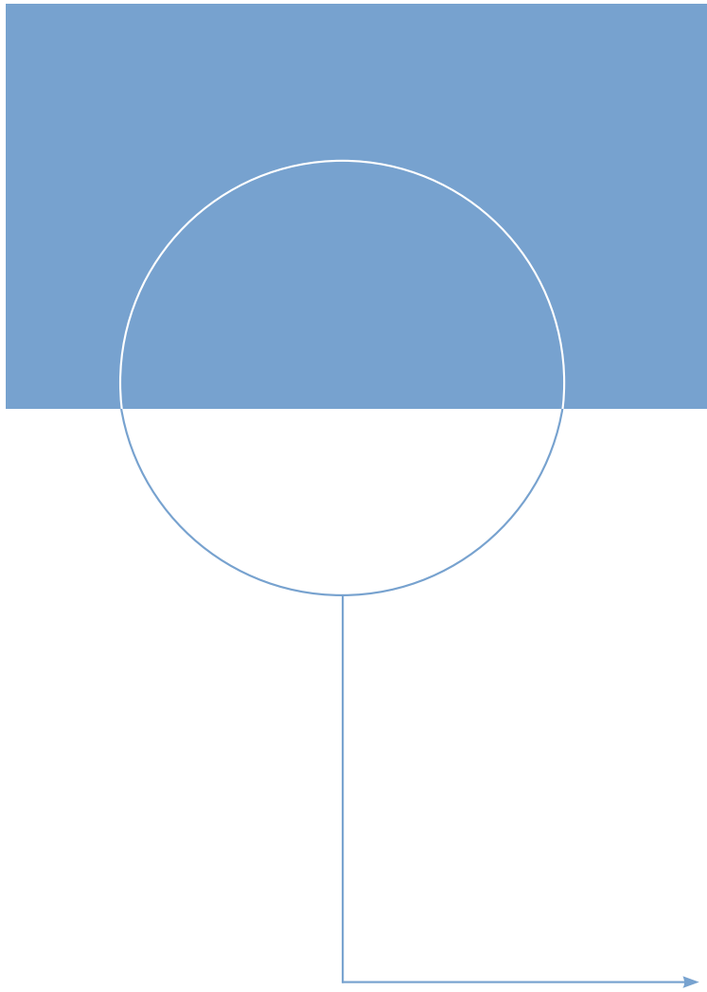

Master's thesis

2019

Emil Grove Dyrvik

NTNU
Norwegian University of
Science and Technology
Faculty of Natural Sciences
Department of Materials Science and Engineering

Emil Grove Dyrvik

Formation of Dislocation Arrays from CSL-type Grain Boundaries in Solar Silicon

June 2019

NTNU
Norwegian University of
Science and Technology

NTNU
Norwegian University of
Science and Technology

NTNU

Norwegian University of
Science and Technology

Formation of Dislocation Arrays from CSL-type Grain Boundaries in Solar Silicon

Emil Grove Dyrvik

Materials Science and Engineering
Submission date: June 2019
Supervisor: Marisa Di Sabatino Lundberg
Co-supervisor: Maria Tsoutsouva
Gaute Stokkan
Birgit Ryningen

Norwegian University of Science and Technology
Department of Materials Science and Engineering

Abstract

Solar photovoltaic energy is already one of the major renewable energy sources and is expected to be one of the most important energy technologies in a sustainable future. Solar cells based on multicrystalline silicon have been the market leader in recent years, but is facing tough competition and is now losing market shares. Improvements to efficiency and/or cost reductions are required for multicrystalline silicon to remain a competitive technology in the realm of photovoltaics.

The efficiency of a multicrystalline solar cell is governed by the quality of the multicrystalline silicon wafer it is based on. This wafer is cut from an ingot produced by a directional solidification process and the wafer quality is dependent on the presence of defects in the ingot from which it is cut, notably dislocations, grain boundaries and impurities. The formation of dislocations and grain boundaries can only be controlled through the solidification process. Thus, to achieve increased control over the presence of these defects, an increased understanding of the interplay between these defects during the solidification is required. The purpose of the work presented in this report is to further the understanding of how dislocation arrays are formed from certain types of grain boundaries.

In this work, 4 artificially grown coincidence site lattice grain boundaries have been inspected with regard to the electronic properties in the vicinity of the grain boundaries, the angular imperfection of the boundaries, and the evolution of dislocation arrays from the boundaries. The grain boundary types are the $\Sigma3\{1\,1\,1\}$, $\Sigma3\{1\,1\,2\}$, $\Sigma27\{5\,5\,2\}$, and $\Sigma27\{1\,1\,5\}$. The latter has been inspected more in-depth than the 3 former. The investigation techniques that have been used include lifetime mapping by microwave photoconductive decay, optical examination of the samples after defect-delineating etching, and orientation mapping by electron backscatter diffraction.

A strong correlation between reduced lifetime and the presence and extent of dislocation arrays was found. Although all samples exhibited a degradation and defect-presence along the grain boundary, it was much more pronounced for the $\Sigma27\{1\,1\,5\}$. Upon closer inspection of the $\Sigma27\{1\,1\,5\}$ specimen, the densely dislocated areas were found to be composed of an ensemble of subgrains. It appeared that the origin of the subgrains were dislocation arrays punched out from the centre grain boundary. These arrays were punched out at an angle and turned gradually more towards the vertical growth direction. The dislocation density was found to vary significantly between different subgrains but was relatively homogeneous within subgrains.

The evolution of the disorientation between the bulk of the two main grains in the $\Sigma 27\{1\,1\,5\}$ sample was probed as a function of the crystal height. However, it could not be decisively determined whether or not the disorientation evolved to become more ideal higher in the ingot.

Also the disorientation evolution of some small-angle grain boundaries and dislocation arrays was inspected. Where the disorientation was of a magnitude that could be detected, the disorientation remained essentially constant. The probed arrays that could be traced all the way to the centre grain boundary did not show any disorientation above the noise levels. It was assumed that these are developing small-angle grain boundaries that are in a too early stage to be detectable.

It was found that adjacent subgrains within a parent crystal seemingly share a direction of rotation relative to the parent crystal. A hypothesis has been put forward that this can be attributed to the origin of these dislocation arrays being the same or related, thus sharing the same Burgers vector. A potential cross-boundary dependency of the rotation of subgrains on the basis of the same hypothesis, due to either transmission of dislocations across the boundary or a relation between sites of origin, has also been discussed.

The local character of the grain boundary was found to be governed by the behaviour of the local subgrains on either side of the boundary.

Sammendrag

Fotovoltaisk solenergi er allerede en av de store fornybare energikildene og forventes å være en av de viktigste energiteknologiene i en bærekraftig fremtid. Solceller basert på multikrystallinsk silisium har vært en markedsleder de siste årene, men står overfor tøff konkurranse og mister markedsandeler. Forbedringer i effektivitet og/eller en kostnadsreduksjon er nødvendig for at multikrystallinsk silisium skal forbli en konkurransedyktig teknologi innen fotovoltaikken.

Effektiviteten til en multikrystallinsk solcelle avhenger av kvaliteten på den multikrystallinske silisiumwaferen som cellen er basert på. Waferen kuttes fra en ingot produsert ved rettet størkning. Waferkvaliteten avhenger igjen av tilstedeværelsen av defekter i ingoten den er kuttet fra – spesielt dislokasjoner, korngrenser og urenheter. Dannelsen av dislokasjoner og korngrenser kan kun styres gjennom størkningsprosessen. For å oppnå økt kontroll over disse defektene, er det derfor nødvendig med en økt forståelse av samspillet mellom disse defektene under størkningen. Hensikten med arbeidet som presenteres i denne rapporten er å forbedre forståelsen av hvordan samlinger av dislokasjoner dannes fra bestemte typer korngrenser.

I dette arbeidet har 4 fabrikerte korngrenser med sammenfallende gitterposisjoner (såkalt «coincidence site lattice») blitt inspisert med hensyn til de elektroniske egenskapene i nærheten av korngrensene, grensenes vinkelfeil og utviklingen av dislokasjonssamlinger fra grensene. Korngrensetypene er $\Sigma3\{1\,1\,1\}$, $\Sigma3\{1\,1\,2\}$, $\Sigma27\{5\,5\,2\}$ og $\Sigma27\{1\,1\,5\}$. Sistnevnte har blitt inspisert mer dyptgående enn de 3 førstnevnte. Undersøkelsesteknikkene som har blitt brukt inkluderer levetidskartlegging ved «microwave photoconductive decay», optisk undersøkelse av prøvene etter defektavdekking ved hjelp av etsing og orienteringskartlegging ved «electron backscatter diffraction».

En sterk sammenheng mellom redusert levetid og omfanget av dislokasjonssamlinger ble funnet. Selv om alle prøvene viste levetidsnedsettelse og nærvær av defekter langs korngrensen, var det mye mer utpreget for $\Sigma27\{1\,1\,5\}$. Ved nærmere inspeksjon av $\Sigma27\{1\,1\,5\}$-prøven ble det funnet at de tett dislokerte områdene var utgjort av en stor mengde subkorn. Det så ut til at opprinnelsen til subkornene var dislokasjonssamlinger sendt ut fra sentrumskorngrensen. Disse dislokasjonssamlingene var sendt ut i en vinkel og svingte gradvis mer mot den vertikale vekstretningen. Dislokasjonstettheten ble funnet å variere betydelig mellom forskjellige subkorn, men var relativt homogen innad i subkornene.

Utviklingen av disorienteringen mellom de to hovedkornene i $\Sigma27\{1\,1\,5\}$-prøven som en funksjon av krystallhøyden ble undersøkt. Det kunne imidlertid ikke påvises at disorienteringen

utviklet seg til å bli mer ideell høyere i ingoten.

I tillegg ble disorienteringsutviklingen av noen småvinkelkorngrenser og dislokasjonssamlinger inspisert. Der hvor disorienteringen var stor nok til å kunne detekteres, forble disorienteringen hovedsakelig konstant. De undersøkte dislokasjonssamlingene som kunne spores helt til sentrumskorngrensen, viste ingen disorientering over støynivåene. Det ble antatt at disse er begynnende småvinkelkorngrenser som er i et for tidlig stadium til å kunne påvises.

Det ble funnet at tilstøtende subkorn innad i en krystall tilsynelatende deler en rotasjonsretning i forhold til foreldrekrystallen. Det er blitt fremsatt en hypotese, som sier at dette kan tilskrives opprinnelsen til disse dislokasjonssamlingene, som enten er den samme eller er relatert til hverandre. Dermed har dislokasjonssamlingene samme Burgers-vektor. En potensiell mulighet for at denne rotasjonsavhengigheten av subkorn eksisterer på tvers av korngrenser, på grunn av transmisjon av dislokasjoner over grensen eller et slektsskap mellom dislokasjonenes opprinnelsessteder, har også blitt diskutert.

Den lokale karakteren til korngrensen ble funnet å være styrt av adferden til de lokale subkornene på hver side av grensen.

Preface

The original intention of this project was to utilise the capabilities of the Laue scanner to characterise a set of laboratory fabricated solar silicon samples. However, as the state of the Laue scanner – a tool specifically designed for orientation mapping of *large* silicon samples – continued to be 'out of order' throughout the project, the project itself turned more and more into an effort to make the best out of scanning electron microscopy-based electron backscatter diffraction (EBSD) – a technique excellent for orientation mapping smaller samples, but with quite a few limitations for larger specimens. A rather large portion of this report has therefore been devoted to discussing the hitches and hurdles encountered with EBSD, and how they best can be avoided for similar work in the future.

As the project progressed, I found many aspects of the experimental procedures that ideally should have been performed differently, despite my attempts at rigour. It would be interesting to redo some of the experiments in the light of this, but time was, as it always is, limited. Rather, I have painstakingly perpetuated the flaws through this report and will bring the lessons with me for future projects.

Although the work is qualitative in nature, I have tried to incorporate quantitative methods whenever possible, in order to give a better foundation for comparison of results. The work on the macroscopic disorientations and the work done on estimating measurement errors are the most obvious examples of this.

To reduce the risk of creating a too indecisive or too shallow report, a lot of experimental data gathered for completeness of the INSIDES project's data records has been left out. (This work is a part of the SINTEF-led INSIDES project.) Instead, an effort has been made to go into depth on one of the samples, and the majority of the report revolves around this particular sample. I am of the opinion that the scope of this project was too wide, making it difficult to dig deep enough or thoroughly enough to make any decisive conclusions in the end. The left out work has been briefly summarised in Appendix A.

It should be made clear that some of the work presented in this report was performed in the academic semester preceding the master project semester, during the course TMT4500 Specialization Project. For the experimental measurements, this concerns the microwave photoconductive decay measurements. For this report, several sections in Chapter 1 are either partly or largely based on sections written for the report submitted in that course, this goes for Sections 1.1, 1.2.1 to 1.2.3, 1.3, 1.4, 1.5.1 and 1.5.2, as well as Sections 2.1 to 2.3.

Acknowledgements

First of all, a round of thanks to my supervisors: To Birgit, Gaute and Maria for many good discussions; to Marisa, Maria and Birgit for comments on the manuscript; to Maria especially for all the help in the lab.

Plenty of hugs to Mattek class of '19 for five fantastic years of studying together, it has been an absolute blast. Also, a high five to everyone I shared the office with the last two semesters, for making every day a joy and filled with laughter. An extra shout-out to Bjørnar, Runar and Joakim for all the mischief we have managed – Notorious OCD, peace out.

Dedicated to my parents.

Abbreviations

µ-PCD microwave photoconductive decay

CI confidence index

CSL coincidence site lattice

EBSD electron backscatter diffraction

Fe iron

FZ float zone

GB grain boundary

HNO_3 nitric acid

HAc, CH3COOH acetic acid

HF hydrofluoric acid

HPMC-Si high-performance multicrystalline silicon

INSIDES IN-SItu characterisation and SImulation of Defect Evolution in Silicon

IPF inverse pole figure

IQ image quality

mc-Si, multi-Si multicrystalline silicon

mono-Si monocrystalline silicon

MSE mean squared error

NaN not a number

ND normal direction

PDG phosphorus diffusion gettering

PV photovoltaic

RAGB random-angle grain boundary

RD rolling direction

SAGB small-angle grain boundary

SEM scanning electron microscope

Si silicon

SRH Shockley-Read-Hall

SSE sum of square errors

TD transverse direction

Contents

1. Background

1.1. Introduction

As the world moves towards renewable and less carbon-intensive energy sources, solar photovoltaic (PV) energy is predicted to comprise a significant share of the world's energy supply in the decades to come, potentially providing a third of the world's electricity by 2050 [1], as illustrated in Figure 1.1. In the realm of renewables, solar PV already holds a position as one of the major technologies and has seen a rapid fall in costs of module production and installation in the recent years [2], implying that the industry will further bolster its position in the future.

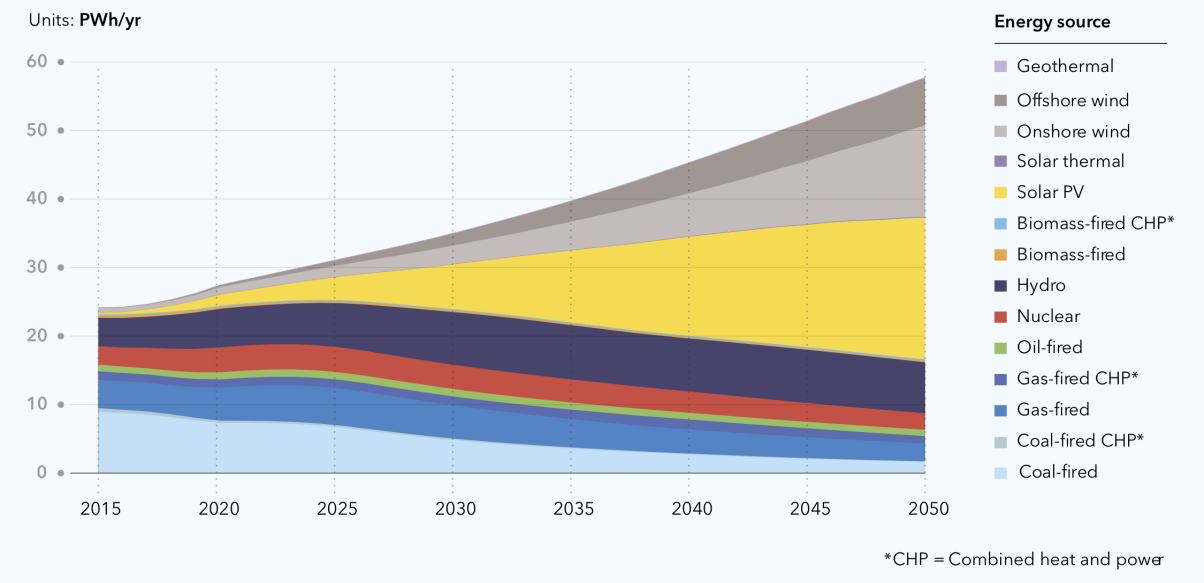

Figure 1.1.: Estimate of the world's global electricity production by generation type. From [1].

Today's PV market is dominated by silicon (Si) wafer technologies, with 95 % of the total module production [2]. Multicrystalline Si-based (mc-Si, multi-Si) modules have been the clear market leader since the start of the decade and supplied about 60.8 % of the estimated 97.5 GWp module production of 2017 [2], as shown in Figure 1.2. Steady improvements during the last decades have increased record conversion efficiencies of mc-Si cells to a current high of 22.3 % for laboratory cells and 19.9 % for modules [2]. The average efficiency of commercial mc-Si modules now lies close to 17 % [2]. However, due to improvements to monocrystalline Si (mono-Si) cell architectures, multijunction cells and novel thin-film chemistries – most notably

perovskites – further improvements to both conversion and cost efficiencies may be required to retain the leading position of mc-Si modules.

The most important factor for the efficiency of the final solar cell is the quality of the Si wafer that constitutes the majority of the cell structure and acts as the photoactive material. Conventionally, multicrystalline silicon ingots are produced by a directional solidification process, where the silicon melt is cooled from the bottom and multiple nucleation events take place. The grain boundaries (GBs) formed in this material may affect the material quality in a variety of ways, e.g. by affecting the formation, multiplication and movement of dislocations. Techniques have been devised to exploit or avoid these effects by controlling the crystallization process. In mono-like ingots, for example, where a mosaic of monocrystalline seeds are used to give a material with just a few, large grains and hence fewer GBs. The new industry standard, high-performance multicrystalline (HPMC-Si) ingots, is another example. Here, a fine-grained material is obtained and utilised to inhibit the movement and multiplication of harmful dislocation clusters [3].

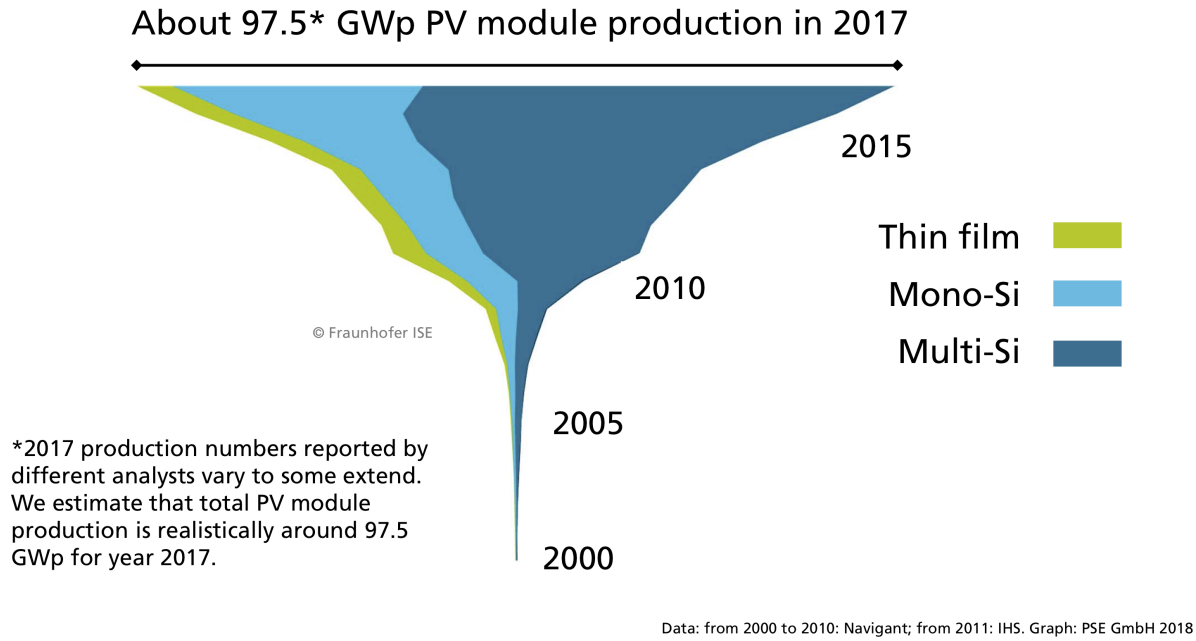

Figure 1.2.: Annual worldwide PV production by technology. From [2].

In order to further increase the quality of multicrystalline silicon material, a better understanding of how dislocations form and multiply in mc-Si is needed. This work seeks to further the current understanding by inspecting the artificially grown grain boundaries in four bicrystals. The bicrystals have been inspected with regard to the electronic properties in the vicinity of the grain boundaries, the angular imperfection of the boundaries, the evolution of dislocation arrays from the boundaries, and correlations therebetween. The work is part of the INSIDES project (IN-SItu characterisation and SImulation of Defect Evolution in Silicon).

1.2. Theory

1.2.1. Recombination in Semiconductors

The statements made in this section are summarised based on information found in [4].

A solar cell's ability at any given time to generate a photocurrent that is as high as possible, depends on the number of free charge carrier pairs and therefore the balance between the generation (increase) and the recombination (decrease) of these. Of particular interest for this work is the recombination, which is an electronic relaxation event causing the electron and the hole that constitute the charge carrier pair to recombine and become fixed in space. Recombination in semiconductors can occur by three main mechanisms: Radiative, Auger and Shockley-Read-Hall (SRH) recombination, as illustrated in Figure 1.3. SRH recombination mostly occurs due to material defects and imperfections, making the mechanism very sensitive to the processing quality of the Si material. It is the mechanism of interest for this work and therefore the only one to be further treated in this section.

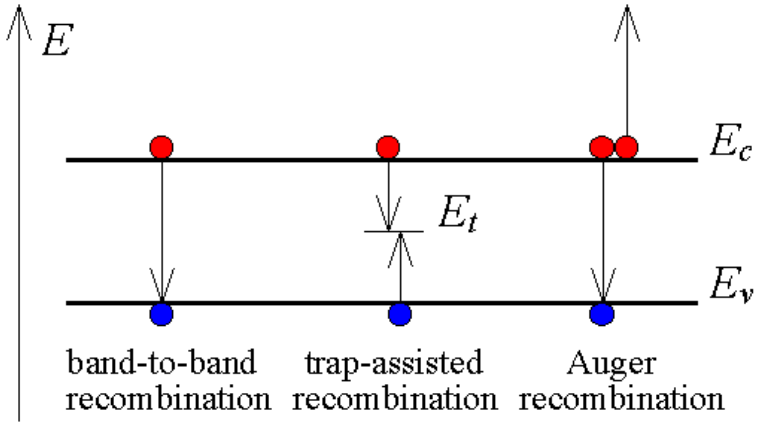

Figure 1.3.: The three types of recombination mechanisms, from left to right: Radiative, Shockley-Read-Hall, Auger. E_C is the conduction band and E_V is the valence band. From [5].

The SRH mechanism is non-radiative and is characterized by a relaxation through electronic trap states in the bandgap of the semiconductor. These trap states are spatially localized and may temporarily trap a free carrier at its locality until it is released again by thermal activation, or, the state may cause recombination by simultaneously trapping carriers of opposite polarities. Trap states tending to the latter scenario are typically called recombination centres and are associated with energies deeper into the bandgap, in comparison to electron or hole traps, which usually reside close to the conduction and valence band edges, respectively. Electron and hole traps have release times that are much shorter than the time required for the capture of the opposite carrier type.

For a single trap state at energy E_t, the net recombination rate at steady state is

$$U_{SRH} = \frac{np - n_i^2}{\tau_{n,SRH}(p + p_t) + \tau_{p,SRH}(n + n_t)}, \tag{1.1}$$

with n, p and n_i being the electron, hole and intrinsic carrier densities, respectively; n_t and p_t being the electron and hole densities when the electron and hole Fermi levels are equal to the trap level. $\tau_{n,SRH}$ and $\tau_{p,SRH}$ are the lifetimes for electron and hole captures by the trap. In doped material, Equation (1.1) simplifies to

$$U_{SRH} \approx \frac{n - n_0}{\tau_{n,SRH}} \tag{1.2}$$

and

$$U_{SRH} \approx \frac{p - p_0}{\tau_{p,SRH}} \tag{1.3}$$

for p- and n-type material, respectively, where n_0 and p_0 are the equilibrium carrier densities. I.e. the recombination rate is proportional to the excess minority carrier density. The electron and hole capture lifetimes of the traps are defined, respectively, as

$$\tau_{n,SRH} = \frac{1}{v_n \sigma_n N_t} \tag{1.4}$$

and

$$\tau_{p,SRH} = \frac{1}{v_p \sigma_p N_t}. \tag{1.5}$$

v_n, v_p are the mean thermal velocities of the carriers; σ_n, σ_p are the capture cross sections of the trap and N_t is the density of the trap states. It can be seen that an increase in N_t gives an increase in the recombination rate U_{SRH}, as would be expected.

1.2.2. Dislocations

The statements made in this section are summarised based on information found in [6, 7], except where otherwise stated.

Dislocations are one-dimensional defects in the crystal lattice and exist in two special cases: edge and screw dislocations. These are used to describe the general case: a mixed dislocation. An important property of a dislocation is its Burgers vector **b**. For an edge dislocation, **b** is normal to its line vector **t**, whereas **b** and **t** are parallel to each other for screw dislocations. For any given mixed dislocation, **b** may be at any angle to **t** and the length and direction of **b** is fixed, regardless of the position along the line.

Dislocations may move through two mechanisms, glide and climb. During glide, an edge dislocation moves in the plane spanned by its line and Burgers vectors. For screws, multiple planes are allowed, as **b** and **t** are parallel. However, the crystal structure normally restricts the motion to the crystallographic planes and directions allowing for the easiest dislocation

movement. These are termed the slip/glide planes and slip/glide directions. Slip directions are the directions within the slip plane associated with the shortest lattice vectors. Screw dislocations may move between multiple planes which both contain the direction of **b**, this is known as cross-slip and is illustrated in Figure 1.4. For diamond crystal structures, such as Si, the glide planes are $\{1\,1\,1\}$ and Burgers vectors of perfect dislocations are $\frac{1}{2}\langle 1\,1\,0\rangle$.

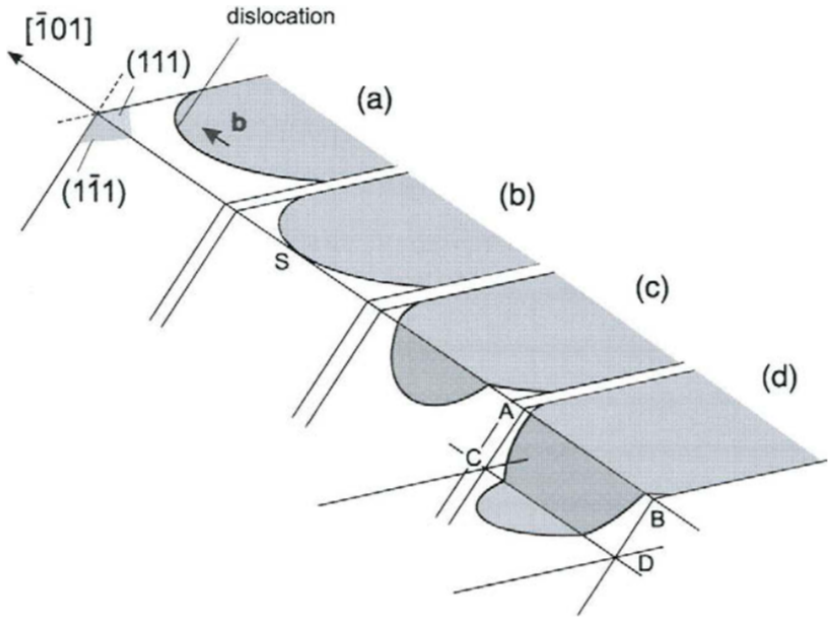

Figure 1.4.: A cross-slip event in fcc (a-c). Double cross-slip in (d). From [7].

Contrary to the glide, climb motion is not restricted to the glide plane, rather it occurs perpendicularly to **b**. It is a phenomenon based on emission and absorption of point defects at the dislocation line, typically vacancies, thus only being active at elevated temperatures where the required thermal energy for the activation of diffusion is available. During climb, steps in the dislocation line, called jogs, occur. The jog is essentially a step in which the dislocation is moved from one slip plane to an adjacent one. Similarly, steps that are contained in the slip plane are named kinks. **b** of jogs and kinks are the same as for their associated dislocation and are subject to the same rules for movement, thus they do not impede the glide characteristics, with an exception for jogs of screw dislocations. Jogs and kinks are illustrated in Figure 1.5.

For a dislocation to move, a force must be exerted on it. Forces on dislocations come in different forms, as the mechanisms of movement are different. Besides glide and climb forces caused by applied stress fields, a dislocation may experience chemical forces due to vacancies, as well as forces due to stress fields from other nearby dislocations or from a surface or interface. As a consequence of the strain they impose on the lattice, two dislocations may attract or repel each other. If the dislocations are of equal sign, they will cause excessive distortion of the lattice if close together, thus having an energetic gain by repelling each other, while dislocations of opposite sign will relax the surrounding lattice strain and may consequently attract and even

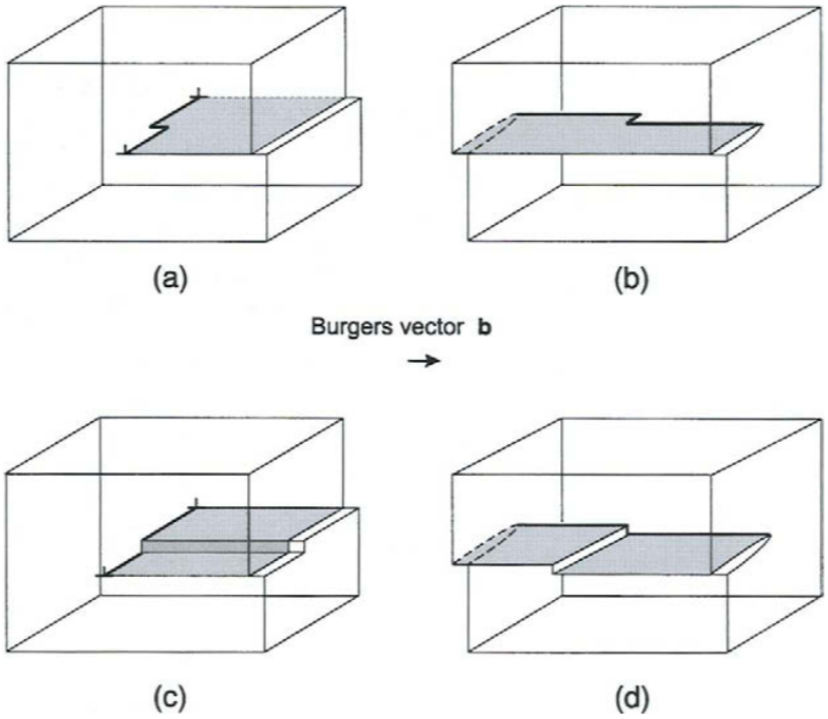

Figure 1.5.: Kink in edge dislocation (a), kink in screw dislocation (b), jog in edge dislocation (c), and jog in screw dislocation (d). From [7].

annihilate each other. A dislocation close to a non-rigid interface may be attracted to it due to the more compliant nature of the lattice in this region. The forces acting on the dislocation in such a case are called image forces, as an imaginary "image" of the dislocation on the opposite side of the interface is used in the associated calculations to fulfil the infinite-body boundary conditions. The solid-liquid interface may be an example of such an interface.

During crystal growth, dislocations may exist in a seed or surface that the crystal grows upon and continue into the newly crystallized region, or they may nucleate in the growing crystal. In the latter case, several mechanisms may be responsible for the nucleation. The three main mechanisms are impingement of growing interfaces, internal stresses due to e.g. thermal contraction or expansion, or collapse of vacancy platelets during cooling.

Additionally, existing dislocations can multiply by various mechanisms. One mechanism is the Frank-Read source, where a dislocation pinned in two ends may bow out under the application of a shear stress and create a dislocation loop. This process is regenerative, and the same source may create multiple loops. Another mechanism is the multiplication by multiple cross glide, wherein a dislocation loop cross glides between parallel glide planes, hence causing jogs that may act as Frank-Read sources for the remaining dislocation lines on both planes connected by the jogs. A third mechanism is the Bardeen-Herring source, which is similar to Frank-Read sources but operates by climb rather than glide.

Also grain boundaries may act as sources and emit dislocations into the grain. This may occur due to, for example, stress concentration at a ledge in the boundary caused by an adsorbed dislocation. Or, for small-angle grain boundaries, the dislocations making up the boundary may act as Frank-Read or Bardeen-Herring sources.

A dislocation in a crystal can be transmitted across a grain boundary into an adjacent crystal. In such a case, the Burgers vector in each crystal can be different, but the net vector is conserved by leaving a grain boundary dislocation [8]. This is summarised in Equation (1.6), where superscripts indicate the location of $\mathbf{b}$ (crystal 1 or 2, or the grain boundary (g)).

$$\mathbf{b^{(1)}} \rightarrow \mathbf{b^{(g)}} + \mathbf{b^{(2)}} \tag{1.6}$$

1.2.3. Misorientations and Grain Boundaries

1.2.3.1. Misorientations

With an orientation $\boldsymbol{O}$, which corresponds to a rotation that maps coordinates from a crystal coordinate system to a reference coordinate system, there is also a class of symmetrically equivalent orientations $\boldsymbol{OS}$ with respect to the symmetry group S [9]. The misorientation between two orientations $\boldsymbol{O_1}$ and $\boldsymbol{O_2}$ is defined as $\boldsymbol{O_1^{-1}O_2}$. With $\{\boldsymbol{S_1}, \boldsymbol{S_2}\} \in S$, there is a class of symmetrically equivalent misorientations $\boldsymbol{S_1^{-1}O_1^{-1}O_2S_2}$ [9]. The misorientation exhibiting the smallest rotational angle of a class of misorientations is sometimes termed the disorientation [9, 10] – this nomenclature will also be used throughout this work. Notation-wise, misorientations will be denoted by angles θ_k (around axes $\boldsymbol{\eta_i}$), while disorientations will be described by a disorientation angle δ (around a disorientation axis $\boldsymbol{\eta_d}$). Vectors and axes in bold text are distinguished from orientations in bold and italicised text.

1.2.3.2. Grain Boundaries

Grain boundaries are defined by a boundary plane and a smallest rotation around a specific axis that would transform the orientation of one of the grains to the orientation of the other, analogous to the above-stated definition of the disorientation.

GBs with relatively small disorientations are suitably termed small-angle grain boundaries (SAGBs), low-angle grain boundaries or subgrain boundaries. These can be considered as rows of dislocations which lie at intervals proportional to the disorientation angle along the boundary, as sketched in Figure 1.6. Grains that are primarily bounded by SAGBs to a larger grain of almost the same orientation are termed subgrains. Typically, GBs with disorientations below 10° to 15° are considered SAGBs, however, there is no clear definition.

At disorientations above 15°, rows of dislocations no longer give a purposeful description of the GB, as dislocations would be overlapping [10]. These boundaries will in this work generally be referred to as random-angle grain boundaries (RAGBs). In literature, they are also frequently referred to as large-angle grain boundaries or high-angle grain boundaries.

There exists a special case of high-angle grain boundaries that exhibits symmetry properties which give rise to overlapping lattice points between the two crystals lattices. These boundaries may be described by the frequency of overlapping lattice points. The array of overlapping lattice positions defines itself a lattice, termed the coincidence site lattice (CSL). A CSL boundary has an index value Σ which denotes the frequency of overlapping points. Σ is defined as the unit cell volume of the CSL in units of the unit cell volume of the elementary cells of the crystals [6]. A $\Sigma 5$ CSL boundary is sketched in Figure 1.7. The Σ-notation will be used to distinguish these from general RAGBs.

CSL boundaries are associated with an exact disorientation angle. However, real crystals will not always make a perfect overlap of lattice points. In these circumstances, grain boundary dislocations may accommodate for the deviation in disorientation angle and preserve the properties of the CSL boundary [10]. Tolerance criteria have been defined in order to classify real GBs as CSL boundaries. A common criterion is the Brandon criterion, which states that a GB is a CSL boundary of index Σ if its disorientation δ is within a

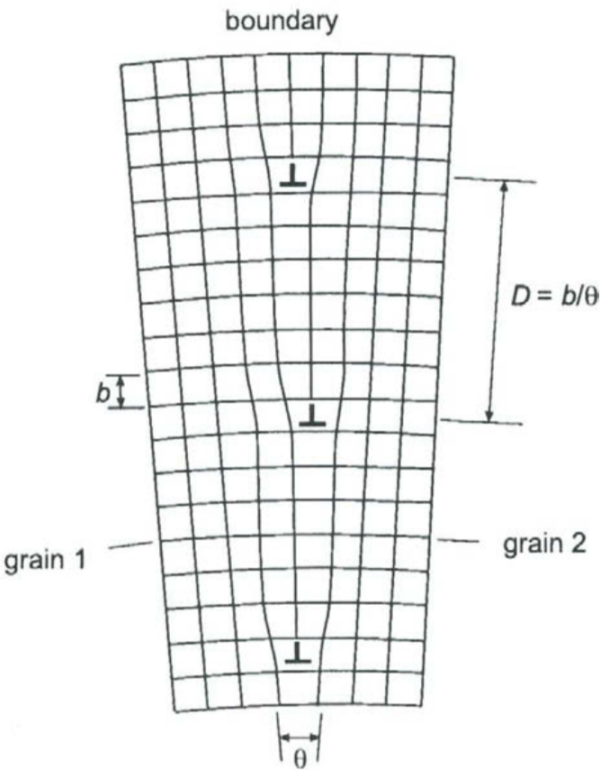

Figure 1.6.: A schematic of a symmetrical pure tilt small-angle grain boundary displaying how the GB may be described as an array of dislocations. From [7].

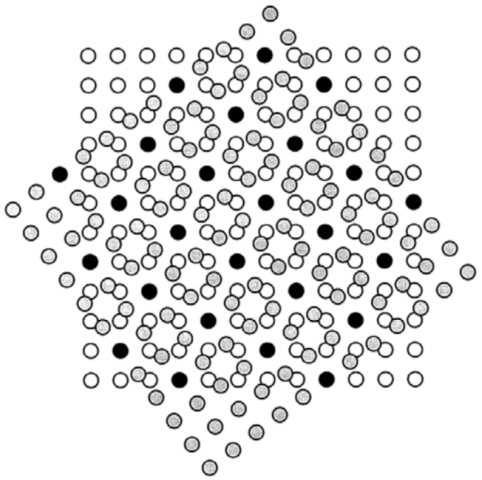

Figure 1.7.: A schematic of $\Sigma 5$ CSL. White and grey circles represent the two lattices, while common lattice sites are dark and make up the CSL. From [10].

tolerance limit $\Delta\delta$ of the disorientation associated with the CSL Σ given by

$$\Delta\delta = 15^\circ \times \Sigma^{-1/2}. \tag{1.7}$$

In this thesis, a notation stating first the *Σ index value*, then the *boundary plane family* of the GB will be used. E. g. $\Sigma3\{1\,1\,1\}$. Some CSL boundaries in the diamond crystal structure that are of particular interest to this work are: The $\Sigma27a\{5\,5\,2\}$ and $\Sigma27a\{1\,1\,5\}$, which exhibit a 31.59° tilt around the $\langle1\,1\,0\rangle$ axis [11]; the first order twin, $\Sigma3\{1\,1\,1\}$, corresponding to a 60° twist around $\langle1\,1\,1\rangle$ or a 70.53° tilt around $\langle1\,1\,0\rangle$ [11]; the $\Sigma3\{1\,1\,2\}$, also corresponding to a 70.53° (or 109.47°) tilt around $\langle1\,1\,0\rangle$ [11]. Additionally, attention is made to the $\Sigma19a\{1\,1\,6\}$, described by a 26.53° tilt around $\langle1\,1\,0\rangle$ [12]. From now on, the *a* will be omitted when referring to the $\Sigma27a$ and $\Sigma19a$ boundaries, because the *b*-system will not be treated, it is therefore implicit that it is referred to the *a*-system boundaries.

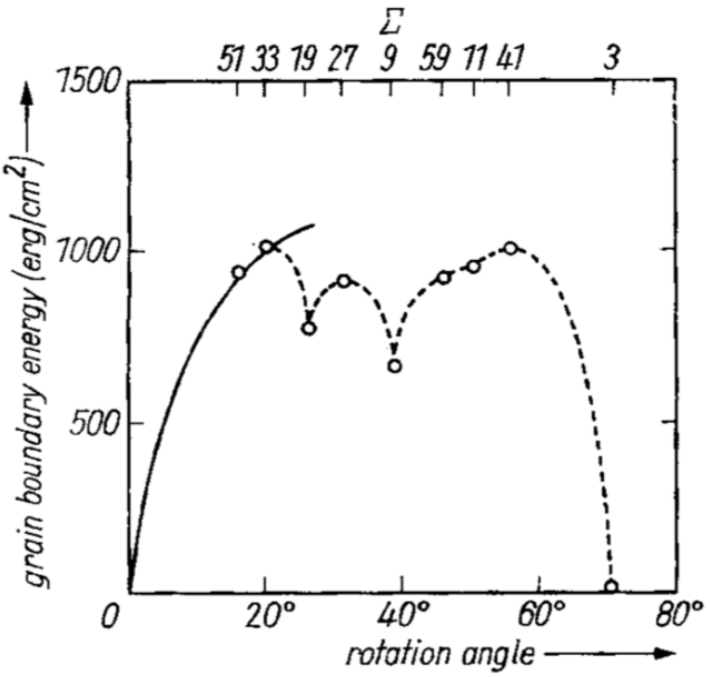

Figure 1.8.: Calculated grain boundary energy as a function of disorientation angle around $\langle1\,1\,0\rangle$ in the range 0° to 70.53°. From [11].

The stability of a GB is determined by its grain boundary energy, which depends on the disorientation between the grains and the CSL symmetry. In Figure 1.8 it can be seen that certain CSL boundaries create local minima in the energy. $\Sigma3\{1\,1\,1\}$ boundary is by far the most stable. The $\Sigma27\{5\,5\,2\}$ lies relatively high, whereas $\Sigma19$ is favourably positioned in a cusp. The energy of $\Sigma3\{1\,1\,2\}$ is not included but has been calculated to be quite high [11]. The energy of the $\Sigma27\{1\,1\,5\}$ has not been calculated.

1.3. Implications of Dislocations in Solar Silicon

Dislocations are always present in multicrystalline silicon, however, the dislocation density may vary over several orders of magnitude from grain to grain. Typical densities are in the range $10^2\,\mathrm{cm}^{-2}$ to $10^7\,\mathrm{cm}^{-2}$ [13]. Models show that the diffusion length decreases with densities above $10^4\,\mathrm{cm}^{-2}$, being more than halved for densities above $10^6\,\mathrm{cm}^{-2}$ [14].

The dislocations may be of various types, many of which have a geometry that makes it energetically favourable with a reconstructed dislocation core, rather than dangling bonds. When these dislocations are clean from impurities or other defects, they form shallow, one-dimensional bands in the bandgap, which do not cause recombination to any noteworthy extent [13], see Figure 1.9. However, the presence of additional defects may cause localised, deep states in the bandgap, which are also observable in Figure 1.9. Deep states are much more likely to act as trap states and be deleterious to minority carrier lifetimes. Such defects may be, for example, dangling bonds in an insufficiently reconstructed dislocation core, or contaminating impurities in the vicinity of the dislocation. The electronic energy levels of an impurity depend on the location of the impurity and may be different for an impurity at a dislocation compared to one in the bulk. Thus, the effect of impurities on the minority carrier lifetime will depend on the dislocation density of the material [13].

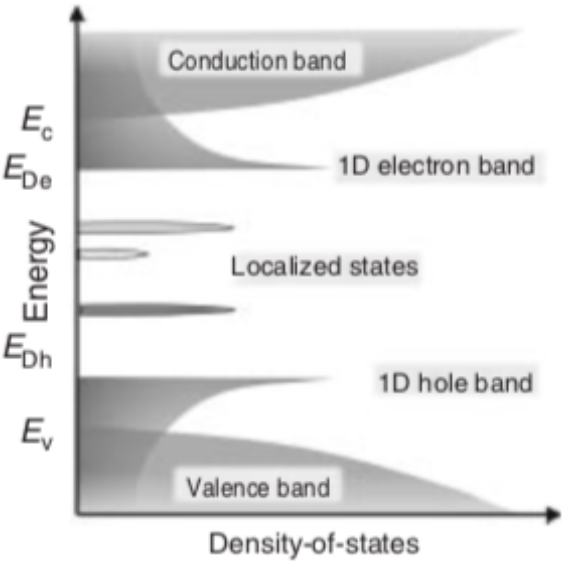

Figure 1.9.: A schematic of the density-of-states for a dislocation. Shallow 1D bands due to lattice deformation from a clean dislocation. Localised deep states due to impurities and dislocation core defects. From [13].

Multicrystalline silicon processing for photovoltaic applications involves external gettering (normally by phosphorus diffusion gettering (PDG)), wherein impurities are moved from the active part of the device, for instance, the p-type bulk, to an inactive part of the device, such as the n-type emitter. Gettering has been found to have a significantly larger, positive effect on the lifetime in areas with low defect densities and high lifetimes already prior to PDG, compared to the effect in areas with higher defect densities and poor lifetimes [15]. This is attributed to internal gettering of transition metal impurities at dislocations and other structural defects [15], thus preventing external gettering in these areas.

It is evident that the presence of dense dislocation clusters in multicrystalline solar silicon material is undesirable, and significant improvements to cell efficiency may be achieved if the formation of such clusters can be avoided.

1.4. Literature Study: Microstructure and Dislocations in Multicrystalline Silicon

Microstructure in multicrystalline silicon and its effect on solar cell efficiency have been investigated by various groups. A selection of works related to the origin of dislocation clusters and arrays will be summarized in this section.

Sopori et al. (1998) [16] found a presence of defects clusters consisting of long, intertwined dislocation loops in some grains in multicrystalline material of otherwise high quality. This was attributed to these grains being oriented with slip planes and directions along stress axes during crystal growth, resulting in deformation and defect formation of said grains when the plastic yield stress was exceeded while relieving stress in the remainder of the ingot. Network modelling indicated that such defect clusters act as shunts, lowering the open-circuit voltage V_{oc} and fill factor FF of a solar cell.

Later, Ryningen et al. (2011) [17] followed dislocation clusters along the height of a wafered, pilot-scale ingot. The clusters were observed to originate at grain boundaries. The behaviour of a Σ27a boundary is described in particular detail. This boundary was observed to grow approximately at a 20° angle to the macroscopic growth direction, spawning multiple dislocation clusters throughout the ingot height. The clusters could be seen to grow in size and dislocation number as a function of height above the point of origin. They propose that the dislocations may multiply by means of a Frank-Read source while following the solid-liquid interface during crystal growth.

Ervik et al. (2011) [18] also studied the dislocation formation from a Σ27a boundary. They found that the boundary dissociated into a structure of triangular grains formed by one Σ3 and two Σ9 boundaries. One of the Σ9 boundaries was found to be asymmetric, and this boundary dissociated further into two Σ3 boundaries. Arrays of dislocations had been formed from the junction between the symmetric and asymmetric Σ9s, as well as from the junction where the asymmetric Σ9 further dissociated. They attributed this behaviour to high boundary energy causing the Σ27 type boundaries to be unstable. They also observed the dissociation behaviour to depend on the angular deviation from exact coincidence, where Σ27 GBs with high coincidence would be straight and less decorated by dislocations. Also Garg et al. (1998) [19] observed the dissociation of a Σ27{5 5 2} boundary into Σ9 and Σ3 boundaries, while Stoffers (2017) [20] observed a Σ27a boundary by high-resolution high-angle annular dark-field scanning transmission electron microscopy and found it to be completely dissociated into periodic arrangements of one Σ9 and two Σ3 boundaries.

Oriwol et al. (2013) [21] examined SAGBs in mc-Si by synchrotron white-beam x-ray topography. They were able to identify SAGBs with disorientations between 0.07° to 0.80° and the disorientation was found to increase with the height in the ingot. They propose a mechanism for the dislocation pile-up where dislocations are generated at a GB near the solid-liquid

interface as a result of thermo-mechanical stresses and subsequently agglomerate to constitute dislocation walls which may form subgrain boundaries which grow in the growth direction. The end result is a cellular structure in the wafer surface where the dislocations are arranged in SAGBs. Further, they describe the mechanism to result in a structure that looks pillar-like in the vertical cross-section, with subgrains of increasing rotation relative to the primary grain orientation and rotation axis parallel to the growth direction. Carl et al. (2014) [22] also studied the evolution of SAGBs by synchrotron white-beam x-ray topography and found that the larger SAGBs would increase in dislocation density at the expense of smaller SAGBs.

Similarly to [17], Stokkan et al. (2014) [23] investigated the evolution of dislocation clusters in HPMC-Si by tracing clusters in wafers along the height of an industrially produced ingot. CSL type boundaries, notably $\Sigma 27$, were also in this work observed in the presence of dislocation clusters. Moreover, RAGBs were found to terminate existing clusters. This effect was found to be more pronounced in the lower parts of the ingot, where the grain size was smaller compared to in the higher parts.

More recently, Trempa et al. (2017) [24] studied the evolution of grain structure and dislocations in extraordinary tall ingots of both HPMC-Si and conventional mc-Si. They found that with the height in the ingot, most measurables converged to the same values for HPMC-Si and conventional mc-Si. Usually, convergence occurred at heights between 200 mm to 400 mm from the bottom. Such measurables included mean grain size, grain size variability, grain orientation distribution, grain orientation variability, grain boundary type distribution and recombination active area. Interestingly, recombination active area peaks at very high levels in the lower parts of the conventional mc-Si, before declining to the level of convergence, whereas recombination active area in the HPMC-Si displays a steady increase from very low levels until convergence. For the HPMC-Si, this seemingly correlates with the gradual decline in RAGBs and increase in grain sizes. In the conventional case, dislocation cluster growth is presumably permitted at early stages of ingot growth due to the much larger grain sizes in the ingot bottom than for the HPMC-Si, and the low amount of RAGBs. Also in this case, convergence seems to correlate with the evolution of grain sizes and grain boundary types.

Chuang et al. (2018) [25] observed the formation of SAGBs by in-situ microscopy during solidification of unseeded material. SAGBs were observed as lines almost perpendicular to the solid-melt interface and propagated in the growth direction. Post-mortem examinations of the in-situ observed SAGBs showed that the dislocations aggregated into linear arrangements which at the beginning appeared wavy, but subsequently grew in relatively straight lines. In the straight lines, individual dislocations could not be distinguished. Some of these dislocation walls would terminate in the crystal and some would make up SAGBs. The disorientation of the SAGBs was found to increase along the length of the SAGB. They argue that if the relationship d/D is sufficiently small, where d is the average interval between intrinsic dislocations in an array and

D is the average dislocation spacing of evenly distributed dislocations in a grain, the energetic configuration of the dislocations may be more favourable when situated in an array than freely in the lattice. Additionally, they argue that the elevated temperatures close to the solid-liquid interface provides good conditions for both slip and climb motion of the dislocations.

1.5. Experimental and Mathematical Techniques

1.5.1. Microwave Photoconductive Decay

The statements made in this section are summarised based on information found in [26].

Microwave photoconductive decay (µ-PCD) is a technique used to determine the excess carrier lifetime of a semiconducting sample. Instruments used for µ-PCD are equipped with a microwave source, microwave detector and a light source. A continuous microwave with power P is generated and directed towards the semiconducting sample where it is partially reflected. The difference in power ΔP of the reflected wave in comparison to the incident wave is related to the conductivity σ through

$$\frac{\Delta P}{P} \propto \sigma, \tag{1.8}$$

where the conductivity is proportional to the excess carrier density and therefore decays with the same time constant τ:

$$\sigma(t) = \sigma(0)\exp(-t/\tau). \tag{1.9}$$

Thus yielding a possibility to determine the excess carrier lifetime from the decay rate of the conductivity. Combined with a localised light source and scanning functionality, spatially resolved lifetime maps may be obtained.

1.5.2. Sopori Defect Etching

Dislocations and other defects in silicon crystals, for example, grain boundaries, may be inspected by means of the etching of a polished crystal. The etch rate at the site of a defect differs from the rate at a location of locally ideal crystallinity and, as a result, a distinct topography is obtained. This makes defects visible as etch pits and etch grooves when viewed in an optical microscope [6].

For efficient delineation of defects in multicrystalline Si, the etchant must act isotropically, making defects in all orientations visible and similar in size. Furthermore, it should be possible to determine the defect propagation direction from the appearance of the etch pit, such as to indicate the origin and nature of the defect. Also, etch rates should be practically high and the etchant should not leave any contamination of the surface or the bulk material [27].

The Sopori etch is specifically made for the purpose and adheres to these requirements. The original version created by Sopori [27] consists of 36 parts 49% hydrofluoric acid (HF), 20

parts undiluted acetic acid (HAc, CH3COOH) and 1-2 parts 70% nitric acid (HNO_3). Whereas HNO_3 and HF both play important roles in the etching mechanism, HAc is only a solvent. HNO_3 serves to oxidise the Si, making it susceptible to the HF, which effectively dissolves the oxide [28]. The mechanism is, therefore, an indirect one. In the Sopori etch, the etch rate is determined by the concentration of HNO_3, i.e. by the oxidation rate [27].

1.5.3. Electron Backscatter Diffraction

Electron backscatter diffraction (EBSD) is a characterisation technique used in conjunction with a scanning electron microscope (SEM). It enables investigation of details about the crystal structure, such as crystal orientations, deformations, and phase determination with high spatial resolution. The spatial resolution is ultimately limited by the excitation volume in the sample and can be well below 0.1 µm for certain materials [29].

The backscattered electrons from the interaction between the electron beam and the sample are used as the source of information for the EBSD signal. These are electrons that are scattered elastically by interaction with an atomic nucleus and retain most of their high energy. If the incident electron is subjected to one or more of these scattering events and leaves the sample from the same surface as it entered, it is backscattered [30].

Interference between electrons scattered on a set of lattice planes in positions fulfilling Bragg's law creates two diffraction cones around the diffracting planes. As the opening angles of the cones are very large, the intersections of the two cones with the detector plane forms two (approximately) straight lines which together give rise to what is called a Kikuchi-band. Figure 1.10 shows a pattern of Kikuchi-bands (a) and a schematic of the formation of the bands (b).

The set of diffracting lattice planes are represented by a normal vector **g**. In order to make an indexation of the orientation of the crystal in a probed sample volume, the

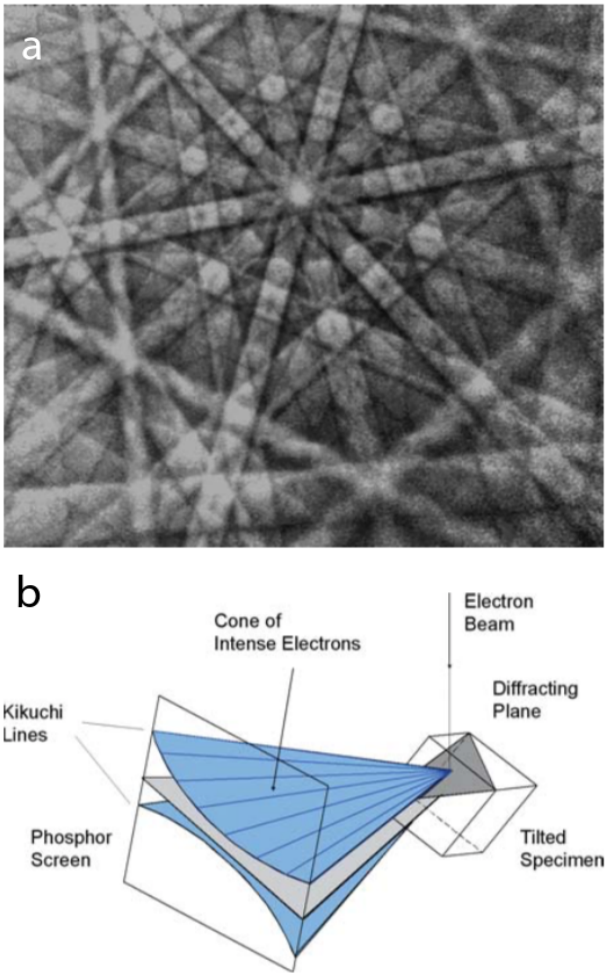

Figure 1.10.: Example Kikuchi pattern as seen by the EBSD detector (a), and schematic of the formation of Kikuchi-bands (b). From [29].

direction of $\mathbf{g}$ must be determined for multiple sets of diffracting lattice planes, i.e. for multiple bands in the pattern. If the unit vector normal to the detector plane is $\mathbf{n}$ and L is the detector-to-sample distance, then the pattern centre may be defined as the vector $\mathbf{x^0}$, where

$$\mathbf{x^0} = L\mathbf{n}. \tag{1.10}$$

Further, if both lines are clearly detected, the closest points to the pattern centre on each line, $\mathbf{x}^+$ and $\mathbf{x}^-$ (henceforth referred to collectively as $\mathbf{x}^\pm$), may be determined. $\mathbf{x}^\pm$ are points on the detector plane which's vectors equals the sum of $\mathbf{x^0}$ and the shortest vector in the detector plane from the pattern centre to the line. With $\mathbf{x}^\pm$, one may determine the wave vectors for each point through

$$\mathbf{k}^\pm = \frac{\mathbf{x}^\pm}{\lambda \|\mathbf{x}^\pm\|}, \tag{1.11}$$

and from this the lattice normal may be found by Equation (1.12) [31]:

$$\mathbf{g} = \mathbf{k}^+ - \mathbf{k}^-. \tag{1.12}$$

If the lines of the cones are diffuse on the detector such that their position is unclear, but the band spanned between them is visible, one can assume the midline of the band to correspond to the plane trace of the set of diffracting planes. Then, if $\mathbf{x}^\perp$ gives the position on the detector plane of the point on the midline closest to the pattern centre (analogous to $\mathbf{x}^\pm$), then the direction of $\mathbf{g}$ can be calculated through

$$\frac{\mathbf{g}}{\|\mathbf{g}\|} = \pm \mathbf{n}^\perp \times \mathbf{t}, \tag{1.13}$$

where $\mathbf{n}^\perp$ is the unit vector of $\mathbf{x}^\perp$ and $\mathbf{t}$ is the unit vector tangent to the midline of the band [31].

To automatically detect Kikuchi-bands in a pattern recorded by the detector, a Radon- or Hough-transform is employed [29]. These mathematical methods seek to describe the observable lines by the polar equation of a straight line, where the line is parametrised by the shortest distance from the origin to the line, r, and the angle between the x-axis and the normal from the line to the origin, ϕ:

$$r = x \cos\phi + y \sin\phi. \tag{1.14}$$

The positions of the detected lines on the detector can subsequently be compared with calculated positions for a given crystal phase and orientation based on a crystallographic database. This requires that $\mathbf{x^0} = L\mathbf{n}$ is carefully calibrated, as the position of $\mathbf{x^0}$ on the detector can serve as the origin and the detector-to-sample distance L is necessary to correctly determine $\mathbf{x}^\pm$ and $\mathbf{x}^\perp$ and thus $\mathbf{g}$.

Scanning across a sample area can be achieved in three different modes. In the beam scan mode, the sample is scanned similarly to the normal SEM: The beam is deliberately deflected

from position to position by the instrument optics to systematically raster the desired area. Because no mechanical movements are involved, beam scans are very fast. However, it is only possible to scan relatively small areas, and the travel of the beam across the stationary sample causes travel of the pattern centre on the detector, which makes so-called dynamic pattern centre calibration necessary [29]. In the second mode, the stage scan, the beam is kept centred while the stage is moving mechanically between the positions. This is typically much slower than a beam scan but has the advantage that much larger areas can be covered and that all geometrical factors remain constant [29]. Beam and stage scan can be combined into a third mode, the combo scan, where beam scans at multiple adjacent stage positions are stitched together. Combo scans allow the most time effective mapping of large areas but suffer otherwise from the same disadvantages as the beam scan.

1.5.4. Simple Linear Regression

A simple linear regression is a regression in which y is a linear function of the regression parameters (e.g. β_0, β_1) and with only a single explanatory variable x. Applying an ordinary least squares method to a regression model $Y = \beta_0 + \beta_1 x + \epsilon$, where ϵ is a stochastic variable simulating the error, we get the estimated regression line $\widehat{Y} = b_0 + b_1 x$, with the least squares method given by minimising the sum of square errors (SSE):

$$min\big(\sum_{i=1}^{n}(Y_i - \widehat{Y}_i)^2\big) = min(SSE) \tag{1.15}$$

The estimated regression parameters b_0, b_1 are then given by Equations (1.16) and (1.17) [32]:

$$b_1 = \frac{\sum_{i=1}^{n}(x_i - \bar{x})Y_i}{\sum_{i=1}^{n}(x_i - \bar{x})^2} \tag{1.16}$$

$$b_0 = \bar{Y} - b_1\bar{x}, \tag{1.17}$$

Barred symbols indicate the mean value. Under the assumption that ϵ is a gaussian distribution with $E(\epsilon) = 0$ and $Var(\epsilon) = \sigma^2$, the variance σ^2 is estimated by the mean squared error (MSE) s^2 [32]:

$$s^2 = SSE/(n-2) \tag{1.18}$$

1.5.5. Filtering of Orientation Data

1.5.5.1. Median Smoothing Filter

A median filter is an edge-preserving smoothing filter. The term median filter suitably describes the method, where, for each pixel in an image or map, all values in a window of neighbouring

pixels are sorted to find the median value which is subsequently returned as the new value of the candidate pixel.

Applying a median filter to an orientation map necessitates a clever way of determining the median in a set of orientations. A common procedure is to find the angular distance or disorientation of each orientation to all the others in a window of nearest neighbours, calculate the mean or cumulative of this value for each pixel in the window, and select the orientation of the pixel which holds the minimum mean/cumulative distance/disorientation to all others as the new orientation value for the candidate pixel [9, 33]. Following Hielscher et al. [9], this can be summarised mathematically as follows:

Let $N(\mathbf{x})$ be a window of positions in the neighbourhood of the candidate position $\mathbf{x}$, and $\delta(\boldsymbol{O}, \tilde{\boldsymbol{O}})$ be the disorientation angle between the orientations $\boldsymbol{O}$ and $\tilde{\boldsymbol{O}}$. The candidate is then given its new orientation $\tilde{\boldsymbol{O}}(\mathbf{x}')$ of $\mathbf{x}' \in N$ which holds the minimum mean disorientation angle to all other orientations $\tilde{\boldsymbol{O}}(\overline{\mathbf{x}})$ in N such that Equation (1.19) is satisfied when $\mathbf{x}''$ is any other position in $N(\mathbf{x})$.

$$\sum_{\overline{\mathbf{x}} \in N(\mathbf{x})} \delta(\tilde{\boldsymbol{O}}(\mathbf{x}'), \tilde{\boldsymbol{O}}(\overline{\mathbf{x}})) \leq \sum_{\overline{\mathbf{x}} \in N(\mathbf{x})} \delta(\tilde{\boldsymbol{O}}(\mathbf{x}''), \tilde{\boldsymbol{O}}(\overline{\mathbf{x}})) \tag{1.19}$$

1.5.5.2. Kuwahara Smoothing Filter

The Kuwahara filter is another edge-preserving smoothing filter. Like for the median filter, a window of nearest neighbours around the candidate is considered. However, in the Kuwahara filter, this window is divided into sections, typically quadrants. The mean and variance are calculated for each quadrant, and the candidate is given the mean value of the quadrant with the lowest variance [34, 35]. Because it bears no direct relevance to the work reported here, a discussion of approaches for finding the mean and variance of orientations is left out.

2. Methods

2.1. Sample Material

Prior to this work, bicrystals with the GBs desired for investigation were fabricated. The types of CSL boundaries fabricated are listed in Table 2.1.

Table 2.1.: The artificial grain boundaries that have been fabricated.

CSL type	Cut plane
Σ3	{1 1 1}
Σ3	{1 1 2}
Σ27	{1 1 5}
Σ27	{5 5 2}

The fabrication involved cutting an ingot of mono-Si into bricks along specific planes and rotating the bricks in such a way that they would create the desired boundary symmetry, as sketched in Figure 2.1. The re-assembled ingot was placed on an as-sawn Si plate, covered in Si granules, and then partly melted from the top and re-solidified, yielding an ingot with the artificial GBs. The ingot was subsequently cut along planes perpendicular to the grain boundaries, into slabs of approximately 1 mm to 2 mm thickness. Each slab would then be a vertical cross-section of the ingot, containing 1 to 3 GBs of interest. The cuts were not completely vertical, but approximately at an 8° angle, in order to obtain good reflection positions during in-situ diffraction experiments on some of the samples at the ESRF synchrotron. The work covered in this report is concerned with slabs that were not used for in-situ measurements.

2.2. Sample Preparation

2.2.1. Grinding, Polishing and Cutting

The sample specimens were mirror polished on one side by grinding with silicon carbide sandpaper, followed by polishing in a Struers AbraPol-20 semi-automatic machine down to 1 µm diamonds. Mirror polishing was done prior to µ-PCD and EBSD measurements.

Before EBSD investigations could take place, the slabs had to be cut to smaller dimensions. Some cuts were made by sawing (work not performed by the author), and some cuts were

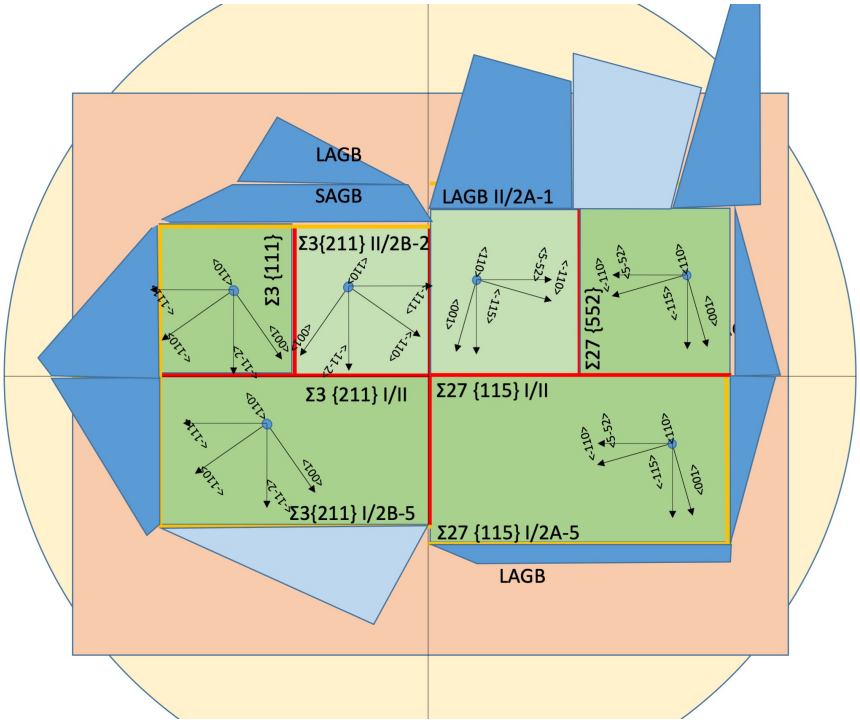

Figure 2.1.: Illustration of the arrangement of seeds to obtain the desired GBs. CSL GBs found in the samples analysed in this work are indicated by text next to the boundary. Coordinate axes denote the orientation of the bricks.

made by breaking the sample along crack initiations scribed by laser in a CL Advanced laser marking device from Stjernberg Automation and Rofin. The final size of the samples were 2 cm to 3 cm in width (across the GBs) and 8 cm to 9 cm in height (along the GBs).

2.2.2. Sopori Defect Etching

The samples were subjected to a defect-revealing Sopori etch in order to reveal dislocations and grain boundaries. The mirror-polished samples were RCA-cleaned and held in 5 % HF for 3 min prior to the Sopori etch. For the Sopori etch itself, samples were generally dipped for a duration of 25 s, except for the second etch of the $\Sigma27\{1\,1\,5\}$, when the purpose of the etching was to just slightly reveal the defects before EBSD measurements, in which the duration was 10 s. Etching procedures were not performed by the author.

In between the two etchings of the $\Sigma27\{1\,1\,5\}$, the sample was ground once and polished multiple times. The difference in thickness of the sample after the first etch and after the second etch was measured with a sliding gauge.

2.3. Microwave Photoconductive Decay

µ-PCD scans were performed in a Semilab WT-2000PVN device with a 904 nm wavelength laser. The excitation area is supposed to be 1 mm^2. An overview scan of each sample was made with a raster step size of 0.500 mm. Additionally, scans around each artificial grain boundary were made with 0.125 mm step size. The samples were mirror polished and without any surface passivation. As a result, recorded lifetime values do not give the true lifetimes. The offset may be especially large for the zones of higher lifetime in the grain bulk, which might have much larger lifetime values than the ones recorded.

2.4. Optical Examinations of Etch-Delineated Defects

The delineated defects of the Sopori etched samples were documented by means of optical methods. The slabs were scanned across their full size in an Epson Perfection V850 Pro image scanner with a resolution of 1200 pixels per inch. Additionally, each of the CSL boundaries was mapped by optical microscopy using a Leica MEF4M microscope with the ProgRes CapturePro v2.8.8 software. The maps cover the grain boundaries along their entire height and between 2 mm to 4 mm on either side. They were created by stitching micrographs taken at 2.5x objective lens magnification (the additional magnification of the camera lens is unknown). Stitching was done using the ImageJ software. The stitched maps offer a much higher level of detail compared to the scanned maps. The $\Sigma 27\{1\,1\,5\}$ boundary was mapped by both techniques twice, once after the first etch and once after the second etch.

2.5. Electron Backscatter Diffraction Acquisition

When referring to EBSD acquisitions, the following coordinate system of the specimen will be used: The rolling direction (RD) lies along the tilt axis of the stage when the specimen is mounted, this direction closely corresponds to the growth direction (height of the GB). The transverse direction (TD) is defined as perpendicular to the RD in the specimen surface plane. The normal direction (ND) is the direction normal to these two and thus also normal to the surface.

2.5.1. Combo Scans

Large scale orientation maps were recorded of 4 of the boundaries, one of each CSL and boundary plane type. The maps were made using the online indexing combo scan feature of the OIM Data Collection 7 software on a computer connected to a JEOL JSM-840A scanning electron microscope equipped with an EBSD detector from NORDIF, a TSL MSC-2200 unit and a Deben Sprite stage controller.

The large maps recorded were typically on the order of 10 mm width and 68 mm height along the GB, or similar. The height was limited by the stage movement range. Multiple combinations of step size and instrument magnification were tested, with step sizes ranging from 10 µm to 100 µm and magnifications of either 70x or 120x. The settings were chosen as a compromise between scan quality, resolution, scan duration and data size. Scans were done at 62.5° tilt to be safe against a collision of the samples with the detectors when scanning the rather large areas. The samples were polished prior to every scan to ensure a high surface quality without carbon depositions from previous scans reducing the quality of the Kikuchi patterns.

2.5.2. Stage Scans

To examine the evolution of the disorientation between the two grains of the bicrystal, a stage scan procedure was designed using the Custom Scan feature of the OIM Data Collection 7 software. Henceforth, the disorientation between the two grains will be referred to as the macroscopic disorientation of the sample. When referring to measurements, the RD axis will be referred to as the y-axis, and the TD axis as the x-axis of the sample. The Custom Scan feature enabled the possibility to program the step sizes for the x-axis and the y-axis individually, as well as the stage position and beam deflection. Each single measurement point had to be programmed in a .txt file fed to the OIM Data Collection 7 software.

To obtain good statistics, the procedure was designed to return an ample amount of data points $\{x_{ij}\}_{j=1}^{n}$ for each y_i. With a scan width of 20 mm and x-axis step size of 100 µm, 201 data points per line y_i were sampled, or approximately 100 data points per grain per line y_i. The y-axis step size was 500 µm along a height of 67 mm, with the height limited by the range of motion of the stage. The procedure was designed as a pure stage scan, with no beam deflection on any measurement point. To effectively write the necessary .txt files custom-designed for each scan, a Matlab script was written, which is listed in Appendix B.2.

Using the same equipment as in Section 2.5.1, two stage scans were done on the $\Sigma27\{1\,1\,5\}$. The samples were mirror polished and the scans were performed with the same equipment as in Section 2.5.1. The first scan covered the lower part of the sample, while the second scan covered the top part of the sample. Because the sample was approximately 9 cm tall and the scan range was almost 7 cm, the scan areas overlap significantly. The magnification was 70x and the tilt was 62.5°.

2.5.3. Beam Scans

To further investigate the subgrain formation from the $\Sigma27\{1\,1\,5\}$ grain boundary, beam scans with a higher resolution were recorded using a Zeiss Ultra 55 field emission SEM with an EBSD detector from NORDIF. The scans were programmed using either the NORDIF or the NORDIF3 software programs. For these measurements, the samples were mirror polished and then slightly

etched, to make it easier to navigate the sample and find the positions of interest. Instrument settings for these scans were 50x magnification, 5 µm step size, and the sample was tilted to 70°. Exposure and pattern resolution settings vary between different sessions.

2.5.4. Calibration

For the JEOL instrument, the accuracy of the orientation indexations was inspected by analysing the orientations in a scan of a float zone (FZ) specimen. This scan was made by another group member prior to this work. Comparing the known orientations of the FZ with the observed orientations, the offset could be determined. Following this, a similar scan and calibration procedure was made on the Zeiss Ultra 55 instrument.

In addition, the slack in the tilting mechanism of the JEOL was briefly tested using the same FZ specimen and the OIM Data Collection 7's feature for interactive indexing.

2.6. Analysis of Orientation Data

2.6.1. Analysis of Beam and Combo Scans

The data collected by EBSD has been examined using multiple methods. The combo scans have primarily been analysed through examination of inverse pole figure (IPF) maps and image quality (IQ) maps generated in TSL OIM Analysis 7, as well as by using the grain boundary detection in the same software. This data has been compared with lifetime and defect maps to select areas for in-depth investigations through higher resolution beam scans. In general, the IPF maps have been plotted along the ND direction, which was found to better display the interesting results than the TD and RD directions.

Analysis of data acquired from beam scans has also been handled in TSL OIM Analysis 7, as for combo scans. Two methods have been used to investigate disorientations across SAGBs. The Vector Profile Mode of the software has been used to probe if the disorientation of the SAGB remains constant or if it changes with the height, and to determine the value where of interest. The disorientations have been sampled by drawing profiles of 100 µm length vertically (which in these scans is roughly along the TD) across the SAGB for approximately every 100 µm to 200 µm of the SAGB, as illustrated in Figure 2.2. The disorientation for each profile has been estimated manually by considering the point-to-origin disorientation reported by the software. The second method is the TSL OIM Analysis 7 feature for detecting and plotting grain boundaries of various types in maps. This has been used to generate the grain boundary maps (white maps with colour-coded grain boundaries). The grain boundaries have been detected with the Brandon criterion as the tolerance angle limit, and the maps were smoothed with the built-in Kuwahara smoothing filter of TSL OIM Analysis 7 to reduce the tendency of noise obscuring the grain boundaries. Smoothing was done through 3 iterations with 10th order nearest neighbours.

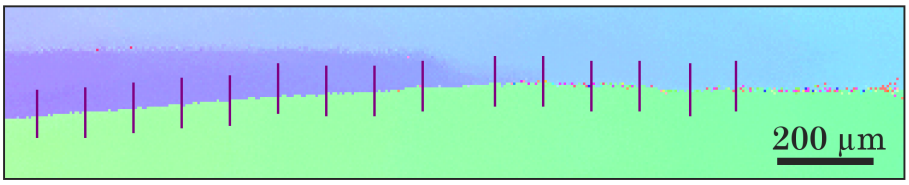

Figure 2.2.: An example IPF map with 100 µm vertical profiles at regularly spaced intervals along a grain boundary, showing how disorientation evolutions were sampled.

Certain subgrains observed in some beam scans have also been examined and compared by pole figure inspection. The pole figures were also generated in TSL OIM Analysis 7. Using the pole figures, the degrees of tilt around $\langle 1\,1\,0 \rangle$ between subgrains have been estimated. For this procedure, the scans were cropped to sections containing all subgrains of interest. These sections were then smoothed using the Kuwahara smoothing filter through 1 iteration with 5th order nearest neighbours. Subsequently, the $\{1\,1\,0\}$ pole figures for each section were generated. Because the subgrains had a common $\{1\,1\,0\}$ pole roughly on the RD axis (growth direction), the tilt around the $\langle 1\,1\,0 \rangle$ axis could be estimated by measuring the angular distance with which the other poles were displaced from each other. The angular distance between poles was extracted from the pole figure using the Misorientation tool of TSL OIM Analysis 7 (which, when used in pole figures, gives the angular distance between the two sample directions being probed).

2.6.2. Estimating the Noise and Systematic Deviations in Beam Scan Data

In order to estimate the questionable orientation gradients and noise level in the beam scans performed on the Zeiss Ultra microscope, 3 scans from 3 different sessions were chosen and disorientation profiles were sampled in the TSL OIM Analysis 7 software. 2 horizontal and 3 vertical profiles were sampled on each of the 2 crystals in each scan, as can be seen in Figure 2.3. Each profile was scrutinised to discard profiles which exhibited non-linear trends in the point-to-origin disorientation, e.g. due to a SAGB, such that only profiles with no visible indications of real orientation shifts in the sample crystal remained for further analysis. See Figure 2.4 for an example of an accepted (a) and a discarded (b) profile.

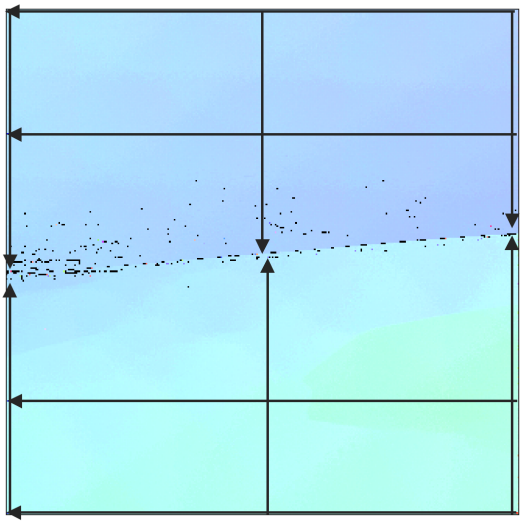

Figure 2.3.: An example IPF map showing how the profiles used for noise and gradient estimations were sampled (along the arrows).

The qualified profiles were then fitted to a

linear profile by simple linear regression analysis with the regression model $Y = \beta_0 + \beta_1 x + \epsilon$, as described in Section 1.5.4, with the assumption of a gaussian distribution of the error. Figure 2.4 (a) shows an example fit. I.e. Y represents a shift in orientation and x represents a position along the profile. Each sampled profile was fitted to this model using the least-squares method implemented in Matlab and the probability maximisation estimators b_1 and s^2 were extracted from each profile.

Following this, the mean of the b_1 values from the horizontal profiles was used to estimate the horizontal gradient in the scans and the mean of the b_1 values from vertical profiles was used to estimate the vertical gradient. The mean of the s^2 values from all profiles was used to estimate the level of the measurement noise. A similar procedure was done on the scan of the monocrystalline FZ specimen for comparison. In this case, 3 horizontal and 3 vertical profiles were taken. The code used is available in Appendix B.3.

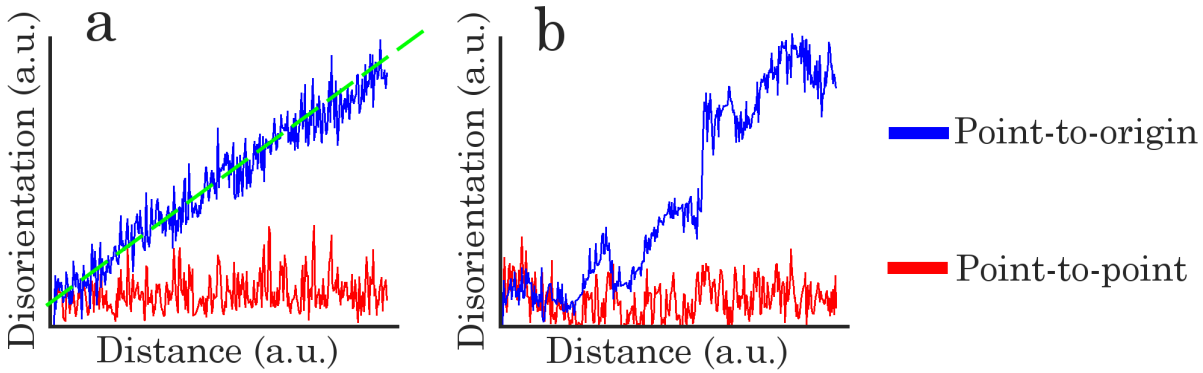

Figure 2.4.: Example profiles sampled for noise and gradient estimations. An accepted profile with a trendline in green (a), and a discarded profile (b). The origin is the first data point sampled for that profile.

2.6.3. Macroscopic Disorientations

To as precisely as possible determine the evolution of the macroscopic disorientation from the data acquired by stage scan, a set of algorithms were written and implemented in Matlab. The data was first treated by a confidence index (CI) discriminating filter, selecting all data points below a CI threshold value and rewriting as not-a-number (NaN) values which would be ignored in the later functions. Each line y_i was then smoothed with an edge-preserving median filter for orientations to remove noise. The filter implemented is similar to the median filter for orientations presented in Section 1.5.5.1. In this work, a one-dimensional window is used as opposed to the more typical two-dimensional window, because all lines $\{y_i\}_{i=1}^{m}$ are isolated from each other.

After smoothing, each line was analysed by an algorithm that detects significant peaks in

the point-to-point disorientation and determines the positions of the grain boundaries from this. To make sure that impulsive noise would not cause detection of false GBs, a control mechanism henceforth referred to as the nearest neighbour control was implemented. The nearest neighbour control compares the orientations of the 2 nearest neighbours on each side of a detected peak. The disorientations are calculated for all 4 pairwise combinations across the peak. Only if all the combinations exceed the aforementioned threshold value, the detected peak is accepted as the position of a grain boundary. An additional mechanism that would ignore boundaries to very small grains (less than 3 data points) was also implemented.

Finally, the 2 largest detected grains in each line y_i, i.e. the main grains of the bicrystal, were examined for their median orientations and these median orientations were used to find the macroscopic disorientation for this y_i. The procedure is summarised in pseudocode in Listing 2.1 and the full code can be found in Appendix B.1. A discussion of the parameters used is found in Section 4.2.2.

Throughout the algorithms, disorientations were calculated using the following process. The rotation matrix $\boldsymbol{G}$ of each orientation was calculated from the recorded Bunge convention Euler angles according to Equations (2.1) and (2.2) [36]. This was done prior to all data treatment.

$$\boldsymbol{G} = \begin{pmatrix} g_{11} & g_{12} & g_{13} \\ g_{21} & g_{22} & g_{23} \\ g_{31} & g_{32} & g_{33} \end{pmatrix} \tag{2.1}$$

$$\begin{aligned} g_{11} &= \cos\phi_1 \cos\phi_2 - \sin\phi_1 \sin\phi_2 \cos\Phi \\ g_{12} &= \sin\phi_1 \cos\phi_2 + \cos\phi_1 \sin\phi_2 \cos\Phi \\ g_{13} &= \sin\phi_2 \sin\Phi \\ g_{21} &= -\cos\phi_1 \sin\phi_2 - \sin\phi_1 \cos\phi_2 \cos\Phi \\ g_{22} &= -\sin\phi_1 \sin\phi_2 + \cos\phi_1 \cos\phi_2 \cos\Phi \\ g_{23} &= \cos\phi_2 \sin\Phi \\ g_{31} &= \sin\phi_1 \sin\Phi \\ g_{32} &= -\cos\phi_1 \sin\Phi \\ g_{33} &= \cos\Phi. \end{aligned} \tag{2.2}$$

ϕ_1, ϕ_2 and Φ are the three Bunge convention Euler angles. All misorientation rotation matrices $\boldsymbol{M_{12}}$ between two orientation measurements 1 and 2 were then calculated by cycling through all $k = 1, \ldots, 24^2$ variations of

$$\boldsymbol{M_{12,k}} = \boldsymbol{T_1^{-1} G_1^{-1} T_2 G_2}, \tag{2.3}$$

with the matrices $\boldsymbol{T}$ being the symmetry operators giving the 24 crystallographically equivalent solutions, matrices for which were taken from [36]. The misorientation was then extracted from

each of the misorientation rotation matrices through

$$\theta_k = \arccos \frac{m_{11,k} + m_{22,k} + m_{33,k} - 1}{2}, \tag{2.4}$$

where $m_{11,k}$, $m_{22,k}$ and $m_{33,k}$ are the diagonal coefficients of $\boldsymbol{M_{12}}$ [36]. Finally, the disorientation δ was found by taking the minimum of all $\{\theta_k\}$.

Listing 2.1: Pseudocode summary of the macroscopic disorientation analysis procedure.

```
(ci filter)
for all data points
    if confidence index =< 0.2
        make NaN

segment data set into sets of monotonous y values (i=1 to m)

(median filter)
for each y_i
    for each x_ij (each candidate)
        make a window from j-5 to j+5

        find disorientations between all data points in the window

        calculate the cumulative disorientation for each data point


        find the smallest cumulative disorientation
            define the orientation of this data point as the median
               orientation of the window

        set candidate orientation equal to median orientation

(grain detection)
for each y_i
    calculate point-to-point (j-1,j) disorientations (ppdo)
    calculate point-to-origin (1,j) disorientations (podo) (the
       disorientation between data point j and the first data point
       in the y-segment)
```

```
(nearest neighbour control)
find peaks in ppdo > 0.025 radians threshold value
    calculate disorientation of (j-2,j+1)
    calculate disorientation of (j-2,j+2)
    calculate disorientation of (j-1,j+1)
    calculate disorientation of (j-1,j+2)
    if all 4 combinations  > threshold value
        accept as a grain boundary
    if not
        ignore grain boundary

(control size of grain)
if a detected grain extends < 3 pixels
    remove grain boundary (ignore grain)

(finding the 2 main crystals)
if grain > 50 pixels
    find median orientation for this grain

find disorientation between the 2 main crystals
    return this value
```

3. Results

3.1. Delineated Defects and Lifetime Maps

3.1.1. Σ27{115}

Although data has been acquired for all four types of grain boundaries listed in Table 2.1, this report will mostly be concerned with work done on the Σ27{1 1 5} type boundary, for which more in-depth work has been performed than for the others. This boundary type was chosen as the main focus because it was desirable to compare the results presented in the following with results from other parts of the INSIDES project at the moment in time where the work underlying this thesis was performed.

Two Σ27{1 1 5} boundaries were created, as can be seen in Figure 2.1, where both boundaries are indicated. For the remainder of this work, emphasis will be on the boundary named *Σ27*{1 1 5} *I/II* in this figure.

The image scan photograph after the first defect etch, which serves as a defect density map with arbitrary units, and the lifetime map of the Σ27{1 1 5} are displayed in Figure 3.1. Defects can be seen as darker features in the photograph, most of which are dislocations, especially in the darkest areas. Right above the seed, the GB is almost free from surrounding dislocations. A few millimetres higher, a dislocation array spreads from the boundary. Higher, more arrays arise, and the density and horizontal extent of the arrays increase until a height around 40 mm above the bottom of the seed, from which the density and the extent remain almost constant.

A clear correlation between the prevalence of defects and the measured lifetime is seen in the upper half of the maps. The lifetime map exhibits a heavily degraded zone along the GB which extends horizontally approximately to the same extent as the defected areas in the defect map. In the lower half, the general presence of a severely degraded red zone obscures the possible degradation effects of the GB and the surrounding dislocations. However, a faint improvement in lifetime around the GB can be observed. The seeds are clearly visible as areas with an enhanced lifetime at the bottom.

Figure 3.2 shows stitched micrographs of the lower part of the grain boundary where the dislocation arrays start forming. The micrographs are taken after the second etch. At 12 mm the first array blooms. It starts by sending out dislocations at angles up to 45° to the boundary, before turning very dense, especially leftwards of the boundary. From this point upwards, a

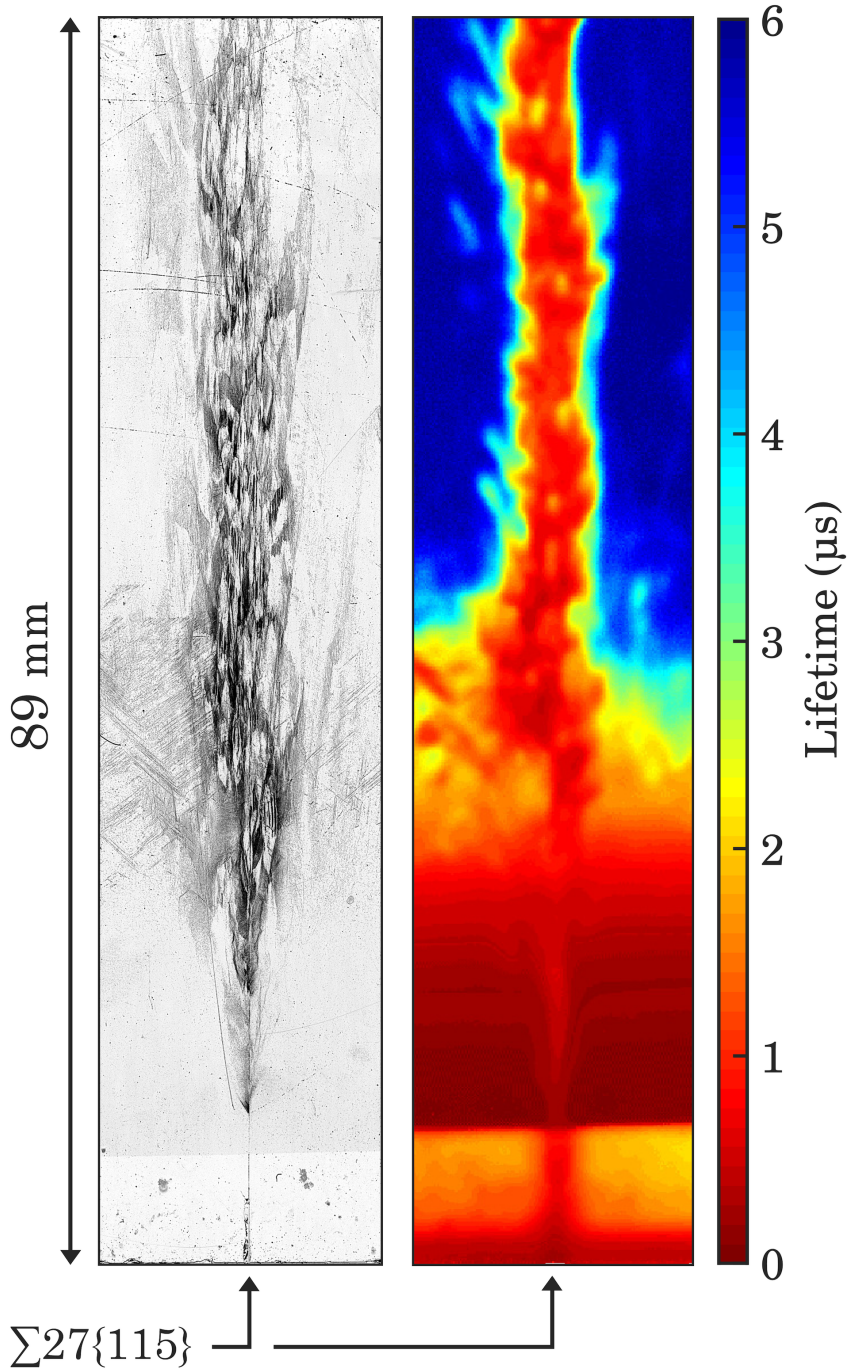

Figure 3.1.: Defect map (left) and lifetime map (right) of the Σ27{1 1 5} boundary. The sample was not passivated for the lifetime map.

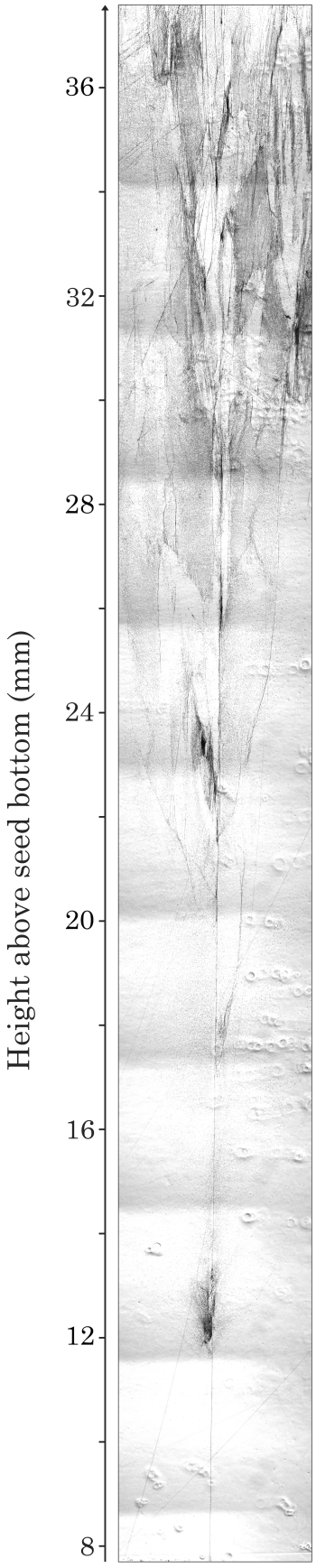

Figure 3.2.: Stitched, optical microscopy defect map of the first 30 mm above the seed in the $\Sigma 27\{1\,1\,5\}$ boundary sample.

cloud of sparsely distributed dislocations surrounds the boundary, with occasional, thin arrays meandering from the boundary. For example, at approximately 18 mm and 20 mm.

At just below 22 mm, two new, pronounced arrays begin. Although rising from the same point, the array on the left and the right side of the boundary is distinctively different. On the left, the array shifts between very densely dislocated and very scarcely dislocated areas. On the inside of this array, towards the boundary, there are relatively few dislocations. On the right, a line of closely spaced dislocations meanders out from the boundary, on the inside of which the density of dislocations is markedly higher than on the outside.

From approximately 26 mm, an almost 4 mm tall region begins which remains relatively dislocation free 150 µm into the crystal on each side. The material outside this region is fairly homogeneously covered in dislocations. However, very close to the boundary within the region are two smaller regions of very high dislocation density.

The tall region is followed by an increasingly chaotic ensemble of areas of various dislocation densities. Special attention is made to the point just below 30 mm where a faint area of intermediate dislocation density is observed as if growing leftwards out from the aforementioned tall region. Observations from this region and below will be subject to the later discussion.

3.1.2. Other Grain Boundaries

Image scan photographs and lifetime maps of one out of each of the three other types of CSL boundaries are displayed in Figures 3.3 to 3.5. Each boundary displays different characteristics, as well as common features. Whereas the $\Sigma3\{1\,1\,1\}$ boundary exhibits dislocation formation already from the top of the seed, Figure 3.3, the $\Sigma3\{1\,1\,2\}$ and $\Sigma27\{5\,5\,2\}$ boundaries, Figure 3.4 and Figure 3.5, respectively, do not produce significant amounts of dislocations before at several centimeters height.

Additionally, comparing the $\Sigma3\{1\,1\,2\}$ and $\Sigma27\{5\,5\,2\}$ boundaries, the dislocation arrays around the $\Sigma3\{1\,1\,2\}$ are wider and less dense than those of the $\Sigma27\{5\,5\,2\}$, which are confined much closer to the boundary. This is also reflected in the lifetime maps. In all cases, an improvement of the lifetime can be seen in the red zone along the boundary.

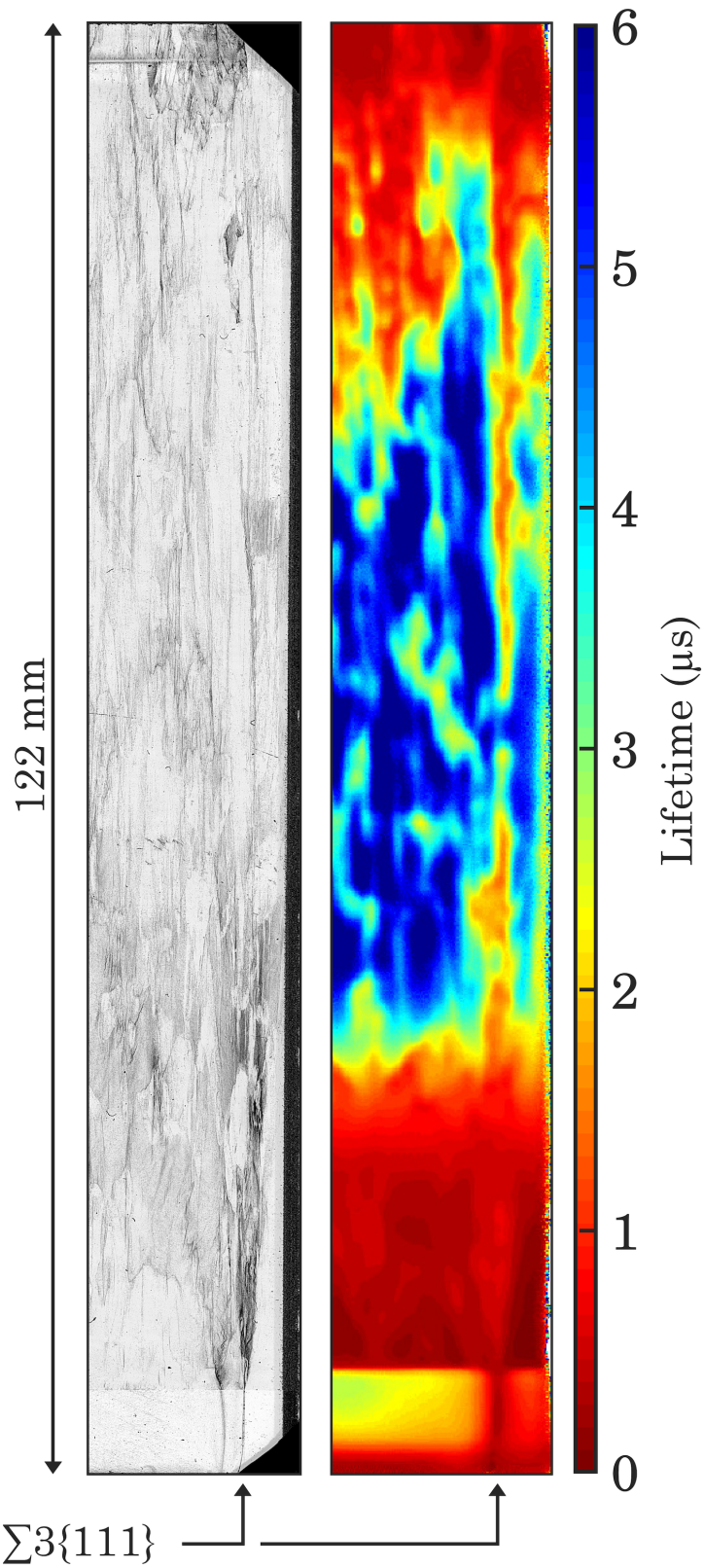

Figure 3.3.: Defect map (left) and lifetime map (right) of the Σ3{1 1 1} boundary. The sample was not passivated for the lifetime map.

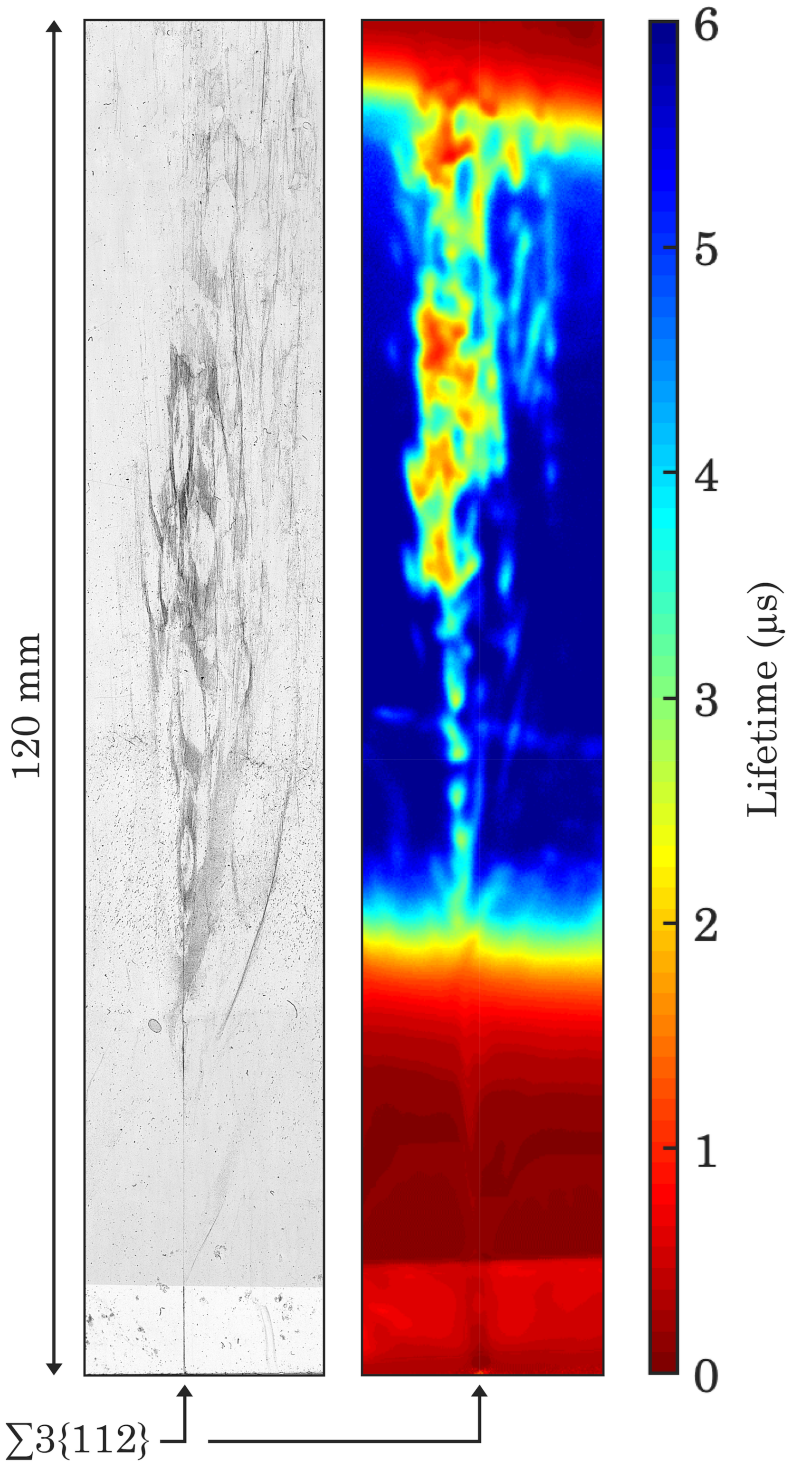

Figure 3.4.: Defect map (left) and lifetime map (right) of the Σ3{1 1 2} boundary. The sample was not passivated for the lifetime map.

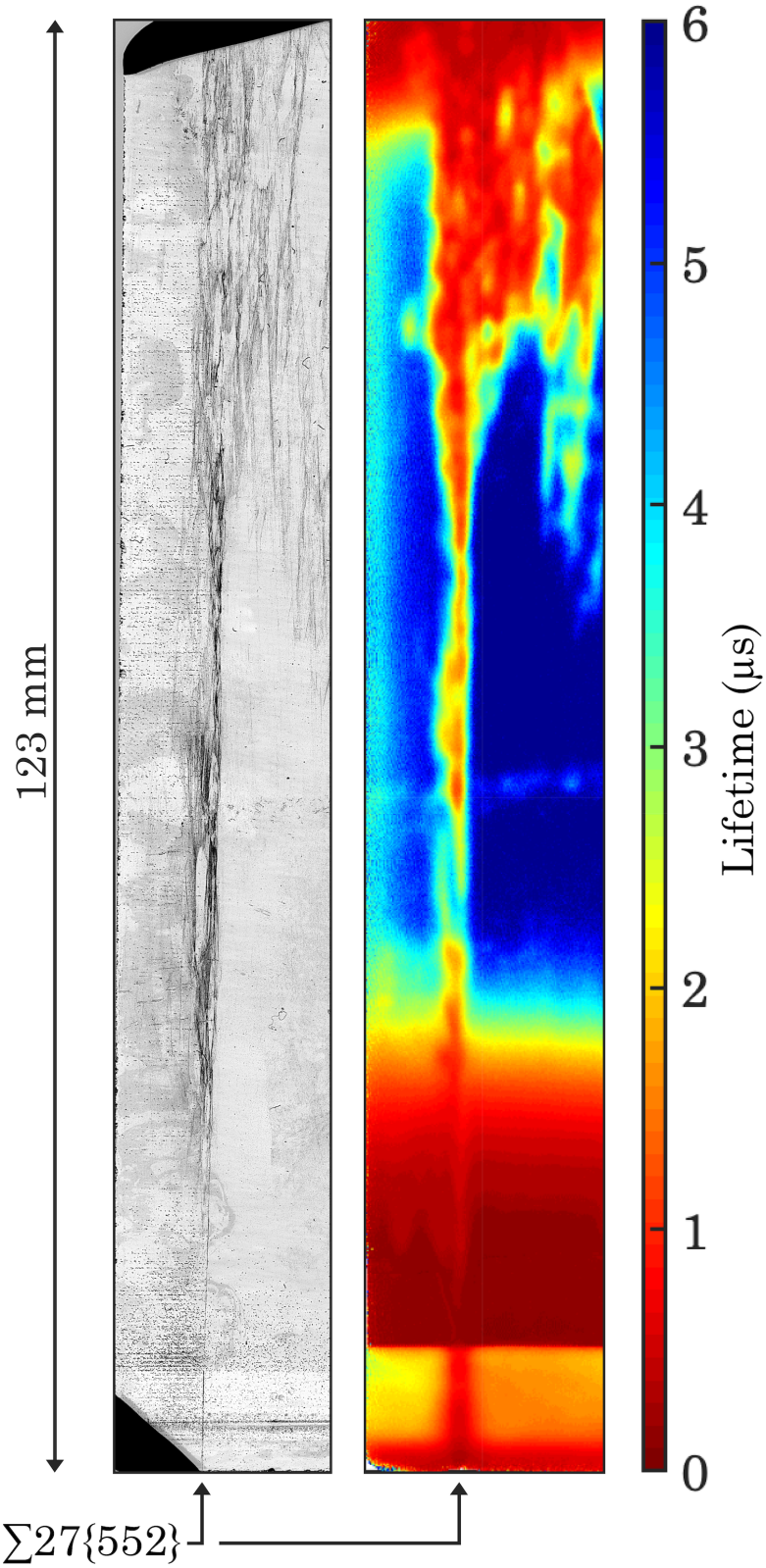

Figure 3.5.: Defect map (left) and lifetime map (right) of the Σ27{5 5 2} boundary. The sample was not passivated for the lifetime map.

3.2. Orientation Maps

3.2.1. Combo Scans

3.2.1.1. Σ27{115}

Figure 3.6 shows the result of two combo scans of the Σ27{1 1 5} GB. The main scan is an overview scan showing major parts of the sample, while the inset is a scan with higher resolution showing an area of high interest. The maps are IPF maps, where the orientation colour of each pixel represents the crystal orientation normal to the surface at this position.

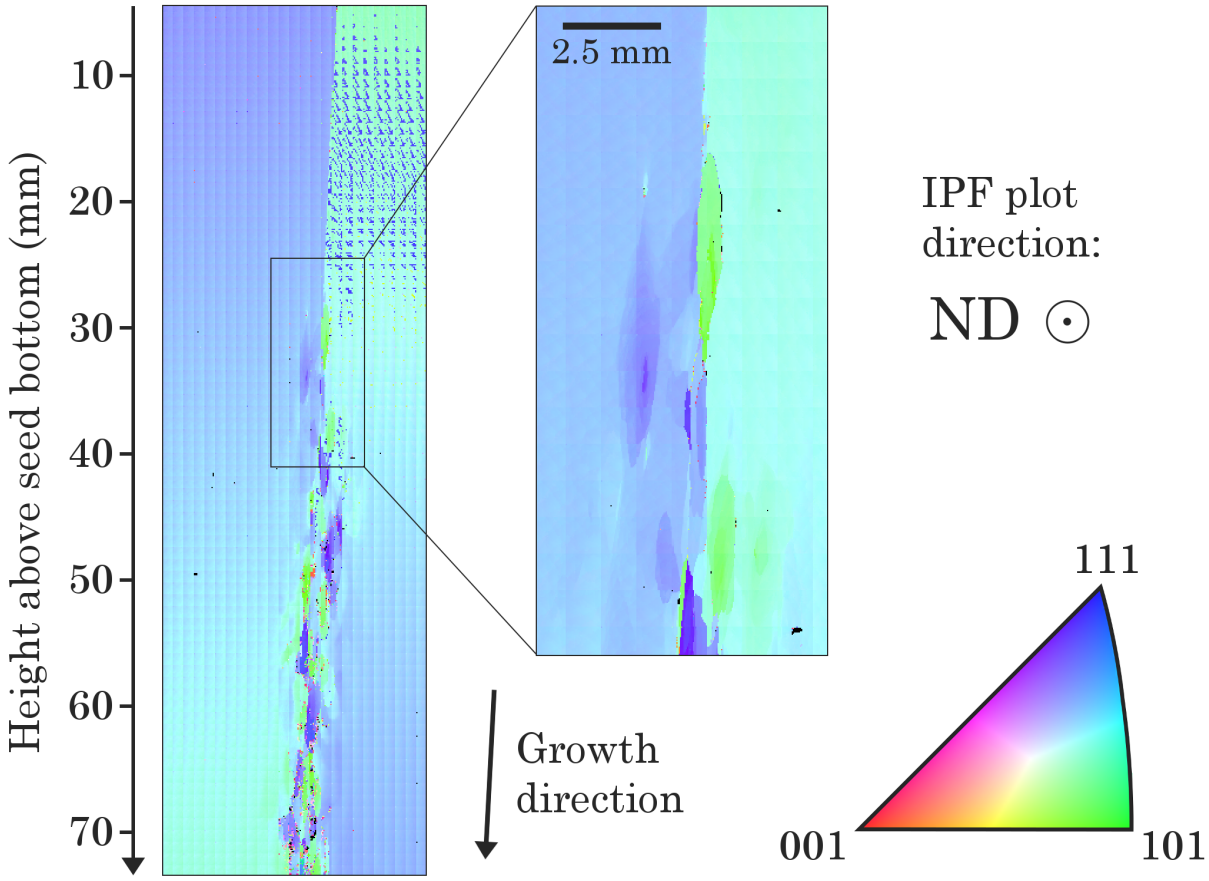

Figure 3.6.: Overview combo scan IPF map of the Σ27{1 1 5} boundary with 100 µm step size (left) and a 30 µm step size combo scan (inset) of an area of interest. The legend colours give the orientation parallel to the surface normal at every pixel.

In the top of the map, the GB can be seen from the abrupt change in colour from a blue to a turquoise shade. Moving higher in the growth direction (lower in the map), multiple subgrains can be seen growing out from the centre GB. Both crystals display a strong gradient but share an average colour somewhere in the light blue-turquoise region which corresponds well with the expected ⟨5 5 2⟩ direction. As is visible from both the main map and the inset, the subgrains tend to orientations that are either more towards the ⟨1 1 1⟩ direction or the ⟨1 0 1⟩

direction, compared to the parent crystals.

Several artefacts are present in the maps. These include the triangular misindexations in the top right corner of the main scan, the orientation misfits of the individual beam scans that have been stitched together giving the impression of a tiling, noisy misindexed pixels in the areas of high subgrain activity, and the strong orientation gradient across each of the crystals.

3.2.1.2. Other Boundaries

The combo scans of the 3 other boundaries are depicted in Figure 3.7. Again, the ND direction is plotted. The tints of all grains correspond well with the expected axes as described in Figure 2.1. Whereas the $\Sigma3\{1\,1\,2\}$ map is of relatively high quality, the maps of both $\Sigma3\{1\,1\,1\}$ and $\Sigma27\{5\,5\,2\}$ display a lot of non-indexed points. An orientation gradient can be seen in both crystals in all three maps, although not as evident in the $\Sigma3\{1\,1\,1\}$ and $\Sigma27\{5\,5\,2\}$.

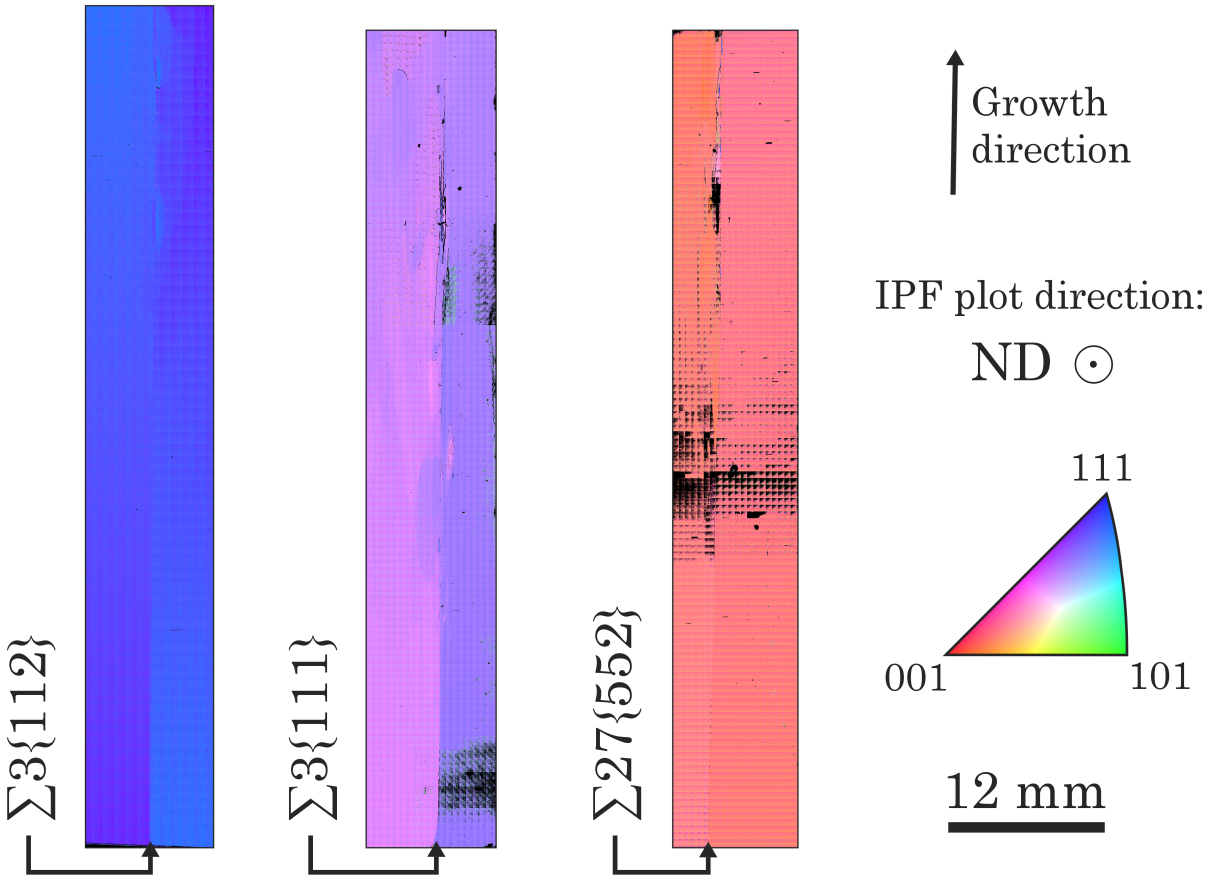

Figure 3.7.: Overview combo scan IPF maps of the $\Sigma3\{1\,1\,2\}$ (left), $\Sigma3\{1\,1\,1\}$ (center) and $\Sigma27\{5\,5\,2\}$ (right) boundaries. The legend colours give the orientation parallel to the surface normal at every pixel.

Subgrains are more difficult to discern in all of these maps, compared to the map of the $\Sigma27\{1\,1\,5\}$ in Figure 3.6. However, subgrains are faintly discernible in the top half around

the $\Sigma3\{1\,1\,2\}$ GB, the top two thirds around the $\Sigma3\{1\,1\,1\}$ GB, and the top half around the $\Sigma27\{5\,5\,2\}$.

3.2.2. Macroscopic Disorientation

The result of the macroscopic disorientation analysis performed on the $\Sigma27\{1\,1\,5\}$ sample using the custom scan feature and aforementioned data treatment (Section 2.6.3) is presented in Figure 3.8.

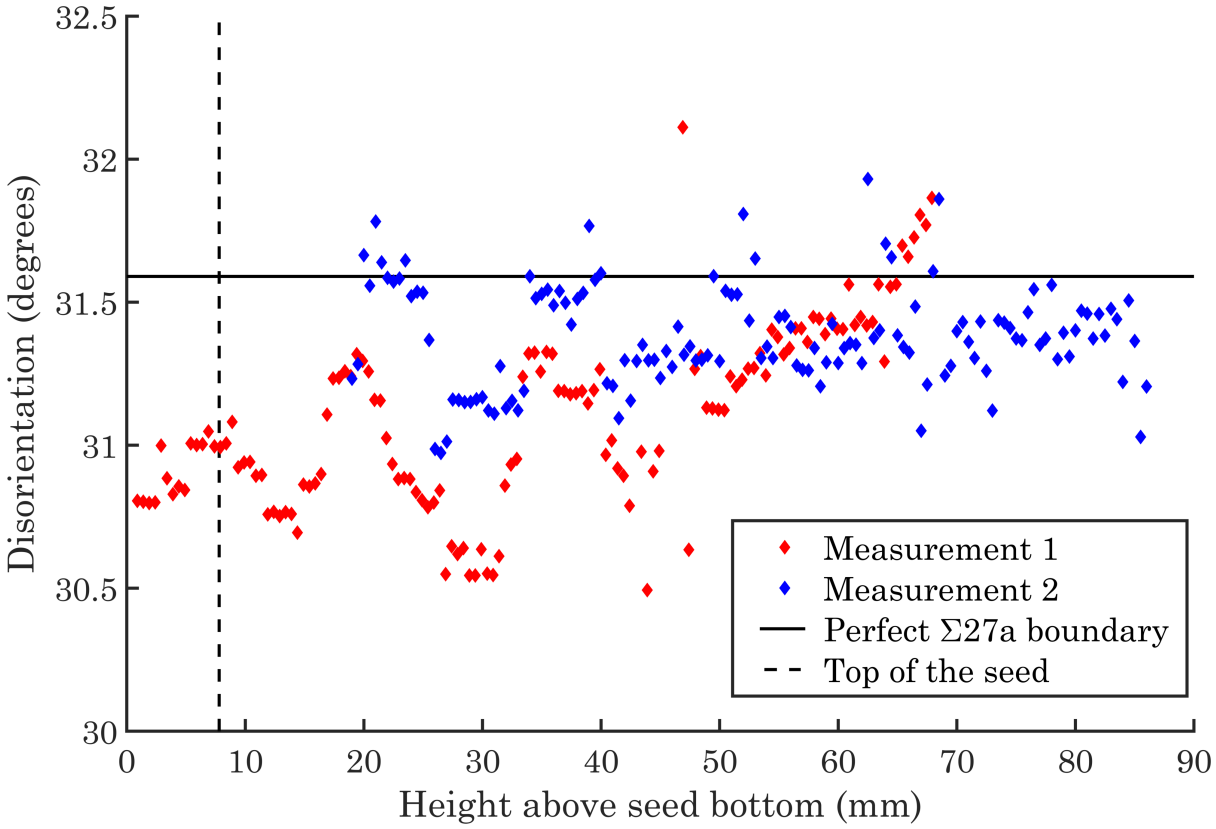

Figure 3.8.: A plot of the (macroscopic) disorientations of the $\Sigma27\{1\,1\,5\}$ as a function of height in the sample.

Immediately visible is that the two measurements do not perfectly overlap. Rather, they are displaced for as much as, perhaps, 0.3°. This is easiest to recognise between 20 mm to 40 mm. Also, whereas Measurement 1 seems to trend positively, the trend of Measurement 2 is more or less horizontal, or even sloping slightly negatively. However, it is apparent that the two measurements share some tendencies. The disorientation seems to jump between different plateaus, and these jumps occur at roughly the same x-axis position for both measurements. This is especially discernible for the jumps at approximately 26 mm, 33 mm and 41 mm height.

3.2.3. Beam Scans

A multitude of beam scans was performed on the $\Sigma 27\{1\,1\,5\}$ boundary to get a deeper insight into the formation of subgrains from the GB. Figure 3.9 gives an overview of the performed scans and how they relate to the defects observed in Figure 3.2. Once again, the IPF map is plotted for directions along the surface normal. Subgrains are clearly visible in many of the maps, most notably in insets (i-l), but also in insets (a-c) and (f-h). The insets (i-l) show the same (green) subgrain features as seen at approximately 29 mm to 34 mm in Figure 3.6 and in the inset of the same figure. With reference to Figure 3.2, the insets (a-c) correspond roughly to 21 mm to 26 mm, inset (d) to 18 mm, inset (e) to 12 mm, and the insets (f-h) to 26 mm to 30 mm. Although many features that are seen in the insets of Figure 3.9 display a rather strong colour contrast, all of the features are subgrains of either of the two main crystals.

3.2.3.1. Estimations of Noise and Systematic Deviations in Beam Scan Data

The mean of the extracted b_1 values for the horizontal profiles is $1.1754\,^\circ\,\mathrm{mm}^{-1}$, while the mean for the vertical profiles is $1.7024\,^\circ\,\mathrm{mm}^{-1}$. The individual b_1 values remain fairly consistent within profiles from the same scan, but large differences are seen from scan to scan. For the FZ specimen, the horizontal profiles have a mean of $0.1497\,^\circ\,\mathrm{mm}^{-1}$ and the vertical profiles have a mean of $1.9557\,^\circ\,\mathrm{mm}^{-1}$. The usefulness of these values is discussed in Section 4.3.

The values for s^2 remain relatively consistent across all scans, and the mean is calculated to be $0.0299\,\mathrm{deg}^2$. Taking this value as the variance of any given measurement point, the standard deviation is 0.1729°. 3 standard deviations amount to 0.5187°, such that 99.6 % of orientation measurements are correct within bounds of ± 0.5187° if the underlying assumptions are correct and no systematic errors are present. The variance found for the monocrystalline specimen was $0.0317\,\mathrm{deg}^2$.

If, for misorientation analyses, a pseudo-variance is calculated by taking the variance of each data point, s^2, and combining with an extra variance due to the gradient, $Var(gradient) = b_1^2$, using the well-known $Var\big(\sum_i^N a_i X_i\big) = \sum_i^N Var(X_i) + \sum_{i\neq j} Cov(X_i, X_j)$ for stochastic variables $\{X_i\}$ with coefficients $\{a_i\}$ and assuming all covariances are zero, we get:

$$\begin{aligned} Var(horizontal) &= 2 \times 0.0299\,\mathrm{deg}^2 + 1.1754^2\ \mathrm{deg}^2\,\mathrm{mm}^{-2} \times dx^2\ \mathrm{mm}^2, \\ StdDev(horizontal) &= \sqrt{0.0598 + 1.3816 \times dx^2}\ \mathrm{deg} \end{aligned} \tag{3.1}$$

and

$$\begin{aligned} Var(vertical) &= 2 \times 0.0299\,\mathrm{deg}^2 + 1.7024^2\ \mathrm{deg}^2\,\mathrm{mm}^{-2} \times dy^2\ \mathrm{mm}^2, \\ StdDev(horizontal) &= \sqrt{0.0598 + 2.8982 \times dy^2}\ \mathrm{deg}, \end{aligned} \tag{3.2}$$

with dx and dy being the horizontal and vertical distances, respectively, between the two probed points. Extracted values for b_1 and s^2 for each profile are given in Table 3.1.

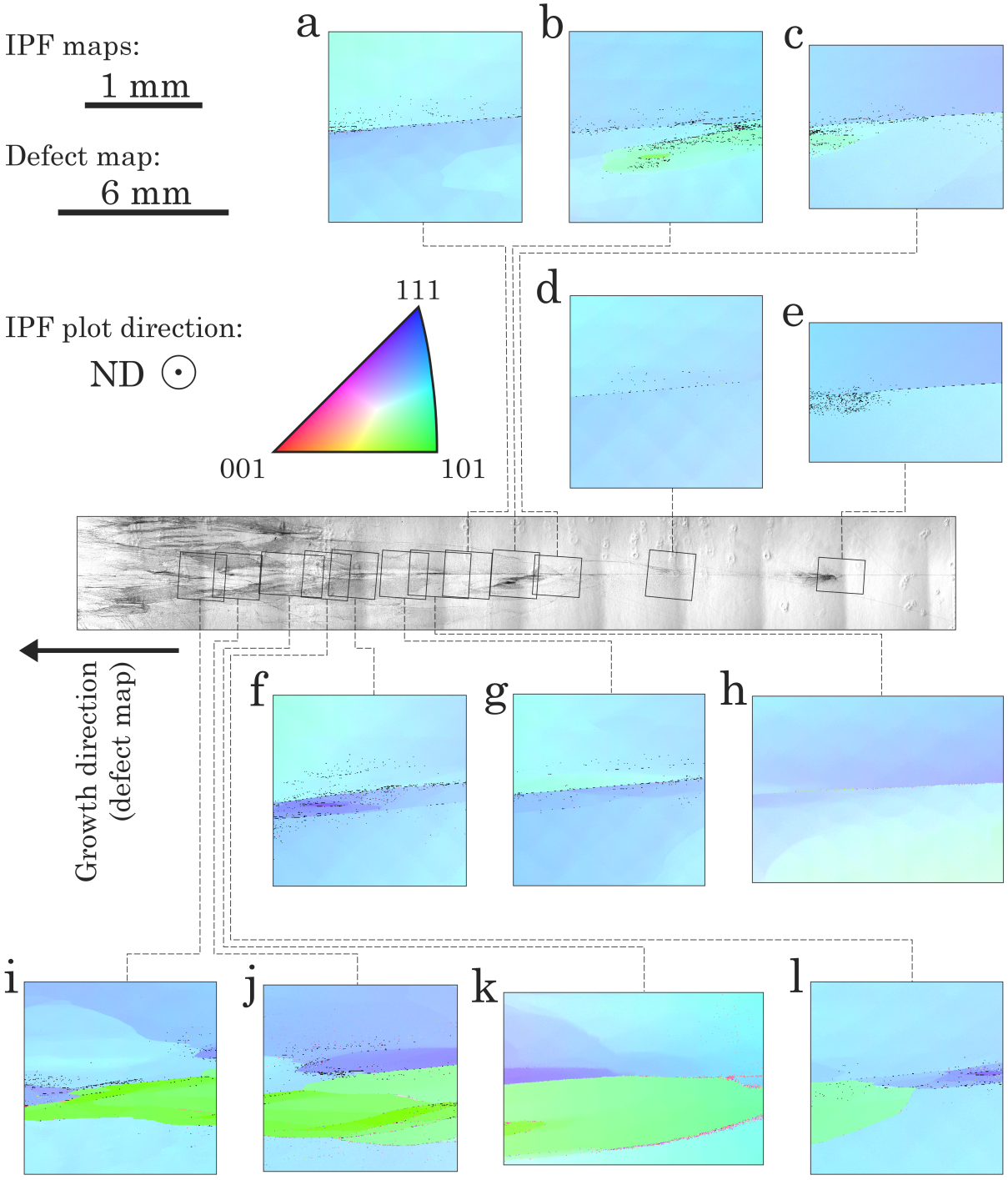

Figure 3.9.: An overview figure of the EBSD beam scans performed on the $\Sigma 27\{1\,1\,5\}$. The defect map shows the positions of the beam scans (insets) as they relate to Figure 3.2. The beam scans are plotted as IPF maps parallel to the surface normal.

Table 3.1.: Values found for the regression parameter b_1 and the estimated noise s^2.

Scan no.	Position	b_1 (deg/mm)	s^2 (deg^2)
Horizontal profiles			
#1	center of top grain	0.7094	0.0279
	top of top grain	0.6952	0.0305
#2	bottom of bottom grain	1.3763	0.0292
	center of bottom grain	1.3306	0.0253
	center of top grain	1.5626	0.0368
	top of top grain	1.5721	0.0349
#3	top of top grain	0.9816	0.0197
Mean (samples #1-3)		**1.1754**	
Mean (FZ specimen)		0.1497	
Vertical profiles			
#1	center of top grain	3.3998	0.0292
	rightmost in top grain	3.6950	0.0393
#2	center of bottom grain	1.1364	0.0150
	center of top grain	1.5411	0.0462
	leftmost in top grain	0.9957	0.0443
	rightmost in bottom grain	1.2382	0.0164
	rightmost in top grain	0.9123	0.0432
#3	leftmost in top grain	1.0428	0.0213
	rightmost in top grain	1.3602	0.0185
Mean (samples #1-3)		**1.7024**	
Mean (FZ specimen)		1.9557	
All profiles			
Mean (samples #1-3)			**0.0299**
Mean (FZ specimen)			0.0317

4. Discussion

4.1. Inadequacies in the EBSD Data Acquisitions

A lot of the data acquired by EBSD using the JEOL JSM-840A (combo scans and custom scans) suffer from one or more aspects of poor quality, in parts of the scan or in full. Several examples of such related artefacts have been pointed out in the previous section. Because of the implications this subpar data quality has on the interpretation of the results and the discussion that will follow, the inadequacies will be discussed prior to the general discussion of the results.

4.1.1. Miscellaneous Artefacts

The most obvious of the artefacts are the large regions of non-indexed (black) data points. A particularly good example is the IPF map of the $\Sigma 27\{5\,5\,2\}$ boundary shown in Figure 3.7. Some samples were more prone to this than others, the hypothesis for this being that the orientation of one or both of the two main crystals in each sample would give Kikuchi patterns where the zone axes were in positions making them more prone to be undetectable for the software whenever the quality of the pattern would be low. Thus resulting in regions with high amounts of wrongly indexed or non-indexed data points. For the same reason, it was in many cases difficult to obtain good indexing on both grains simultaneously. A potential workaround of this could be to have the sample turned 90° around the ND, however, this would lead to space issues because of the large sizes of the specimens in one of the dimensions.

It was observed that areas of non-indexation would often be at arbitrary positions on the sample, leading to the hypothesis that the source could be a fluctuation in the instrument parameters that would degrade the pattern quality at arbitrary times during the scan. This hypothesis was strengthened when it was later discovered that the filament voltage setting of the electron gun was set such that the instrument would run at the unstable false peak of the emission curve, rather than the much more stable saturation point. As the large scans required scan durations of 24 h to 72 h, typically around 48 h, the demands on current stability were higher than what could be achieved on this setting.

The orientation maps from combo scans suffer from visible tiling from the stitching of the individual beam scans recorded in the combo scan. This, among other things, severely disturbs any grain boundary maps generated from this data. The tiling can be attributed to an insufficient calibration of the dynamic pattern centre calibration, such that each tile (beam scan)

possesses both a horizontal and a vertical orientation gradient. Increasing the magnification reduces the demands on the quality of the dynamic pattern centre calibration on the expense of longer measurement durations (more stage movement steps), however, not sufficiently much to eliminate the tiling.

4.1.2. Sample Unlevel with Stage

Another observation was that the sample would not stay at the same working distance when moving the stage away from the centre position. This was found to be caused by the system of sample and sample holder not being level with the stage. The sample holder that was used, consisted of 3 pieces which were assembled with set screws. This assembly would not stack evenly, resulting in a slight tilt. Also, because the surface on which to mount the sample to the holder was rather small, the taping of the sample to the holder using carbon tape would also be prone to unevenness. In combination with the rather large scan area, this angular deviation would yield differences in the WD of as much as 2 mm to 3 mm between the ends of the scan area (typically 66 mm distance). This corresponds to angular deviations of up to 2° to 3° around the TD axis. A tilt around the RD would also be present, but this would have a less severe effect on the WD because of the shorter scan range in this dimension.

The absence of a levelness between the sample and the stage has a few consequences. Firstly, the preferred arrangement is to have the sample mounted such that the tilt axis of the stage is around the RD axis (recall that this is roughly along the GB, the long dimension of the sample), such that when tilted, both the upper and lower long edges lie horizontally in the instrument chamber. If this is the case and the sample is not level with the stage because of an unwanted tilt around TD, then, when moving the stage a step Δy_{stage}, the intersection between the incident electron beam and the specimen surface will move both a step Δy_{beam} and a step Δx_{beam} on the surface due to the difference in WD (remember that the stage is tilted almost 70°), thus probing a different real position than suggested by the stage position coordinates recorded by the software. This exact consequence is, however, corrected for by the routine procedure of aligning one of the upper or lower edges such that it remains centred in the beam along the entire scan length in y (x constant). This is done by rotating the sample around ND (away from the preferred arrangement). However, such a rotation around ND will introduce the same, wrong rotation around ND in the detected orientation of the probed position.

Secondly, any position of the sample which in reality is not at the same WD as where the WD was probed and the focus adjusted, will not be in focus. The real resolution at these positions will thus be reduced, as a larger sample area will be probed and the amount of electrons incident on the (small) area of interest will be much lower. This may lead to the degradation of the Kikuchi patterns and overlap of Kikuchi patterns from neighbouring positions.

Thirdly, the computer algorithms used for calibration and indexation of Kikuchi patterns

use the WD as an input parameter. Recall that to calculate the direction of the crystal lattice plane normal $\mathbf{g}$, the positions $\mathbf{x}^{\pm}$ and $\mathbf{x}^{\perp}$ on the detector plane must be determined. These vectors could each be described as a sum of the pattern centre vector $\mathbf{x^0}$ and a vector in the detector plane. The pattern centre is used as an origin for the Hough transform, which detects the in-plane vectors through the variables r and ϕ. A shift in working distance ΔWD leads to an equal shift in the vertical position of the pattern and the pattern centre on the detector. This means that for a real working distance $WD(x, y) = WD_c + \Delta WD(x, y)$, with x, y being positions on the sample and WD_c being the working distance at the position where the focus was set and the indexation calibrated, the position of the pattern and the real pattern centre will be constantly changing as a function of the position on the sample being probed. However, as this is not calibrated for, the indexation will proceed with the fixed origin determined from WD_c, meaning that the measured distances and angles to the detected Kikuchi bands will be wrong. The consequence is a non-real change in calculated orientation, which is roughly equivalent to a rotation α of the sample around the tilt axis, the approximation is given through

$$\alpha(x, y) \approx \arctan \frac{\Delta WD(x, y)}{L} \tag{4.1}$$

where L is the detector-to-sample distance. The smaller L is, the less the approximation holds. A small L will give a large difference in the vertical shift between bands that are vertically close to the calibrated pattern centre and bands that are vertically far away in the first place. This should give a worse fit in the indexing routine.

It is very likely that the gradient that can be seen internally in the large crystals in many of the combo scans, Figure 3.1 (left) especially, is due to this phenomenon. The gradient across both crystals in the y-direction of this scan is 8° to 9°. If a detector-to-sample distance of 20 mm is assumed, this degree of tilt is what would be expected from a difference in WD of about 3 mm between the ends of the scan area. As far as the author understands, the orientation gradient should be equal for both grains and thus not have any effect on the calculation of disorientations. The non-real gradient therefore likely does not affect the quality of the disorientation results but should be kept in mind when inspecting the orientation maps from combo scans.

4.1.3. Geometric Post-Processing of Combo Scan Data

Using a monocrystalline FZ specimen with known crystallographic directions, the absolute orientations could be calibrated. For the JEOL, an older scan of a FZ specimen (not performed by the author) was used to find the calibration parameters. The calibration was then applied in post-processing for the combo scans. The stage scans were not post-processed because only relative orientations were of interest from these scans. From the scan of the FZ, correction factors of 3° around TD and 7° around ND were found. Since at this point in time it was not obvious to the author that the deviations were dependent on the sample mounting and therefore only

partly systematic, the same post-processing correction was applied to all samples. As it later turned out, any deviation around ND could be due to an angular offset of the EBSD detector around its own axis, which is roughly constant, as well as the more unpredictable deviation in ND caused by the unlevel sample, as described above. Deviations around RD and TD would be directly dependent on the sample mounting for each scan, i.e. also not entirely systematic, and RD would also have a contribution from slack in the instrument's mechanical tilt around this axis. It can be argued that no corrections should have been applied as long as these correction factors were not assuredly based on invariant data, which could not be guaranteed in this case. However, the corrected orientations are closer to what would be expected in terms of growth direction and boundary plane than the uncorrected data, indicating that a large portion of the correction factors found were systematic rather than variable. Regardless, a few degrees error in these orientations does not severely impact the results analysed here, as the focus is mainly on relative orientations rather than absolute.

4.2. Macroscopic Disorientations

4.2.1. Interpretation of the Results

The purpose of determining the evolution of the macroscopic disorientation was to test the hypothesis: do the bulk crystals obtain orientations which result in a more ideal grain boundary between them when dislocations are emitted from the boundary?

Considering Measurement 1 of Figure 3.8 individually, the hypothesis seems plausible, as the general trend definitely goes towards values closer to the ideal disorientation higher in the sample. However, Measurement 2 casts doubt over this outcome. When considering both measurements together, one may question both the trend towards ideality – because of the different slopes of the two measurements – and the real displacement from ideality – because of the discrepancy between the two measurements.

Ideally, an estimation of the noise levels should be performed, such as finding a standard deviation for the orientations or the standard deviation of the point-to-point disorientation within a grain. That is, however, time-consuming and requires the implementation of a method to calculate the average of orientations, which can be done but is not straight forward. Also, judging from how the disorientations distribute in plateaus with very small spread of disorientation values within each plateau, the noise is presumably quite low when taking the rather high number of data points used to find each median orientation into consideration.

It is enticing to compare the position of the jumps in disorientation value between different plateaus in Figure 3.8 with the position of the occurrence of the various subgrains observed in Figure 3.6. Likewise for the changes in disorientation occurring in the first millimetres above the seed in Figure 3.8. It is possible that the presence of subgrains skews the number of data points

for the bulk crystals to such an extent that the median values are also significantly skewed, and thus the disorientation is artificially altered. E.g. when a larger subgrain is detected by the algorithm, the set of data points assigned to the median selection of the main grain is reduced.

While some features seem to match up fairly well between the plot and map, like the jump at approximately 28 mm and the green subgrain at approximately the same height, other features are harder to link together. The precision of the positional measurements and the alignment of positions across different scans are also not exact, which makes the comparison a difficult and inaccurate exercise. One cannot on the basis of the available information draw any conclusions as to if there is a correlation or not between the jumps in macroscopic disorientation and the emergence of subgrains from the main boundary, or to if the general trend of the disorientation is towards the more ideal.

4.2.2. On the Method

4.2.2.1. Algorithm

One of the first steps in the data treatment used to generate the plot in Figure 3.8 is a CI filter. The purpose of the CI filter is to remove poorly indexed data points which could obscure the determined macroscopic orientation values and cast doubt over the trueness of the calculated disorientations. Ideally, the raw data would be of good quality and a CI threshold in the range of 0.6 to 0.8 could be used without removing too many data points. Unfortunately, the acquired raw data from the custom scans were of rather low quality. Using a CI threshold value of, for example, 0.5, would return poor results later in the process because too many data points were removed, making the median filter smoothing unstable. To have sufficient amounts of data points, a CI threshold of 0.2 was employed in the final calculations.

A poor confidence index does not necessarily correlate to a poor determination of the real orientation of a data point, but rather to the magnitude of the uncertainty. A measurement can therefore still be of use even if multiple CI values are low. In this case, a consideration of the scan data shows that there is good consistency between the indexed orientations within each grain and that the determined orientations are reasonable. It is thus concluded that the low CI threshold value likely does not severely affect the accuracy of the measurement, but an effect on the precision is likely at hand. However, the degradation of precision is counterbalanced by the relatively high amount of data points available for the median filter later on.

The median filter implemented does a good job of smoothing the orientation data while retaining the most important boundaries. An important parameter is the width of the window around each candidate. A smaller window will give a lesser smoothing effect, while a larger window will increase the run-time of the algorithm and the chance of erasing an edge (a GB) if the area it encloses (the grain) is smaller than the window size. Because the window used in this work was one-dimensional, it was necessary to include a higher order of nearest neighbours than

would be necessary for a two-dimensional window to obtain a good smoothing effect. Therefore, a rather wide window was chosen, stretching 5 nearest neighbours on each side of the candidate. With a step size of 100 µm, this makes the total window size 1.1 mm (11 data points). Using a window of this size or larger was particularly important because of the relatively high density of non-indexed or non-qualified (CI) data points in certain areas, which would cause trouble in finding a good value for the candidate when the window was filled primarily with NaNs.

To automatise the procedure of finding the disorientation between the two main crystals, an algorithm that would segment the data set into respective grains was included. This was mainly to ensure that when searching for the median orientations, data points that in reality belonged to relatively large subgrains would not skew the median values of the main crystals. Partly, it was to enable the option of also studying subgrain orientations with the same tool, however, so far this has not been done. Three features of this segmentation algorithm should briefly be discussed. One, the threshold value for point-to-point disorientations; two, the nearest-neighbour control of peaks exceeding the threshold; and three, the significant grain size rule.

The threshold value was put to 0.025 rad (1.4°). This value was chosen after visual inspection of some example disorientation profiles post-smoothing and found to give a sufficiently high threshold to exclude any peak detection due to Gaussian noise. Thus, any peaks detected would be due to SAGBs exceeding 1.4° disorientation, or due to impulsive noise.

The nearest-neighbour control serves to remove non-real GBs due to impulsive noise. However, there are identified bugs where, in some special cases, an actual grain boundary will be detected as noise by the algorithm. Take, for example, a situation where there are 3 points in a row where the point-to-point disorientation is exceeded, and one of the points is due to an actual GB while the others are noise. If a and b are two different orientations with disorientation higher than the threshold, then the sequence of measured orientations may be $a\ a\ a\ b\ a\ b\ b\ b\ b$, where $a\ a\ a$ and $b\ b\ b$ clearly are different grains. However, the nearest-neighbour control will not be able to find a position where the condition is fulfilled. For the purpose with which the method has been employed here, this shortcoming only causes a problem when the median orientations of the main crystals end up being skewed significantly because of incorporation of data points from nearby grains. The likelihood of this happening is presumably sufficiently seldom that it should not affect the overall macroscopic disorientation, except for skewing perhaps one or two data points.

The third point, the grain size rule, has the same effect as described for the nearest-neighbour control above: potentially slightly skewing the determined median orientations of the main crystals. This feature simply removes grains smaller than 3 data points wide (300 µm), because smaller grains than this cannot be associated with a true median orientation. Removing these small grains altogether thus makes the subsequent algorithms simpler. For the macroscopic disorientation purpose, this was assumed to be acceptable, because the number of data points

added to the set of orientations available for median selection for the main grain is relatively small (3 data points added to a set of almost 100 data points). However, if multiple grain boundaries in a row are skipped, and these are bordering one of the main grains, then this may actually significantly skew the median. It is not believed that this is the reason for the jumps discussed in Section 4.2.1, but the effect would be the same.

Performance-wise, the overall algorithm for finding the macroscopic disorientations has room for improvement. The most effective modification would be to change the algorithm for orientation comparison during the search for a median in a window. Whenever considering the closeness of orientation between two points, the current algorithm calculates the disorientation between the two orientations. This involves calculating the rotation matrices of each point and minimizing the set of 24^2 misorientation combinations, which is a very computing-intensive task. Additionally, this solution does, in theory, introduce the possibility of switching a candidate's orientation to an orientation that is far away in angular distance from the real orientation, but crystallographically equivalent. This does not pose a problem in this work, as ultimately only the disorientation is of interest, but could create unwanted effects if the same algorithm was used for a different purpose. In the alternative solution, the Euler angles which define the orientation are treated as the three coordinates in a three-dimensional Euclidean space, the Euler space. Then, the orientation distance can be compared much faster by simply comparing the Euclidean distance between the two points in the Euler space. The difference between these two approaches has also been outlined by Gupta et al. [33].

4.2.2.2. A Possible Fallacy

During the completion of this report, the author became aware of an article by Grimmer [37], which casts doubt over the legitimacy of the employed algorithm. Grimmer states that there are $24 \cdot 24 \cdot 2$ different descriptions of the same relative orientation of two cubic lattices. In the current algorithm, $24 \cdot 24$ different misorientations were calculated and minimised to find the disorientation, i.e. only half as many. The author has not been able to reach an understanding to whether or not the remaining 24^2 misorientations are exactly the same as those calculated – but merely described by the mathematical inverse – or if this additional half of the set contains unique misorientations that should have been calculated. If the latter is the case, the calculated disorientations are wrong. Because of the minimisation step in the calculation of the disorientation, the net result on the calculated disorientations would not be a huge shift from what has been presented here, but it is statistically probable that the value of 50 % of the data points in the plot would very slightly decrease. However, the disorientation calculation would be wrong by definition.

4.2.2.3. Acquisition Quality

The data acquired for use in the macroscopic disorientation was deliberately recorded by a stage scan routine in order to avoid systematic orientation gradients due to inadequate dynamic pattern centre calibration, as could be frequently observed as tiles in the IPF maps of combo scans. Because the beam axis is fixed and only the stage moves in this mode, the geometric distortions that the dynamic pattern centre calibration is supposed to correct for do not arise. This gives high confidence that the relative orientation recorded between the two crystals is not skewed by an altering of the median values due to artificial, repeating gradients in the orientation.

Oppositely, the rather large orientation gradients observed across the entire length of the scans slightly reduces this confidence. However, as discussed in Section 4.1, it is probable that these gradients are caused by a non-constant working distance and that the effect is likely equal for both grains, thus it should not alter the disorientations. Additionally, both measurements used to calculate the disorientations show very similar gradient levels.

4.3. Estimations of Noise and Systematic Deviations in the Beam Scans

A discussion of the limitations of the employed method for error estimation is warranted. Most importantly, using the disorientation between the orientation of a fixed point (the origin) and an array of orientations is not ideal for characterising neither the noise nor the systematic deviation. This is primarily because the disorientation is a one-dimensional absolute value that does not give any information as to in which direction the change in orientation is. (When evaluated without its disorientation vector.) Additionally, the origin orientation has been chosen arbitrarily and may not be centred at the expectation orientation, which would give the most correct results. Orientational noise is much more complex, seeing that the orientations not only are described by an axis in a three-dimensional space but also by another rotation around this axis. However, because mainly relative orientations (disorientations and angular distances) are considered in this report, and considering that the noise appears quite uniform (Figure 2.4), the precision of the noise estimation is presumably satisfactory. The advantage of this method is the simplicity with which it can be performed to give reasonably good absolute values, using the readily available features of TSL OIM Analysis 7.

The consistency of the s^2 calculations is good across all scans investigated and the noise can be estimated reasonably with the variance of $0.0299\,\mathrm{deg}^2$.

For the estimation of the systematic deviations, the b_1 values spread significantly, especially when also taking the values from the FZ specimen into account. The differences are large when comparing between scans and when comparing the horizontal profiles to the vertical

profiles within scans. However, comparing between the two grains internally in each scan, the differences are not significant. The explanation for this lies likely in the calibration of the dynamic pattern centre for the indexation of the scans. During a beam scan, the pattern centre of the Kikuchi pattern moves, and this movement must be calibrated and corrected for in order to accurately determine the true orientation of the crystal in each measurement point. An ideally calibrated indexation should result in an indexed scan with no non-real orientation gradient. For many of the recorded scans, the quality of the recorded calibration patterns and the resulting indexation is only moderately good. Some scans are therefore better calibrated than others, and most scans are apparently calibrated with different quality along the two different axes, resulting in differing gradients.

In order to achieve good error corrections, estimation of b_1 should be done individually for each scan. That is, however, time-consuming – and for some scans problematic due to the presence of real orientation gradients – and has therefore not been done in this work. Instead, as a compromise, the mean b_1 value has been used for the gradient error estimation, which should give a better estimation of the overall uncertainty than not employing an estimate of the gradient. Employing the square of the $b_1 dx$ or $b_1 dy$ estimators as a variance, as has been done in the uncertainty calculations, is unconventional. Though, considering the variable magnitude of the b_1 values, using the estimator in this sense is not entirely unheard of and does a good job of underlining the uncertainty of the estimations.

As was done for the combo scan data, also the beam scan data was post-processed to better calibrate the orientation. The mounting of the sample in the Zeiss Ultra microscope was less prone to errors, so the deviations should be less variable than for the JEOL instrument. The calibration factors were found by scanning a FZ specimen with known direction and then applied in TSL OIM Analysis 7. For the Ultra, the correction factors were 1° around TD, 2° around RD and 5° around ND.

4.4. Dislocation Generation from the Centre Boundary

Considering Figures 3.1 and 3.2, it is apparent that the $\Sigma 27\{1\,1\,5\}$ boundary acts as source for dislocation arrays. At several points, for example, at 12 mm and 22 mm in Figure 3.2, arrays of dislocations can be seen to flower from the grain boundary into the crystals on either side of the boundary. The fact that the arrays extend into both grains from roughly the same position is interesting. This means that there is either some inherent property of the GB at this position that has the potential to nucleate dislocation arrays on both sides of the boundary, or, that dislocations nucleated at one side of the boundary are able to traverse the boundary into the other grain. As noted in Equation (1.6), the transmission of a dislocation from one grain to another is theoretically possible as long as a grain boundary dislocation is generated to conserve the net Burgers vector.

In both the observed examples mentioned above, the array seems to start slightly lower down in one grain than in the other, on the order of perhaps 50 µm to 300 µm. Ervik et al. [18] observed that the Σ27 boundary dissociated into grains that in the two-dimensional cross-section could be perceived as triangular with $\Sigma 3^n$ sides, and that dislocation arrays could be punched out from the corners of the triangle, i.e. from the junctions between different Σ-boundaries. If a rather large triangle is present and a dislocation array is punched out into one grain from one corner and another array into the other grain from another corner, where the corners are vertically far apart, then the observations could be explained without the need for dislocation transmission across the GB. These triangles were on a similar scale as observed for the dislocation generation here.

The arrays extend from the GB in various angles, and often with changing directions. They do not seem to follow any specific crystallographic directions. This could indicate that the formation of the arrays happens in the wake of the growth front, which, due to e.g. convection, could be changing its shape and thus its influence on the array formation. Image forces that could attract or repel dislocations will be available at the growth front and could manipulate the movement of the newly formed dislocations.

4.5. Dislocation Microstructure and Observations of Subgrains

Figure 3.9 indicates that there is a correlation between the observations of dislocation arrays, dislocation clustering, and minor changes in the orientation of the crystal, i.e. the presence of subgrains. In Figure 4.1 the beam scan IPF map in inset (k) of Figure 3.9 has been overlain on an optical microscopy defect map to show the correlations between dislocation arrays and the detected subgrains. The match between the two maps is not perfect, due to the geometric distortions which occur during beam scan EBSD. Figure 4.2 shows a grain boundary map for the same area (right). The grain boundaries are coloured according to either their disorientation or their CSL relationship. Some identified subgrains have been denoted with roman numerals.

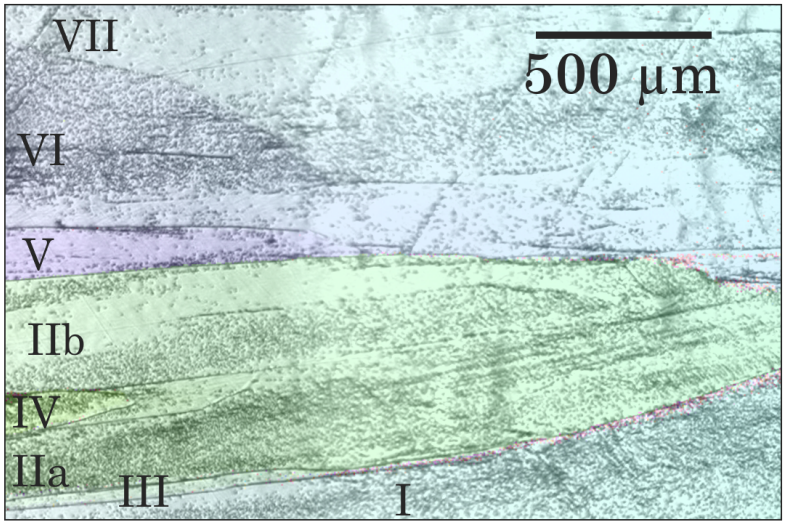

Figure 4.1.: IPF map of the scan in inset (k) of Figure 3.9 overlain on the optical microscopy defect map of the same area. Dislocation arrays can be seen to follow and be restricted by SAGBs.

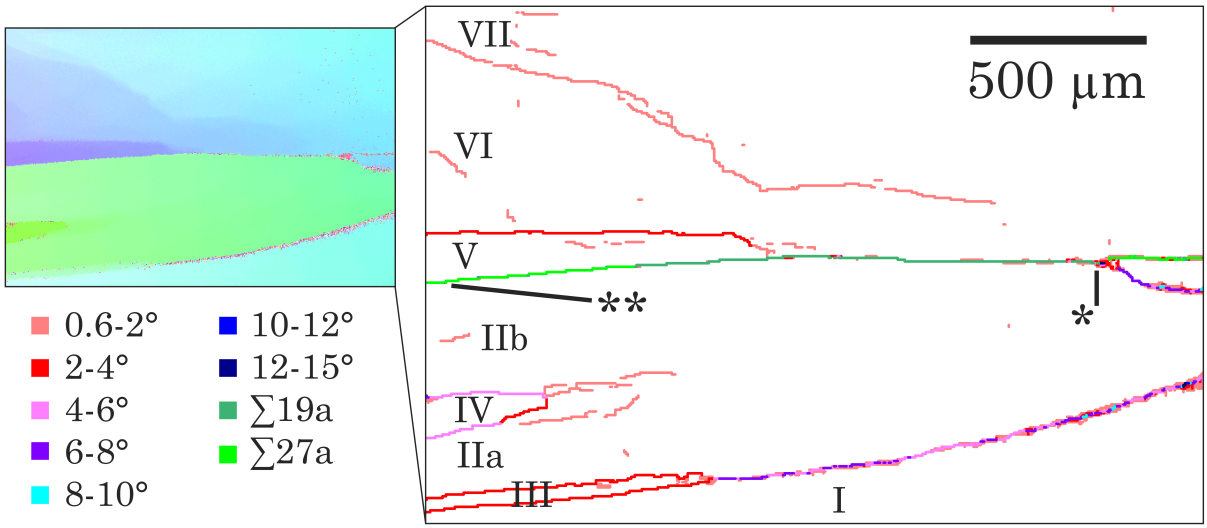

Figure 4.2.: IPF map of the scan in inset (k) of Figure 3.9, (upper left), and a grain boundary map of the same scan. The legend colours of the grain boundary map have no correlation to the IPF legend colours of the IPF map. The asterisks refer to the first (*) and last (**) measurement point of Figure 4.7.

The main GB, the $\Sigma27\{1\,1\,5\}$, is seen at the far right in the centre in Figure 4.2. It is detected as a $\Sigma19$ between subgrains IIb and VI/VII before it eventually is detected as a $\Sigma27$ again. Why it is briefly detected as a $\Sigma19$ is discussed in Section 4.7.3.

SAGBs of various disorientations have been detected by the software and can be observed in the figure. The majority of the detected SAGBs can easily be correlated to areas of unique orientation (colour) in the IPF map (upper left). Returning to Figure 4.1, relatively straight, solid boundary lines may be observed in the defect map along the detected SAGBs. These lines are likely the overlapping etch pits of the densely spaced dislocations that make up the SAGBs.

Closely inspecting Figure 4.1, several additional features can be discerned. The subgrain denoted IIb can be seen to have a long region of very low dislocation density, as well as a parallel long region of higher dislocation density. In fact, a dislocation array separates these two regions, potentially acting as a SAGB, dividing the subgrain into two individual subgrains of very similar orientation. This potential SAGB is not properly detected in the grain boundary map of Figure 4.2, however, an isolated line at the far left, next to the IIb notation, insinuates that there might be a disorientation between these two regions.

Chuang et al. [25] argue that dislocations in the lattice with Burgers vector equal to or opposite to the Burgers vectors of dislocations that constitute a dislocation wall, may be attracted to the wall and agglomerate there or annihilate. Thus the wall acts as a dislocation sink for some dislocations. Chuang et al. also argues that lattice dislocations with certain other Burgers vectors may be repelled by the wall.

It could be that in the mostly dislocation-free subgrain inside IIb (assuming these are

individual subgrains inside IIb), the majority of dislocations that would intercept the specimen surface have been drained to the surrounding dislocation walls because of Burgers vector relationships. Thus, the grain appears to be free of dislocations. Alternatively, this subgrain could have been more effectively drained of dislocations than the neighbouring subgrain during solidification. Subgrains with more dislocations after the initial solidification may suffer from increased multiplication during cooling, due to intersecting dislocations which form kinks and jogs that may act as multiplication sites. Thus becoming more densely dislocated in the end.

In the same figure, similar tendencies are visible in the smaller subgrain to the right of subgrain IV. The density in this subgrain is much lower than in the surrounding subgrains. In Figure 3.2, multiple other features that are likely subgrains can be seen to follow the same trend. Some are densely dislocated, while others appear essentially dislocation free.

4.6. Disorientation Evolution of Small-Angle Grain Boundaries

Relatively low in the sample, at 12 mm (inset (e) in Figure 3.9) and 18 mm above the bottom of the seed (inset (d) in Figure 3.9), dislocation arrays can clearly be seen to nucleate from the boundary. However, inspecting the orientation maps of these locations, no significant orientation changes indicating any SAGB formation can be detected across the arrays.

Observing the area from inset (d) at approximately the 18 mm mark in Figure 3.2, the aggregations of dislocations look a lot like those observed by Chuang et al. [25]. Being disordered and wavy at first, they eventually become thinner and more defined lines. However, the disordered regions observed by Chuang et al. extend only some hundred micrometres, whereas those observed here may persist for well above a millimetre before turning more ordered. Chuang et al. observed the newly formed SAGBs to increase in disorientation with height. It is speculated that this is also the case here. The disorientation across the SAGBs might be below the detection limit of the EBSD acquisitions in the areas investigated, but could be increasing higher in the sample. In the findings of Chuang et al., the disorientation rises from below 0.5° to above 3° in only 600 µm. If such a steep rise in disorientation was present in the two arrays investigated here, it should be detectable. However, as visible from the frame of inset (d) in Figure 3.9, only the disordered beginning of the array is covered by the beam scan. It is sensible that the rise in disorientation is less steep for an array that is unordered for a longer distance. The growth rate used by Chuang et al. is higher than industrial growth rates. One would assume that a higher growth rate leads to longer distances of unorder because the cooling would be faster and the dislocations would have less time to arrange. The growth rate of the samples inspected here is unknown but should be even higher than that of Chuang for this assumption to hold true.

From 25 mm to 29 mm above the seed bottom is another interesting region along the centre GB. The area is covered in insets (f-h) and (l) in Figure 3.9. The same area has been depicted in Figure 4.3, which shows overlain IPF maps on a defect map (top), and grain boundary

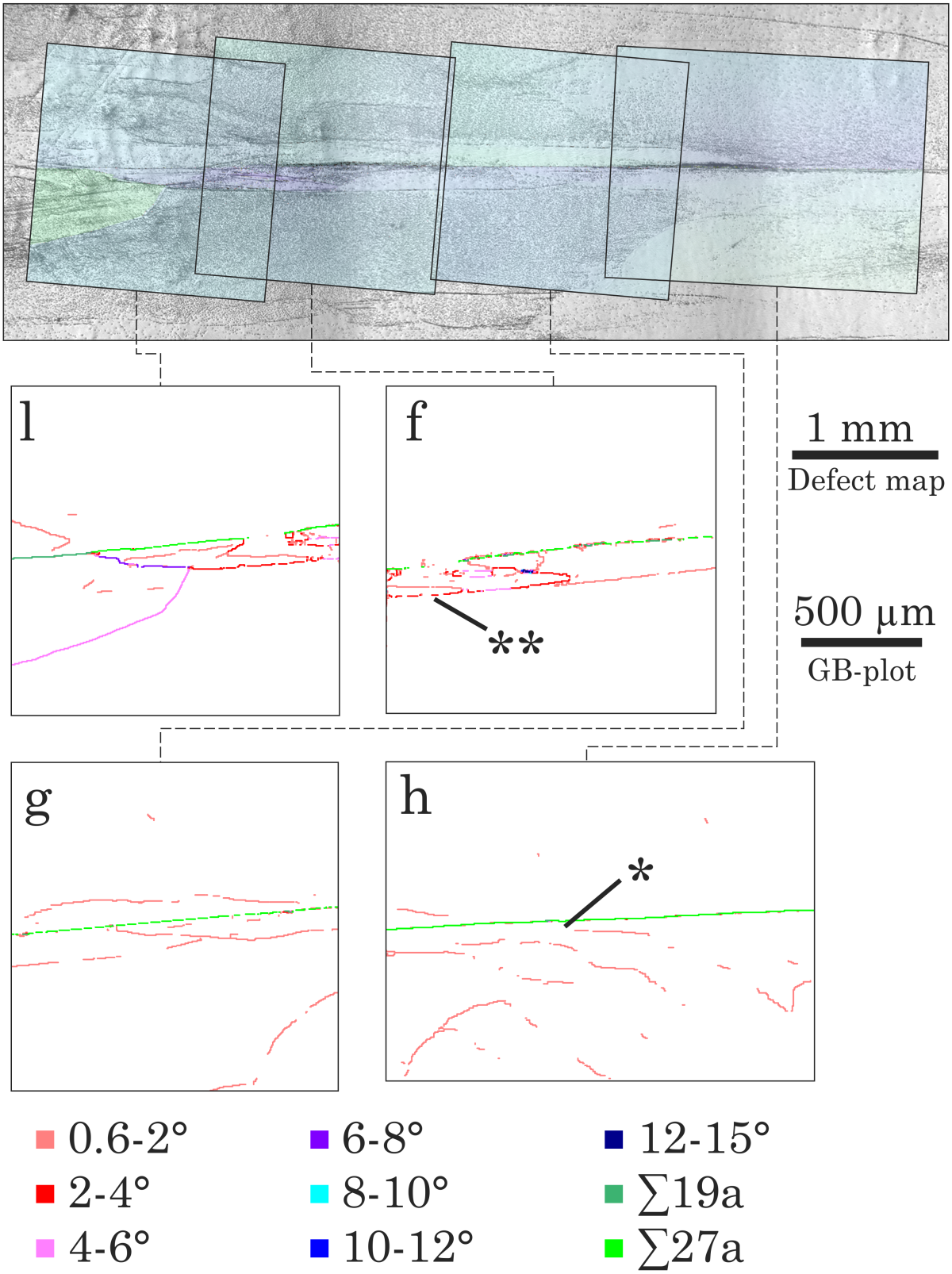

Figure 4.3.: Defect map of an area along the Σ27{1 1 5} overlain with IPF maps of the scans in insets (f-h) and (l) of Figure 3.9 (top). In the insets below are grain boundary maps of the same scans, denoted with the same letters. The evolution of consecutive SAGBs can be followed through all of the insets. The asterisks refer to the first (*) and last (**) measurement point of Figure 4.4.

maps for the same EBSD scans in the insets below. For ease of referencing between figures, the insets in Figure 4.3 have been named with the letter of the corresponding insets in Figure 3.9.

The area is interesting because of the clear difference in dislocation density on both sides of the centre grain boundary. Considering the grain boundary maps in Figure 4.3, somewhere in the middle of inset (h) in the grain in the lower half of the scan, a SAGB either nucleates or a subgrain enters from outside this cross-section. The SAGB grows more or less vertically (horizontally in the figure) but eventually seems to change direction, growing in towards the centre GB and terminating in the middle of inset (g). However, shortly after the change in direction, a new SAGB seems to rise roughly in the same tracks as the previous. This SAGB increases gradually in disorientation and can be followed into insets (f) and (l), where multiple new subgrains appear internally of the subgrain it encloses.

Figure 4.4 shows the evolution of disorientation along these SAGBs between the positions marked by asterisks in Figure 4.3 insets (f) and (h). The standard deviation for each data point is calculated to 0.3°. From the graph, it seems that the first SAGB exhibits a slight increase in disorientation. The first data point, at below 0.5°, might be just below the area where the subgrain enters the cross-section (if that is the case). When the first SAGB is succeeded by a different SAGB after roughly 1200 µm, the disorientation drops a bit and remains low until it increases slightly for two data points around 2500 µm – likely due to a new internal subgrain not very visible in the figure – and then jumps to above 4° when reaching another more visible internal subgrain in inset (f). Also the disorientation evolution of the boundary between subgrain I and the rightmost part of subgrain IIa (before the appearance of subgrain III) was probed and found to be roughly constant, as far as could be estimated from the noise levels, with a disorientation of $(5.8 \pm 0.3)°$. Generally, these SAGBs seem to be quite mature with relatively little evolution of disorientation for each individual SAGB. Detected changes in disorientation are rather shifts between different but related subgrains.

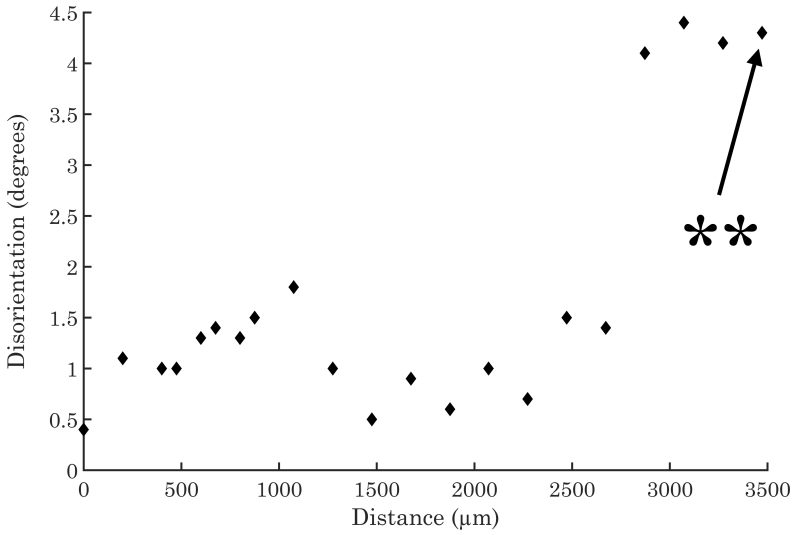

Figure 4.4.: Graph showing the evolution of the disorientation between the positions marked by asterisks in Figure 4.3.

Interestingly, from the microstructure seen in the defect map in Figure 4.3, there seems to be a subgrain in the opposing crystal that almost mirrors the subgrains just described. However,

no visible change in orientation can be observed in the orientation maps or grain boundary maps. Seeing how dislocation densities and arrays so far have been observed to correlate very well with different orientation domains in the orientation maps, it is not unlikely that there also exists one or more subgrains in this region, but of a disorientation that is below the detection limit.

4.7. Subgrain Rotations

4.7.1. Approximating the Tilt Around the Common ⟨1 1 0⟩ Axis

Because the ideal CSL boundaries are often described by tilts around the ⟨1 1 0⟩ axis, it is of particular interest to see how the tilt of the real boundary around ⟨1 1 0⟩ differs from the ideal, as well as how the formation of subgrains alters this tilt. However, the disorientation does not necessarily give the best indication of this, as the disorientation may be around an axis $\boldsymbol{\eta}_{\mathbf{d}}$ which does not necessarily correspond exactly to ⟨1 1 0⟩. Decomposing the disorientation to find the misorientation contribution from the tilt component around ⟨1 1 0⟩ could therefore shed further light on the nature of the non-ideality of the boundaries, although the method is unconventional. Approximating this component by the angular distance between {1 1 0} poles has been attempted. The data is presented in Figure 4.5, Figure 4.6 and Table 4.1, and will be discussed below.

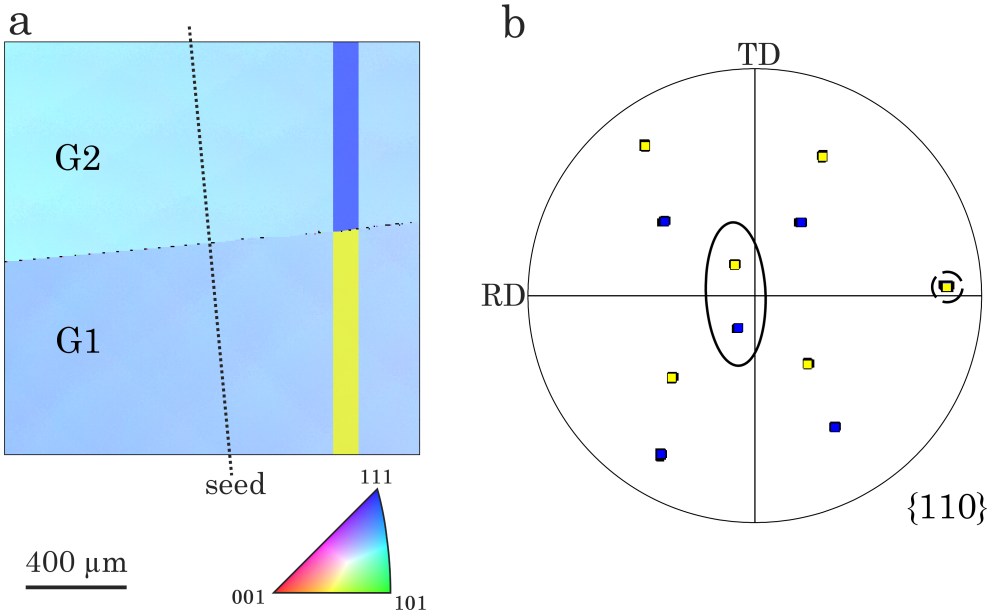

Figure 4.5.: IPF map of the top part of the seed around the Σ27{1 1 5} GB (a) and pole figure showing the {1 1 0} poles of the area probed in the IPF map (b). The dotted line in (a) indicates the top of the seed (i.e. seed is to the right of this line). The probed section in (a) is coloured with the legend colours of (b), which have no correlation to the IPF legend colours of (a). The dashed circle indicates the common pole, while the poles encircled by an ellipsis are perpendicular to the common pole.

Figure 4.5 (a) shows an IPF map at the top region of the seed (this map is not included in Figure 3.9). The position of the top of the seed is indicated by the dotted line. A nomenclature to distinguish between the two main grains of the bicrystal is introduced, where one has been denoted G1 and the other G2. A section of the map in Figure 4.5 (a) (the section that has been probed) has been colour-coded in reference to the legend colours of the pole figure in (b). It is stressed that the legend colours of (b) do not have any correlation to the IPF legend of (a). The pole figure in (b) shows the $\{1\,1\,0\}$ poles of the two grains of (a), with the common pole of the two grains indicated by the dashed circle. The poles encircled by an ellipsis are perpendicular to the common pole. If the pole of each grain that make up the common pole were at the exact same position, then the angular distance between the $\{1\,1\,0\}$ poles perpendicular to the common pole would be entirely due to a rotation around the axis of the common pole. The angular distance between the two poles encircled by the ellipsis is $(31.9 \pm 0.3)^\circ$, where the uncertainty is the standard deviation calculated in accordance with Equation (3.2). This value is relatively close to the ideal of 31.59° but it is quite far from the range of disorientation values between 30.7° to 31.1°, which were found in the seed in Figure 3.8, although it is possible within 3 standard deviations. However, it should be kept in mind that the angular distance is merely an approximation of the disorientation.

A similar representation is given in Figure 4.6 for the area in inset (k) of Figure 3.9. Subgrains are denoted by Roman numerals like in Figures 4.1 and 4.2. A clear grouping of the subgrains into two groups is seen in the pole figure and these groups correspond to the parent grain of each subgrain: subgrains I, IIa, IIb, III and IV are a subset of G1, while V, VI and VII are a subset of G2. The angular distances between some of the poles encircled by the ellipsis are given in Table 4.1.

Table 4.1.: Angular distances between $\{1\,1\,0\}$ poles for the grains and subgrains in Figures 4.5 and 4.6.

Subgrains	Angular distance
G1-G2	$(31.9 \pm 0.3)^\circ$
I–VII	$(26.5 \pm 2.9)^\circ$
V–VII	$(6.7 \pm 0.8)^\circ$
VI–VII	$(2.1 \pm 0.4)^\circ$
V–VI	$(4.6 \pm 0.3)^\circ$
IIb–IV	$(5.9 \pm 0.3)^\circ$
IIa–IV	$(3.9 \pm 0.3)^\circ$
IIa–III	$(2.9 \pm 0.3)^\circ$
I–III	$(3.2 \pm 0.3)^\circ$
I–V	$(33.4 \pm 1.0)^\circ$
V–IIb	$(28.7 \pm 0.3)^\circ$
I–IIa	$(6.5 \pm 0.3)^\circ$

As can be seen from Table 4.1, the angular distance I-VII of $(26.5 \pm 2.9)^\circ$ is lower than the distance of $(31.9 \pm 0.3)^\circ$ between the seeds, while the distance I-V of $(33.4 \pm 1.0)^\circ$ is higher. The distance between IIb and V, i.e. the local disorientation component along $\langle 1\,1\,0 \rangle$ for the centre GB is $(28.7 \pm 0.3)^\circ$, which is also lower than the distance between the seeds. Seeing that there are dislocation arrays at an extent far outside the scanned area of Figure 4.6, as can be seen in the defect map in, for example, Figure 3.9, it is reasoned that neither subgrain I, nor VII, holds the orientation of the main crystals on either side (G1 and G2). Rather, they are likely subgrains (as

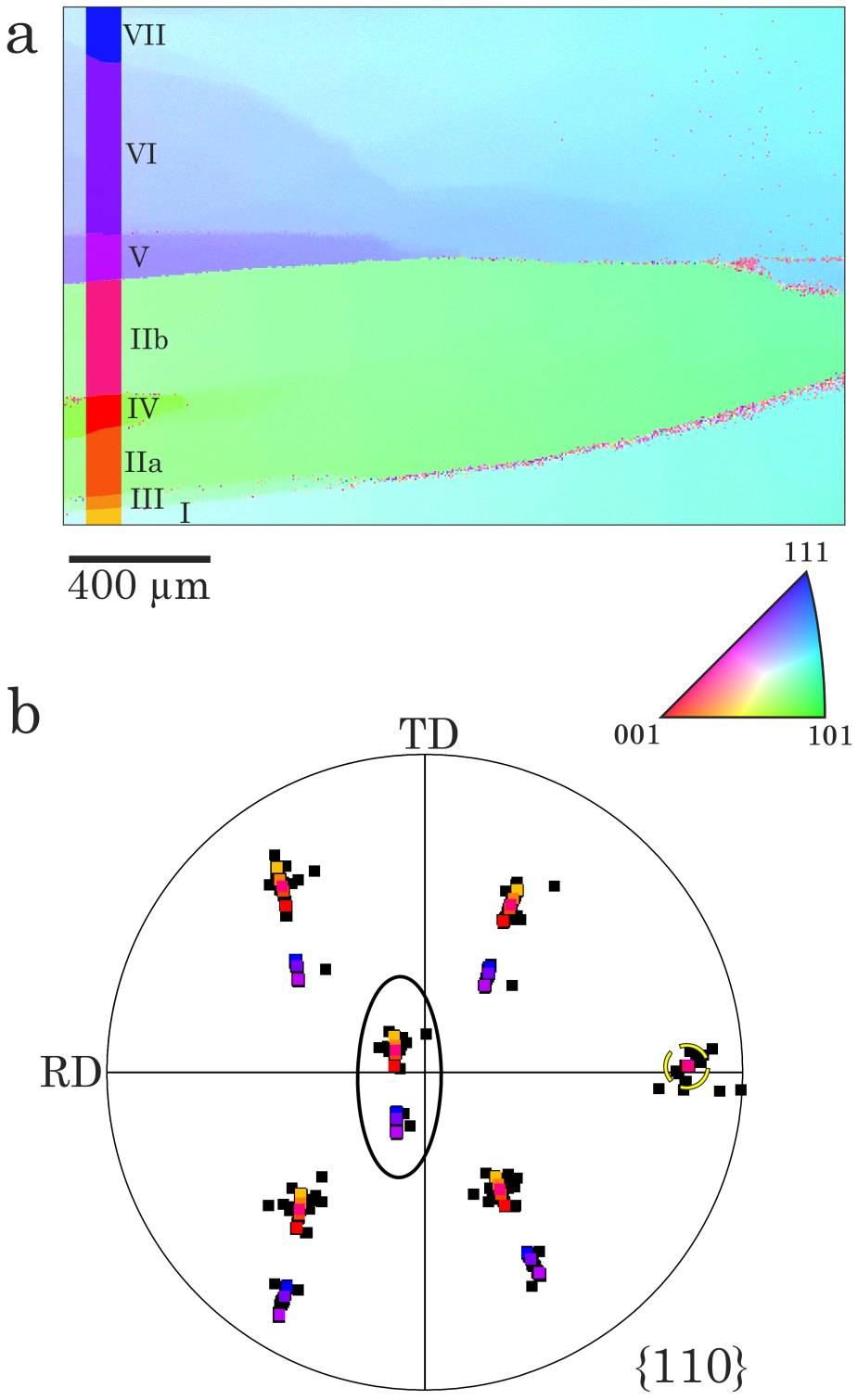

Figure 4.6.: IPF map of the scan in inset (k) of Figure 3.9, (a), and pole figure showing the {1 1 0} poles of the area probed in the IPF map (b). The probed section in (a) is coloured with the legend colours of (b), which have no correlation to the IPF legend colours of (a). The dashed, yellow circle indicates the common pole, while the poles encircled by an ellipsis are perpendicular to the common pole.

have been assumed so far). The angular distance around $\langle 1\,1\,0 \rangle$ for adjoining subgrains can be seen to be on the order of 2° to 7°.

The approximation is, of course, not perfect, as the poles making up the common $\{1\,1\,0\}$ pole does not stack perfectly, as can be seen in Figures 4.5 and 4.6. Thus is the common axis not perfectly defined. The difference from perfect stacking is, however, rather small, making the approximation viable. This approach is much simpler than the alternative method of averaging the orientation of each subgrain and calculating the disorientation vector. TSL OIM Analysis 7 does offer the possibility to perform such a method but is not able to distinguish each subgrain as an individual grain to average. Software such as MTEX may offer the required freedom to manually select the subgrains, but would still be vastly more time consuming than the employed approach.

The uncertainties stated in Table 4.1 reflect the dependence on the distance between the probed positions in the uncertainty calculations very well. The angular distance I-VII is associated with a very large uncertainty due to the probed positions being on the far ends of the vertical axis, while the uncertainties of the angular distance of subgrains adjacent to each other are much lower. However, the fact that the common pole is relatively homogeneously defined for all subgrains indicates that the vertical gradient in this scan is of low magnitude. Thus is the uncertainty stated in Table 4.1 likely exaggerated.

4.7.2. Directions of Subgrain Rotations

Considering the G1 subgrains isolated from the G2 subgrains, Figure 4.6 shows a clear rotational trend within each set of subgrains. For the G1 subgrains (subgrains I to VI), the closer the subgrain is to the CSL GB, the more the orientation of each subgrain has been rotated from the orientation of the G1 seed towards the orientation of the G2 seed. An exception for this is IIb, which rotates oppositely of this in relation to IIa and IV, but still holds true relatively to I, III and the seed. Also for the G2 subgrains (V to VII) the orientation is farther away from the G1 seed the closer the subgrain is to the GB. The orientations here are, however, so close to the orientation of the G2 seed that it cannot be properly distinguished in which direction relative to the G2 seed orientation the rotation is in. It may seem as if the VII orientation lies between the G1 and G2 orientations while the V orientation is outside the G2 orientation, the latter thus having rotated away from both seed orientations.

An interesting aspect of the rotations observed, is that the first subgrain across the centre GB might seem to attempt to match the rotation of the subgrain opposite of the GB (i.e. V is rotated in the same sense as IIb), while the subgrains in between the bulk crystal and the subgrain adjoining the centre GB relaxes the orientation back to the orientation of the seed by rotating oppositely as a function of distance from centre GB, on each side of the centre GB. This observation holds true if it is such that the true VII orientation does not lie between the G1 and

G2 orientations, but rather slightly outside. If not, the nature of the subgrain rotation may be more complex, or random, than what can be described based on these data. Multiple groups of subgrains must be examined to have sufficient statistical basis to draw any conclusions on this.

4.7.3. Subgrain Growth Directions and Effects of Subgrain Formation on the Local CSL Character

As briefly mentioned, Figure 4.2 reveals that the $\Sigma27\{1\,1\,5\}$ boundary for a stretch rather has the character of a $\Sigma19$a boundary. This is again likely due to the relative rotation of subgrains on either side of the boundary. The net reduction in tilt angle around $\langle 1\,1\,0\rangle$ makes the Brandon criterion unfulfilled for a $\Sigma27$a boundary, but it is fulfilled for a $\Sigma19$a. Figure 4.7 shows the disorientation evolution across the centre GB between the two positions marked by asterisks in Figure 4.2. The values scatter a bit, but can generally be grouped into a lower and a higher plateau. The jump between the plateaus happens at around 1000 µm and corresponds exactly with the rise of subgrain V in the centre of Figure 4.2. It is not clear why the software continues to detect the $\Sigma19$a for a few hundred µm after the rise of subgrain V and the abrupt change in disorientation. The $\Sigma19$ boundary is associated with lower energy than the $\Sigma27$, which would imply that once the transformation to a $\Sigma19$ has occurred, it would be energetically favourable for the GB to remain a $\Sigma19$.

Also, since $\Sigma19$a has a boundary plane $\{1\,1\,6\}$, which is very close to $\{1\,1\,5\}$, describing the GB as a $\Sigma19$a for the stretch with a disorientation of roughly 26° makes sense. Remember, however, that the centre GB is two-dimensional and extends in and out of the surface plane of the sample and therefore has a much larger surface area than what is one-dimensionally represented in this cross-section. The $\Sigma19$a is thus likely only a local phenomenon, occurring due to the behaviour of local subgrains, with the majority of the boundary staying as a $\Sigma27\{1\,1\,5\}$. Figure 4.8 gives an impression of the extra dimension (in/out of plane) that must be considered.

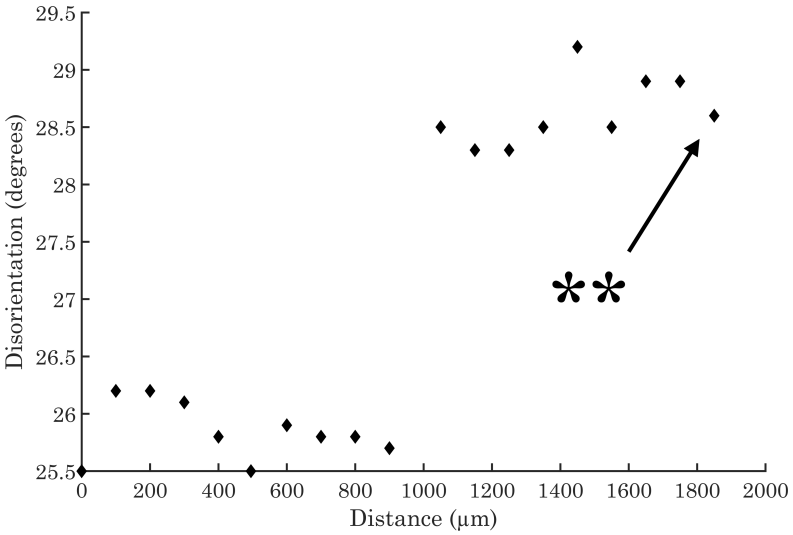

Figure 4.7.: Graph showing the evolution of the disorientation between the positions marked by asterisks in Figure 4.2.

In Figure 4.8, image scan photographs after the first and second defect etch are compared. The second etch was of shorter duration, and this photograph can be seen to have slightly less pronounced dislocation arrays. More strikingly, many features are observable in both graphs, but at different heights. This is due to the removal of material due to grinding and polishing between the two etch sessions, which means that we are looking at two different, parallel planes of the sample, spaced 0.45 mm apart. A random selection of these features are indicated by arrows. The change in position of the features can be as large as 3.5 mm vertically. This roughly corresponds to a growth direction of the features (subgrains) that is at an 8° to 9° angle to the vertical axis of the sample surface. However, recall that the sample specimens were not cut vertically along the growth direction, but at an angle of this magnitude. The direction of subgrain growth may therefore either be roughly parallel to the macroscopic growth direction or angled 16° to 18° to it. There is reason to believe that the former is the case. Judging from Figure 3.2, the tendency seems to be that the SAGBs start quite angled to the centre boundary and then align more in the vertical direction as they grow. Combined with observations by Oriwol et al. and Chuang et al. that the subgrains are elongated and pillar-like in the growth direction, and that SAGBs grow parallel with the growth direction, this suggests that also the SAGBs observed here adapt to grow parallel to the growth direction, despite having an origin angled to this axis. However, as the inspected CSL grain

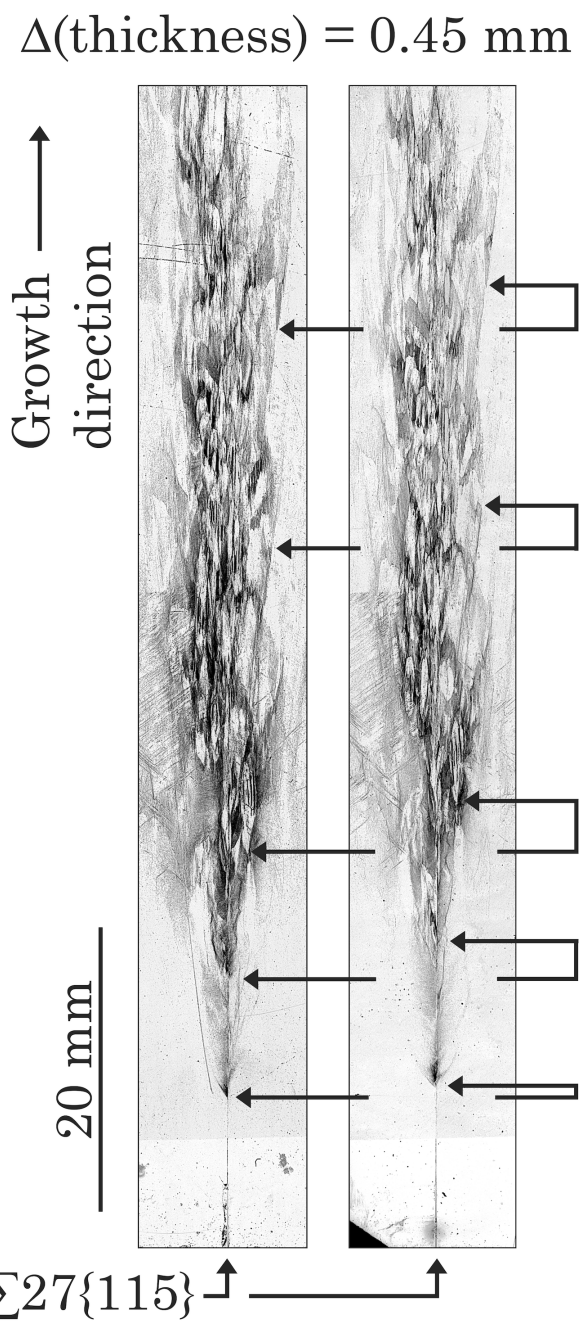

Figure 4.8.: Two defect maps of the Σ27{1 1 5} boundary showing the vertical cross-section of the grain boundary at two slightly different, parallel planes, with the distance between the planes given by Δ(thickness). The arrows indicate how many features can be found in both maps but at different heights.

boundary is approximately vertical, the pillar-like growth from the grain boundary is not easily observed. As described, the dislocation walls seem to rise from the centre GB at an angle, before turning more and more towards the growth direction. At this point, the subgrains could continue a pillar-like growth along the macroscopic growth direction, but what likely occurs is the impingement of the subgrains that have been nucleated at a low height with other subgrains nucleated higher up the boundary. Consequently, a microstructure emerges like the one observed for the $\Sigma 27\{1\,1\,5\}$, seen in, for example, Figure 4.8: a fluttering bouquet of subgrains up along the boundary.

4.8. A Hypothesis for Subgrain Rotation

The mechanism proposed by Oriwol et al. [21] where a dislocation generation at a grain boundary near the solid-liquid interface due to thermo-mechanical stresses is assumed, seems to fit well with the observations of this work. In their proposed mechanism, energy-reducing dislocation walls are built by gliding dislocations that agglomerate. The dislocations could also be climbing. As Chuang et al. [25] argue, the conditions close to the solid-liquid interface should be good for both types of dislocation movement, and the incorporation of dislocations with equal Burgers vectors into an array is energetically favourable. The high dislocation density of the walls results in a rotation of the lattice, and thus the wall becomes a SAGB. Oriwol et al. further describe the subgrains to have the axis of rotation parallel to the growth direction. This coincides fairly well with what is observed here.

The observations made in this work insinuate that there could be a dependency between the rotation of the subgrains in one crystal and the rotation of the subgrains in the other crystal. However, some of the evidence is diffuse, notably the position of the $\{1\,1\,0\}$ poles of the G2 subgrains relative to the pole of the G2 seed. A mechanism explaining how the rotation could be dependent between subgrains internally in a crystal, as well as across a GB is described in the following:

A location at the CSL boundary acts as a dislocation source during solidification, as described above, punching out dislocations of same or similar Burgers vector into one of the crystals. The dislocations are highly mobile in the wake of the growth front and several of the generated dislocations traverse the CSL boundary into the other crystal. In both crystals, the dislocations form arrays like described by both Oriwol et al. and Chuang et al. [21, 25]. Because of the high degree of symmetry between the crystals and the similar genetics between the dislocations (coming from the same source), the rotations induced by the newly formed SAGBs in both crystals are in the same direction. The magnitude of the rotation depends on the dislocation density in the boundary, and the magnitude therefore tends to be higher for SAGBs closer to the centre GB (closer to the source) than for SAGBs further into the bulk crystal.

The topic of dislocation transmission across grain boundaries is very complex and the author has not been able to delve sufficiently far into the matter to properly discuss the likelihood of this phenomenon in the situation described here. In an alternative edition of the hypothesis, the dislocations do not have to traverse the boundary but are generated in each crystal from the same site or different sites. In the case of different sites, the relation between Burgers vectors in each crystal could be preserved by a relation between the generation sites. Such a preservation could perhaps occur in the examples of triangular dissociations, as observed by Ervik et al. [18]. Also the theoretical feasibility of this alternative deserves a more thorough consideration than what has been found time for.

The real case would be more complex with e.g. the formation of new SAGBs from new sources due to e.g. impingement between subgrains, which could explain why the rotational sense and the magnitude as a function of distance from the centre GB do not strictly follow the proposal of the above hypothesis in the observations that have been made.

4.9. Other Boundaries

A short discussion of how the observations made for the $\Sigma27\{1\,1\,5\}$ boundary transfers to the other boundaries, that have been more shallowly investigated, is warranted.

The subgrain formation around the $\Sigma27\{5\,5\,2\}$, Figure 3.5, seems to be more restricted to only one side of the boundary. The formation is not completely restricted to one of the crystals, but the extent in the left crystal is much larger than in the right, whereas for the $\Sigma27\{1\,1\,5\}$, Figure 3.1, the extent is relatively symmetric. It could be that boundary has a much higher tendency to generate dislocations in one of the crystals and that the dislocations have limited possibility to traverse the boundary.

Inspecting the $\Sigma3\{1\,1\,2\}$, Figure 3.4, the trend is somewhat similar. There are definitely dislocation arrays on both sides of the centre GB, but they extend much further into the right crystal. Also, the subgrains here appear larger and less densely dislocated than for the two $\Sigma27$ boundaries.

In the case of the $\Sigma3\{1\,1\,1\}$, the situation is more complex and not properly comparable because of a strong dislocation source right next to the GB, as can be seen just to the left of the indicated GB in Figure 3.3. However, it is interesting that a generation of dislocations immediately at the top of the seeds can be observed from the CSL, which cannot be observed for the other boundaries. This is especially interesting because the $\Sigma3\{1\,1\,1\}$ boundary is considered to be the least harmful.

The orientation maps from combo scans do not offer good possibilities for discussing the rotations of the subgrains. However, comparing the IPF map contrast between Figure 3.6 and the maps in Figure 3.7, it appears that the contrast is stronger for the $\Sigma27\{1\,1\,5\}$ than for the others, indicating that the magnitude of rotation should be less for the samples in Figure 3.7.

4.10. A Note on the Lifetime Maps

Even though the lack of surface passivation will severely reduce the measured carrier lifetimes in the relatively high lifetime areas (blue in Figures 3.1 and 3.3 to 3.5), it is still clearly visible that the CSL grain boundaries have an adverse effect on the electronic properties in their surroundings. It is also apparent that some grain boundaries have a more severe effect than others, with the $\Sigma 27\{1\,1\,5\}$ being the worst by far. Unfortunately, due to the size of the laser spot, the resolution is not good enough to judge the observed subgrains and SAGBs individually.

The slight improvement in measured lifetimes around the GBs in the red zone can likely be attributed to internal gettering of iron (Fe) from solution to the GB and defects. It is probable that this region contains high amounts of dissolved Fe that has diffused up through the seeds from a Si plate on which the seeds were standing during the melting and re-solidification. This plate had not been cleaned by etching before the process, even though it had been sawn, thus being a source of Fe contamination.

The intermediate lifetime areas in the bottom of the sample represent the seeds, which are n-type, which is associated with higher lifetimes than p-type material like the bulk. Peculiarly, inspection of Figures 3.1 and 3.3 to 3.5 gives the impression that the seeds are approximately 2 mm larger in the lifetime maps than in the defect density maps. In reality, this is not the case, but an artefact of the measurement. Two hypotheses that may explain this are put forward:

One, this "extended region" is composed of material from the seeds that was only briefly melted before recrystallisation, thus not having been subject to proper mixing by convection and existing primarily of the same n-type material as the seeds.

Two, the presence of n-type material adjacent to p-type material creates a weak, vertical p-n-junction which somehow affect the charge carriers in the vicinity of the junction in such a way as to extend their lifetime.

Additionally, two hypotheses that have been rejected, are that there has been a diffusion of donor dopants from the seeds into this region at elevated temperatures after the recrystallisation – rejected on the basis that the colour gradient does not match the expected profile associated with Fick's laws – and, that the artefacts are a convolution effect due to the size of the excitation area of the laser probe – rejected on the basis that many finer features are clearly visible in the maps.

A deeper investigation into this phenomenon has not been performed, as it is outside the scope of this thesis.

5. Conclusions

Four bicrystals with artificially grown CSL-type grain boundaries were investigated with regard to the electronic properties in the vicinity of the grain boundaries, the angular imperfection of the boundaries, and the evolution of dislocation arrays from the boundaries. In-depth investigations were performed on the $\Sigma27\{1\,1\,5\}$, whereas more superficial investigations were performed on the $\Sigma27\{5\,5\,2\}$, $\Sigma3\{1\,1\,2\}$, and $\Sigma3\{1\,1\,1\}$ boundaries.

All boundaries were found to reduce the lifetime in an area along the boundaries. The extent of this area is larger for some boundaries than others, with the $\Sigma27\{1\,1\,5\}$ exhibiting the most severe extent of degraded area. The extent of the degraded areas correlates well with observations of densely dislocated areas.

The densely dislocated areas are composed of an ensemble of subgrains, which appear to be formed as a result of dislocation arrays being punched out from the centre CSL boundary. These arrays, which form dislocation walls and small-angle grain boundaries around the subgrains, arise from the centre boundary at various angles and turn gradually into a more vertical direction. The dislocation density internally in detected subgrains is relatively homogeneous, but large differences in density are seen between different subgrains. It is not clear whether this is due to actual density differences or differences in the dislocation character between subgrains which leaves the dislocations undelineated by the Sopori etch.

The evolution of the disorientation between the bulk of the two main grains (the macroscopic disorientation) of the $\Sigma27\{1\,1\,5\}$ bicrystal was probed as a function of the crystal height. It could not be decisively determined whether or not the disorientation evolved to become more ideal higher in the ingot. Several jumps between disorientation plateaus were observed. These could either be artefacts of the median technique used for finding the orientation at each height or actual orientation fluctuations arising during growth.

Also the disorientation evolution of some SAGBs and dislocation arrays was inspected. Where the disorientation was of a magnitude that could be detected, the disorientation remained essentially constant, except for some jumps. These jumps could be correlated to the observation of new subgrains along the measured array, e.g. there was a new boundary being measured for each jump. The probed arrays that could be traced all the way to the centre GB did not show any disorientation above the noise levels. It is assumed that these are developing SAGBs that are in a too early stage to be detectable.

It was found that adjacent subgrains within a parent crystal seemingly share a direction of

rotation relative to the parent crystal. It is hypothesised that this can be attributed to the origin of these dislocation arrays being the same or related, thus sharing the same Burgers vector. The observations insinuate that such a rotation dependency between subgrains might also exist across the centre GB, for adjacent subgrains in the other crystal. Such a cross-boundary dependency may be obtained through a shared dislocation origin in one grain where some of the dislocations are transmitted to the other, or, by related origins on both sides of the boundary. The statistical sample is, however, far too small to draw any conclusions.

The character of the centre GB – the disorientation, boundary plane and CSL type – was found to be locally dependent on the behaviour of the local subgrains on either side of the boundary. No decisive conclusion can be made as to whether or not the behaviour of the subgrains deterministically seeks to reduce the energy of the centre GB.

6. Further Work

- Ideally, much of the orientation mapping should be redone with the improved settings and routines that have been discovered and discussed in this thesis, this would help reduce uncertainty and speculations.
- The dislocation arrays should be inspected more closely with respect to the geometry of the etch pits, possible Burgers vectors and possible slip planes. This could help with identifying the types of dislocation sources, as well as explaining the rotational sense of the subgrains.
- Akin to the previous point, one or more subgrains should be selected and followed across multiple cross-sections, ideally to their origin (presumably at the centre GB), to properly inspect the disorientation evolution, dislocation character and rotational character of subgrains.
- The current slabs were cut for a different purpose (in-situ investigations). For similar post-mortem work like that described in this report, slabs could be cut thicker and exactly vertical. Areas of interests could then be identified and inspected through both horizontal and vertical cross-sections, which would help in understanding the three-dimensional aspects of the subgrain formation.
- Grain boundaries could be fabricated that are at an angle rather than vertical. Vertical CSL boundaries like those investigated here are a very special case, in reality, most CSL boundaries are angled to the vertical due to their crystallographic restrictions. Especially interesting for angled grain boundaries is what happens to dislocation arrays formed on the underside of the grain boundary versus those formed on the top.
- A lot of the in-depth work done on the $\Sigma 27\{1\,1\,5\}$ could be done on the other CSL boundaries for comparison.
- The macroscopic disorientation calculations should be further inspected to find out more about how the data treatment affects the end results. E.g. how would the result be without filtering, what is the variance of the orientations of the main grains prior to selection of the median, and how would a selection based on averaging rather than the median affect the result.

- In general, disorientation inspections in related work should include more emphasis on the disorientation axis, to observe if the axis remains constant with height or if the axis changes in a consistent fashion.

References

[1] Engel, D. *Energy Transition Outlook 2017: Renewables, Power and Energy Use Forecast to 2050*. Arnhem, The Netherlands, 2017.

[2] Philipps, S. and Warmuth, W. *Photovoltaics Report*. Freiburg, Germany, 2019.

[3] Yang, Y. M., Yu, A., Hsu, B., Hsu, W. C., Yang, A., and Lan, C. W. "Development of high-performance multicrystalline silicon for photovoltaic industry". *Progress in Photovoltaics: Research and Applications* 23 (3) (2015), pp. 340–351.

[4] Nelson, J. *The Physics of Solar Cells*. London, UK: ICP, 2003. Chap. 4, pp. 79–118.

[5] Van Zeghbroeck, B. *Principles of Semiconductor Devices. Carrier recombination and generation*. 2011. URL: `https://ecee.colorado.edu/~bart/book/book/chapter2/ch2_8.htm` (visited on 03/25/2019).

[6] Föll, H. *Defects in Crystals*. 2015. URL: `https://www.tf.uni-kiel.de/matwis/amat/def_en/index.html` (visited on 03/25/2019).

[7] Hull, D. and Bacon, D. J. *Introduction to dislocations*. 4th ed. Oxford, UK: Butterworth Heinemann, 2001. Chap. 1-4, 6-9.

[8] Smith, D. A. "Interaction of dislocations with grain boundaries". *J. Phys. Colloques* 43 (C6) (1982), pp. 225–237.

[9] Hielscher, R., Silbermann, C. B., and Schmidl, E. "Denoising of crystal orientation maps". *J. Appl. Crystallogr.-In Rev.* (2018).

[10] Humphreys, F. J. and Hatherly, M. *Recrystallization and Related Annealing Phenomena*. 2nd ed. Oxford, UK: Elsevier, 2004. Chap. 4, pp. 91–119.

[11] Kohyama, M., Yamamoto, R., and Doyama, M. "Structures and Energies of Symmetrical <011> Tilt Grain Boundaries in Silicon". *physica status solidi (b)* 137 (1) (1986), pp. 11–20.

[12] Brandon, D., Ralph, B., Ranganathan, S., and Wald, M. "A field ion microscope study of atomic configuration at grain boundaries". *Acta Metallurgica* 12 (7) (1964), pp. 813–821.

[13] Seibt, M. and Kveder, V. "Gettering Processes and the Role of Extended Defects". eng. *Advanced Silicon Materials for Photovoltaic Applications*. Ed. by Pizzini, S. 1st ed. United Kingdom: Wiley, 2012. Chap. 4.

[14] Donolato, C. “Modeling the effect of dislocations on the minority carrier diffusion length of a semiconductor”. *Journal of Applied Physics* 84 (5) (1998), pp. 2656–2664.

[15] Bentzen, A. and Holt, A. “Overview of phosphorus diffusion and gettering in multicrystalline silicon”. *Materials Science and Engineering: B* 159-160 (2009). EMRS 2008 Spring Conference Symposium K: Advanced Silicon Materials Research for Electronic and Photovoltaic Applications, pp. 228–234.

[16] Sopori, B. L., Chen, W., and Jones, K. “On the performance limiting behavior of defect clusters in commercial silicon solar cells”. *2nd World Conference and Exhibition on Photovoltaic Solar Energy Conversion*. Sept. 1998.

[17] Ryningen, B., Stokkan, G., Kivambe, M., Ervik, T., and Lohne, O. “Growth of dislocation clusters during directional solidification of multicrystalline silicon ingots”. *Acta Materialia* 59 (20) (2011), pp. 7703–7710.

[18] Ervik, T., Kivambe, M., Stokkan, G., Ryningen, B., and Lohne, O. “Dislocation formation at Σ=27a boundaries in multicrystalline silicon for solar cells”. *Proceedings of the 26th European Photovoltaic Solar Energy Conference and Exhibition, WIP-Munich*. Hamburg, Germany, 2011, pp. 1895–1899.

[19] Garg, A., Clark, W. A. T., and Hirth, J. P. “Dissociated and faceted large-angle coincident-site-lattice boundaries in silicon”. *Philosophical Magazine A* 59 (3) (1989), pp. 479–499.

[20] Stoffers, A. “Grain boundary segregation in multicrystalline silicon studied by correlative microscopy”. PhD thesis. Aachen, Germany: RWTH Aachen University, May 19, 2017.

[21] Oriwol, D. et al. “Small-angle subgrain boundaries emanating from dislocation pile-ups in multicrystalline silicon studied with synchrotron white-beam X-ray topography”. *Acta Materialia* 61 (18) (2013), pp. 6903–6910.

[22] Carl, E.-R., Danilewsky, A., Meissner, E., and Geiger, T. “Large- and small-angle grain boundaries in multi-crystalline silicon and implications for the evolution of grain boundaries during crystal growth”. *Journal of Applied Crystallography* 47 (6) (2014), pp. 1958–1965.

[23] Stokkan, G., Hu, Y., Mjøs, Ø., and Juel, M. “Study of evolution of dislocation clusters in high performance multicrystalline silicon”. *Solar Energy Materials and Solar Cells* 130 (2014), pp. 679–685.

[24] Trempa, M., Kupka, I., Kranert, C., Lehmann, T., Reimann, C., and Friedrich, J. “Evolution of grain structure and recombination active dislocations in extraordinary tall conventional and high performance multi-crystalline silicon ingots”. *Journal of Crystal Growth* 459 (2017), pp. 67–75.

[25] Chuang, L.-C., Maeda, K., Morito, H., Shiga, K., and Fujiwara, K. "Origin of small-angle grain boundaries during directional solidification in multicrystalline silicon". *Materialia* 3 (2018), pp. 347–352.

[26] Borrego, J. M., Gutmann, R. J., Jensen, N., and Paz, O. "Non-destructive lifetime measurement in silicon wafers by microwave reflection". *Solid-State Electronics* 30 (2) (1987), pp. 195–203.

[27] Sopori, B. L. "A New Defect Etch for Polycrystalline Silicon". *Journal of The Electrochemical Society* 131 (3) (1984), pp. 667–672.

[28] Föll, H. *Semiconductors I. Etching of Silicon*. 2015. URL: `https://www.tf.uni-kiel.de/matwis/amat/semi_en/kap_4/backbone/r4_2_1.html` (visited on 03/25/2019).

[29] Schwarzer, R. A., Field, D. P., Adams, B. L., Kumar, M., and Schwartz, A. J. *Electron backscatter diffraction in materials science*. 2nd ed. Springer, 2009. Chap. 1.

[30] Napchan, E. "Backscattered Electrons in the SEM". *Microscopy and Analysis* (2001), pp. 9–12.

[31] Morawiec, A. "Automatic orientation determination from Kikuchi patterns". *Journal of Applied Crystallography* 32 (4) (1999), pp. 788–798.

[32] Tjelmeland, H. *Enkel lineær regresjon*. 2017. URL: `https://wiki.math.ntnu.no/tma4245/tema/begreper/regression` (visited on 06/04/2019).

[33] Gupta, V. K. and Agnew, S. R. "A Simple Algorithm to Eliminate Ambiguities in EBSD Orientation Map Visualization and Analyses: Application to Fatigue Crack-Tips/Wakes in Aluminum Alloys". *Microscopy and Microanalysis* 16 (6) (2010), pp. 831–841.

[34] Humphreys, F. J., Bate, P. S., and Hurley, P. J. "Orientation averaging of electron backscattered diffraction data". *Journal of Microscopy* 201 (1) (2001), pp. 50–58.

[35] Godfrey, A. "Edge preservation near triple junctions during orientation averaging of EBSP data". *Scripta Materialia* 50 (8) (2004), pp. 1097–1101.

[36] Engler, O. and Randle, V. *Introduction to texture analysis: macrotexture, microtexture and orientation mapping*. 2nd ed. Boca Raton, FL, US: CRC press, 2010.

[37] Grimmer, H. "Disorientations and coincidence rotations for cubic lattices". *Acta Crystallographica Section A* 30 (6) (1974), pp. 685–688.

Appendices

A. Additional Work

- PCD-measurements
  - Overview scan of entire slabs for $\Sigma3\{1\,1\,1\}$, $\Sigma3\{1\,1\,2\}$, $\Sigma27\{5\,5\,2\}$, $\Sigma27\{1\,1\,5\}$ (4 slabs)
  - Higher magnification scan of each boundary (8 in total)
- Optical microscopy
  - Overview maps of defect etched samples at 2.5x magnification (stitched micrographs): all 8 boundaries (where $\Sigma27\{1\,1\,5\}$ I-II was mapped twice – once after each defect etch)
  - Point of interest micrographs of defect etched samples at 20x magnification (Points of interest were chosen based on the overview maps and the micrographs were taken prior to orientation mapping (while awaiting the Laue scanner to be back in order). These micrographs therefore turned out to be of little use in the final analyses.)
    - $\Sigma3\{1\,1\,1\}$
    - $\Sigma3\{1\,1\,2\}$ I-II
    - $\Sigma3\{1\,1\,2\}$ II-2B-2
    - $\Sigma27\{1\,1\,5\}$ I-II
    - $\Sigma27\{5\,5\,2\}$
- Photoscanner overview maps of defect etched samples
  - Entire slabs for $\Sigma3\{1\,1\,1\}$, $\Sigma3\{1\,1\,2\}$, $\Sigma27\{5\,5\,2\}$, $\Sigma27\{1\,1\,5\}$ (4 slabs) after first defect etch
  - Another scan of $\Sigma27\{1\,1\,5\}$ I-II after the second etch
- EBSD Orientation mapping: the majority of these results have been presented in the report to varying extents
- Matlab script for conversion of Laue grid-scan data files to .ang

B. Code

B.1. Macroscopic Disorientation Analysis

The following codes were used to generate the macroscopic disorientation data. Some of the functions must be called manually, while some are called by the manually called functions, these are: **DisorientationCalculator.m**, **MedianOrientationFinder.m**, **WindowSelection.m**, **PODOCalculator.m** and **PPDOCalculator.m**. The manually called functions should be called in the following sequence:

1. AngFileReader.m
2. FilterCI.m
3. RotationMatrixCalculator.m
4. DataSegmentationY.m
5. MedianFilter.m
6. GrainSegmentation.m
7. MacroscopicDisorientationFetch.m

B.1.1. AngFileReader.m

Listing B.1: Matlab script used for finding macroscopic disorientations. Reading the raw data.

```
% AngFileReader
% Taking an .ang file of orientation data and recreates the data
   matrix as
% a matlab variable

% Input data: .ang located in the "ang files" folder

% Output data: MxN array stored as a .mat variable in "mat files"
   folder
% M (:,N): different data points
% N=1: phi1 Euler angle
% N=2: PHI Euler angle
% N=3: phi2 Euler angle
% N=4: x coordinate
% N=5: y coordinate
% N=6: IQ value
% N=7: CI value
% N=8: Phase ID
% N=9: Detector intensity
% N=10: Fit

function AngFileReader()

% Finding .ang file
cd 'ang files'
files = dir;
fprintf('Available files:\n');
for i = 1:length(files)
    fprintf('%i: %s\n',i,files(i).name);
end
folderNum = input('Enter number of desired file:\n');
angFilename = files(folderNum).name;

file = fopen(angFilename,'r');
fprintf('Reading .ang file...\n');
```

```
% Counting data points
line = 1;
dataPointCount = 0;
while line ~= -1
    line = fgets(file);
    if line == -1 % Breaks the if before error message, loop will
       close thereafter
        continue
    elseif length(line) > 50 && contains(line,'#') == false
        dataPointCount = dataPointCount + 1;
    end
end
frewind(file)

% Reading data point information to matrix
array = NaN(dataPointCount,10);
line = 1;
index = 1;
while line ~= -1
    line = fgets(file);
    if line == -1 % Breaks the if before error message, loop will
       close thereafter
        continue
    elseif length(line) > 50 && contains(line,'#') == false
        array(index,1) = str2double(line(1:9)); % phi1
        array(index,2) = str2double(line(10:19)); % PHI
        array(index,3) = str2double(line(20:29)); % phi2
        array(index,4) = str2double(line(30:42)); % x
        array(index,5) = str2double(line(43:55)); % y
        array(index,6) = str2double(line(56:62)); % IQ
        array(index,7) = str2double(line(63:69)); % CI
        array(index,8) = str2double(line(70:72)); % PhaseID
        array(index,9) = str2double(line(73:79)); % Detector
           intensity
        array(index,10) = str2double(line(80:87)); % Fit
        index = index + 1;
```

```
    end
end
fclose(file);
cd ../


% Saving array
cd 'mat files'
filename = input('File has been read. Enter desired name of .mat
   file for variable storage (write ".ang" for same name as .ang)
   :\n','s');
if contains(filename,'.ang')
    filename = angFilename(1:end-4);
end
save(filename,'array');
fprintf('Array saved as %s.mat\n',filename);
cd ../
end % function
```

B.1.2. FilterCI.m

Listing B.2: Matlab script used for finding macroscopic disorientations. Confidence index filtering the data.

```
% FilterCI
% Taking in an array of orientation data and filtering it for CI
   values

% Input data: MxN array
% M (:,N): different data points
% N=1: phi1 Euler angle
% N=2: PHI Euler angle
% N=3: phi2 Euler angle
% N=4: x coordinate
% N=5: y coordinate
% N=6: IQ value
% N=7: CI value
% N=8: Phase ID
% N=9: Detector intensity
% N=10: Fit


% Output data: equally shaped array where Euler angles (N=1 to N
   =3) of
% below treshold CI value has been set to NaN


function angArrayFiltered = FilterCI(angArray)


CIlimit = input('Set CI treshold value between 0 and 1 (-1 for no
   filtering)\n');
if CIlimit >= 0 && CIlimit <= 1
    CIindices = transpose(find( (-1)*((angArray(:,7) > CIlimit)-1)
        ));
    angArrayFiltered = angArray;
    for i = CIindices
```

```
        angArrayFiltered(i,1:3) = NaN(1,3); % Replacing Euler
            angles of rows with sub-limit values with NaNs
    end
    amountReplaced = length(CIindices);
    fprintf('Filtering completed. %i rows with CI values smaller
        than or equal to %.2f replaced by NaNs.\n',amountReplaced,
        CIlimit);
else
    fprintf('No filtering\n');
end

end
```

B.1.3. RotationMatrixCalculator.m

Listing B.3: Matlab script used for finding macroscopic disorientations. Calculating the rotation matrix for each data point.

```
% RotationMatrixCalculator
% Taking in an array of orientation data and appends it with
   rotation
% matrix coefficients for each data point

% Input data: MxN array
% M (:,N): different data points
% N=1: phi1 Euler angle
% N=2: PHI Euler angle
% N=3: phi2 Euler angle
% N=4: x coordinate
% N=5: y coordinate
% N=6: IQ value
% N=7: CI value
% N=8: Phase ID
% N=9: Detector intensity
% N=10: Fit

% Output data: same array with appendements:
% N=11: g11
% N=12: g12
% N=13: g13
% N=14: g21
% N=15: g22
% N=16: g23
% N=17: g31
% N=18: g32
% N=19: g33


function appendedArray = RotationMatrixCalculator(array)

dataPoints = size(array,1);
phi1vec = array(:,1);
```

```
PHIvec = array(:,2);
phi2vec = array(:,3);

appendedArray = NaN(dataPoints,19);
appendedArray(:,1:10) = array;

for pointNum = 1:dataPoints
    % Formulas: Bunge page 21, Engler/Randle p 35
    appendedArray(pointNum,11) = cos(phi1vec(pointNum)) * cos(
       phi2vec(pointNum)) - sin(phi1vec(pointNum)) * sin(phi2vec(
       pointNum)) * cos(PHIvec(pointNum)); %g11
    appendedArray(pointNum,12) = sin(phi1vec(pointNum)) * cos(
       phi2vec(pointNum)) + cos(phi1vec(pointNum)) * sin(phi2vec(
       pointNum)) * cos(PHIvec(pointNum)); %g12
    appendedArray(pointNum,13) = sin(phi2vec(pointNum)) * sin(
       PHIvec(pointNum)); %g13
    appendedArray(pointNum,14) = -cos(phi1vec(pointNum)) * sin(
       phi2vec(pointNum)) - sin(phi1vec(pointNum)) * cos(phi2vec(
       pointNum)) * cos(PHIvec(pointNum)); %g21
    appendedArray(pointNum,15) = -sin(phi1vec(pointNum)) * sin(
       phi2vec(pointNum)) + cos(phi1vec(pointNum)) * cos(phi2vec(
       pointNum)) * cos(PHIvec(pointNum)); %g22
    appendedArray(pointNum,16) = cos(phi2vec(pointNum)) * sin(
       PHIvec(pointNum)); %g23
    appendedArray(pointNum,17) = sin(phi1vec(pointNum)) * sin(
       PHIvec(pointNum)); %g31
    appendedArray(pointNum,18) = -cos(phi1vec(pointNum)) * sin(
       PHIvec(pointNum)); %g32
    appendedArray(pointNum,19) = cos(PHIvec(pointNum)); %g33
end
end % function
```

B.1.4. DataSegmentationY.m

Listing B.4: Matlab script used for finding macroscopic disorientations. Preparing the data structure for upcoming functions.

```
% DataSegmentationY
% Taking in an array of orientation data and segmenting it in
   matrices for
% each y coordinate value

% Input data: MxN array
% M (:,N): different data points
% N=1: phi1 Euler angle
% N=2: PHI Euler angle
% N=3: phi2 Euler angle
% N=4: x coordinate
% N=5: y coordinate
% N=6: IQ value
% N=7: CI value
% N=8: Phase ID
% N=9: Detector intensity
% N=10: Fit
% N=11: g11
% N=12: g12
% N=13: g13
% N=14: g21
% N=15: g22
% N=16: g23
% N=17: g31
% N=18: g32
% N=19: g33

% Output data: MxNxO matrix stored as a .mat variable
% M (:,N,O): different x data points
% N=1: phi1 Euler angle
% N=2: PHI Euler angle
% N=3: phi2 Euler angle
% N=4: x coordinate
% N=5: y coordinate
```

```
% N=6: IQ value
% N=7: CI value
% N=8: Phase ID
% N=9: Detector intensity
% N=10: Fit
% N=11: g11
% N=12: g12
% N=13: g13
% N=14: g21
% N=15: g22
% N=16: g23
% N=17: g31
% N=18: g32
% N=19: g33
% O (M,N,:): different y data points

function newArray = DataSegmentationY(array)

% Finding the indices of the steps in y
% Necessary because length of x-coordinates not constant (
   alternates)
yStepIndices = [1];
for i = 2:size(array,1)
    if array(i,5) > array(i-1,5)
        yStepIndices(end+1) = i;
    end
end


ysteps = length(yStepIndices);
yStepIndicesExtended = [yStepIndices size(array,1)+1];
minXLength = min(yStepIndicesExtended(2:end)-yStepIndicesExtended
   (1:end-1));
maxXLength = max(yStepIndicesExtended(2:end)-yStepIndicesExtended
   (1:end-1));
newArray = NaN(maxXLength,19,ysteps); % pre-allocating
for i = 1:ysteps
```

```
    currentXLength = yStepIndicesExtended(i+1)-
       yStepIndicesExtended(i);
    newArray(1:currentXLength,:,i) = array(yStepIndicesExtended(i)
       :yStepIndicesExtended(i+1)-1,:);
end
end % function
```

B.1.5. MedianFilter.m

Listing B.5: Matlab script used for finding macroscopic disorientations. Median filter smoothing the data.

```
% MedianFilter
% Takes in a y-segmented array and applies the Median Filter to it
   , returns
% smoothed duplicate of the array

% Input data: MxNxO matrix
% M (:,N,O): different x data points
% N=1: phi1 Euler angle
% N=2: PHI Euler angle
% N=3: phi2 Euler angle
% N=4: x coordinate
% N=5: y coordinate
% N=6: IQ value
% N=7: CI value
% N=8: Phase ID
% N=9: Detector intensity
% N=10: Fit
% N=11: g11
% N=12: g12
% N=13: g13
% N=14: g21
% N=15: g22
% N=16: g23
% N=17: g31
% N=18: g32
% N=19: g33
% O (M,N,:): different y data points

% Output data: Same MxNxO matrix shape with N=1-3,11-19 replaced




function smoothedArray = MedianFilter(array)
```

```
NNs = input('Enter desired number of nearest neighbors per side of
    the candidate:\n');
smoothedArray = array; % Duplicating for pre-allocation

for i = 1:size(array,3) % Creating a window for each x position
   for all y positions (i)
    windowArray = WindowSelection(array(:,:,i),NNs);
    for j = 1:size(windowArray,3) % Finding desired new value for
       each x position (j)
        medianValues = MedianOrientationFinder(windowArray(:,:,j))
           ;
        smoothedArray(j,[1:3 11:19],i) = medianValues([1:3 11:19])
           ;
    end
    sumnans = sum(isnan(smoothedArray(:,1,i)));
%    if sumnans > 0
%        fprintf('Window size insufficiently large. %i NaNs
   detected for O=%i (y=%f) in smoothed array.\n',sumnans,i,
   smoothedArray(1,5,i));
%    end
end
fprintf('Smoothing completed\n');
end % function
```

B.1.6. GrainSegmentation.m

Listing B.6: Matlab script used for finding macroscopic disorientations. Finding the coordinates of grains.

```
% GrainSegmentation
% Finds peaks in the point-to-point misorientation, controls if
   the change
% in orientation is persistent and recognises the peak as a grain
   boundary if
% persisent. Returns the indices of the leftmost and rightmost
   pixel of
% each grain and the median orientation of each grain.

% Grains less than 3 pixels wide are ignored

% May fail to recognise the grain boundary if e.g. the ppdo has 3
   consecutive
% peaks, i.e. the podo goes a a a b a b b b b

% Input data: MxNxO matrix
% M (:,N,O): different x data points
% N=1: phi1 Euler angle
% N=2: PHI Euler angle
% N=3: phi2 Euler angle
% N=4: x coordinate
% N=5: y coordinate
% N=6: IQ value
% N=7: CI value
% N=8: Phase ID
% N=9: Detector intensity
% N=10: Fit
% N=11: g11
% N=12: g12
% N=13: g13
% N=14: g21
% N=15: g22
% N=16: g23
% N=17: g31
```

```
% N=18: g32
% N=19: g33
% O (M,N,:): different y data points


% Output 1: MxN index matrix with indices start and end of each
   grain in
% each y-segment
% M: y-segments
% N: indices (odd numbered = start-index, even numbered = end-
   index)

% Output 2: MxNxO grain orientation matrix with the median
   orientation of
% each grain specified in the index matrix
% M: different grains. (M=m,:,O=o) is the grain that corresponds
   to the index matrix
% as start (M=o, N=2m-1) and end (M=o,N=2m)
% N=1: phi1 Euler angle
% N=2: PHI Euler angle
% N=3: phi2 Euler angle
% N=4-10: NaNs
% N=11: g11
% N=12: g12
% N=13: g13
% N=14: g21
% N=15: g22
% N=16: g23
% N=17: g31
% N=18: g32
% N=19: g33
% O: different y segments

function [indexMatrix,grainOrientationMatrix] = GrainSegmentation(
   array)
```

```
threshold = 0.025; % radians
indexMatrix = NaN(size(array,3),1);
grainOrientationMatrix = NaN(1,12,size(array,3));
for i = 1:size(array,3)
    ppdo = PPDOCalculator(array(:,:,i));
    podo = PODOCalculator(array(:,:,i),1);
    indexVector = [1];
    % find values above treshold
    for j = 3:length(ppdo)-2 % do not check the outer edges (for
       signficance-check simplicity)
        controlMatrix = NaN(2);
        if ppdo(j) > threshold

            % significance check: control values up to 2 nearest
               neighbors
            % on each side if grain boundary or impulsive noise
            for k = 1:2
                for l = 1:2
                    disorientation = DisorientationCalculator(
                       array(j-k,:,i),array(j+l,:,i));
                    if disorientation > threshold
                        controlMatrix(k,l) = 1;
                    else
                        controlMatrix(k,l) = 0;
                    end
                end
            end
            if sum(sum(controlMatrix)) == 4 % accept grain
                indexVector(end+1) = j-1; % end of last grain
                indexVector(end+1) = j; % start of this grain
            end
        end
    end % j-for
    indexVector(end+1) = length(ppdo);

    % control that grain size is significant
    m = 3;
```

```
while m <= length(indexVector)
    if indexVector(m)-indexVector(m-2) < 3
        % remove detected boundary if grain is only 2 pixels
           wide
        temp = [indexVector(1:m-2) indexVector(m+1:end)];
        indexVector = temp;
        fprintf('Insignificant grain size. GB removed. (i = %i
           , m = %i)\n',i,m);
    else
        m = m+2;
    end
end

% Finding median orientations of grains
tempOrientationMatrix = zeros(length(indexVector)/2,12);
for n = 2:2:length(indexVector)
    medianArray = MedianOrientationFinder(array(indexVector(n
       -1):indexVector(n),:,i));
    tempOrientationMatrix(n/2,1:3) = medianArray(1:3);
    tempOrientationMatrix(n/2,4:12) = medianArray(11:19);
end

% Storing in output matrices
if size(indexMatrix,2) < length(indexVector) % expanding
   indexMatrix if necessary
    temp = indexMatrix;
    indexMatrix = NaN(size(array,3),length(indexVector));
    indexMatrix(:,1:size(temp,2)) = temp;
    indexMatrix(i,:) = indexVector;
else
    indexMatrix(i,1:length(indexVector)) = indexVector;
end
if size(grainOrientationMatrix,1) < size(tempOrientationMatrix
   ,1) % expanding grainOrientationMatrix if necessary
    temp = grainOrientationMatrix;
    grainOrientationMatrix = NaN(size(tempOrientationMatrix,1)
       ,12,size(array,3));
```

```
        grainOrientationMatrix(1:size(temp,1),1:12,:) = temp;
        grainOrientationMatrix(:,1:12,i) = tempOrientationMatrix;
    else
        grainOrientationMatrix(1:size(tempOrientationMatrix,1)
           ,1:12,i) = tempOrientationMatrix;
    end

    fprintf('%i y-segments segmented into grains. Grains found in
       last segment: %i\n',i,length(indexVector)/2);
end % i-for
end % function

% kontrollsjekken ikke i stand til ? akseptere korngrense-
   tilfeller hvor det er
% tre konsekutive peaks i ppdo og podo derfor g?r:  a a a b a b b
   b b
```

B.1.7. MacroscopicDisorientationFetch.m

Listing B.7: Matlab script used for finding macroscopic disorientations. Finding the disorientation between the main grains.

```
% MacroscopicDisorientationFetch
% Controls each grain if they are larger than a threshold value, which
% should be so large as to only give the two main crystals. Returns the
% disorientations between the median orientations of the two large grains detected.

% Input 1: MxN index matrix with indices start and end of each grain in
% each y-segment
% M: y-segments
% N: indices (odd numbered = start-index, even numbered = end-index)

% Input 2: MxNxO grain orientation matrix with the median orientation of
% each grain specified in the index matrix
% M: different grains. (M=m,:,O=o) is the grain that corresponds to the index matrix
% as start (M=o, N=2m-1) and end (M=o,N=2m)
% N=1: phi1 Euler angle
% N=2: PHI Euler angle
% N=3: phi2 Euler angle
% N=4-10: NaNs
% N=11: g11
% N=12: g12
% N=13: g13
% N=14: g21
% N=15: g22
% N=16: g23
% N=17: g31
% N=18: g32
% N=19: g33
```

```
% 0: different y segments

% Output: Vector with the disorientations for each y value

function disorientations = MacroscopicDisorientationFetch(
   indexMatrix,grainOrientationMatrix)

disorientations = NaN(1,size(indexMatrix,1));
grainIndices = NaN(size(indexMatrix,1),4);
requiredGrainSize = 50;
nMatrix = NaN(size(indexMatrix,1),2);
for i = 1:size(indexMatrix,1)
    n = 2;
    gi = 0; % numbers of grains larger than requiredGrainSize
       found for this segment
    while ~isnan(indexMatrix(i,n))
        grainSize = indexMatrix(i,n) - indexMatrix(i,n-1);
        if grainSize >= requiredGrainSize && gi == 0
            gi = gi+1;
            grainIndices(i,1:2) = indexMatrix(i,n-1:n);
            nMatrix(i,1) = n;
        elseif grainSize >= requiredGrainSize && gi == 1
            gi = gi+1;
            grainIndices(i,3:4) = indexMatrix(i,n-1:n);
            nMatrix(i,2) = n;
        elseif grainSize >= requiredGrainSize && gi >=2
            gi = gi+1;
            fprintf('More than 2 grains larger than required size
               found for i=%i\n',i);
        end
        n=n+2;
        if n > size(indexMatrix,2)
            break
        end
    end
    if gi < 2
```

```
        fprintf('Less than 2 grains larger than required size
            found for i=%i\n',i);
    end
end

for j = 1:size(indexMatrix,1)
    median1 = NaN(1,19);
    median2 = NaN(1,19);
    median1(1:3) = grainOrientationMatrix(nMatrix(j,1)/2,1:3,j);
    median1(11:19) = grainOrientationMatrix(nMatrix(j,1)/2,4:12,j)
        ;
    median2(1:3) = grainOrientationMatrix(nMatrix(j,2)/2,1:3,j);
    median2(11:19) = grainOrientationMatrix(nMatrix(j,2)/2,4:12,j)
        ;
    disorientations(j) = DisorientationCalculator(median1,median2)
        ;
end
end
```

B.1.8. DisorientationCalculator.m

Listing B.8: Matlab script used for finding macroscopic disorientations. Calculating the disorientation between two orientations.

```
% DisorientationCalculator
% Takes in two vectors of orientation data, generates the rotation
% matrices, calculates a misorientation angle and checks the 24
   symmetric
% solutions to find the disorientation angle. Returns a scalar
% disorientation angle in radians

% Input data: 2 1xN arrays
% N=1: phi1 Euler angle
% N=2: PHI Euler angle
% N=3: phi2 Euler angle
% N=4: x coordinate
% N=5: y coordinate
% N=6: IQ value
% N=7: CI value
% N=8: Phase ID
% N=9: Detector intensity
% N=10: Fit
% N=11: g11
% N=12: g12
% N=13: g13
% N=14: g21
% N=15: g22
% N=16: g23
% N=17: g31
% N=18: g32
% N=19: g33

% Output data: disorientation angle in radians

function disorientation = DisorientationCalculator(orientation1,
   orientation2)

if isnan(orientation1(1)) || isnan(orientation2(1))
```

```
    disorientation = NaN;
else
    % Creating the 24 symmetry operators for the
       crystallographically related
    % solutions
    % Matrices from Engler/Randle p. 381
    T = zeros(3,3,24);

    T(:,:,1) = [1 0 0; 0 1 0; 0 0 1];
    T(:,:,2) = [0 0 -1; 0 -1 0; -1 0 0];
    T(:,:,3) = [0 0 -1; 0 1 0; 1 0 0];
    T(:,:,4) = [-1 0 0; 0 1 0; 0 0 -1];

    T(:,:,5) = [0 0 1; 0 1 0; -1 0 0];
    T(:,:,6) = [1 0 0; 0 0 -1; 0 1 0];
    T(:,:,7) = [1 0 0; 0 -1 0; 0 0 -1];
    T(:,:,8) = [1 0 0; 0 0 1; 0 -1 0];

    T(:,:,9) = [0 -1 0; 1 0 0; 0 0 1];
    T(:,:,10) = [-1 0 0; 0 -1 0; 0 0 1];
    T(:,:,11) = [0 1 0; -1 0 0; 0 0 1];
    T(:,:,12) = [0 0 1; 1 0 0; 0 1 0];

    T(:,:,13) = [0 1 0; 0 0 1; 1 0 0];
    T(:,:,14) = [0 0 -1; -1 0 0; 0 1 0];
    T(:,:,15) = [0 -1 0; 0 0 1; -1 0 0];
    T(:,:,16) = [0 1 0; 0 0 -1; -1 0 0];

    T(:,:,17) = [0 0 -1; 1 0 0; 0 -1 0];
    T(:,:,18) = [0 0 1; -1 0 0; 0 -1 0];
    T(:,:,19) = [0 -1 0; 0 0 -1; 1 0 0];
    T(:,:,20) = [0 1 0; 1 0 0; 0 0 -1];

    T(:,:,21) = [-1 0 0; 0 0 1; 0 1 0];
    T(:,:,22) = [0 0 1; 0 -1 0; 1 0 0];
    T(:,:,23) = [0 -1 0; -1 0 0; 0 0 -1];
    T(:,:,24) = [-1 0 0; 0 0 -1; 0 -1 0];
```

```
% Generating rotation matrices
g11 = orientation1(1,11);
g12 = orientation1(1,12);
g13 = orientation1(1,13);
g21 = orientation1(1,14);
g22 = orientation1(1,15);
g23 = orientation1(1,16);
g31 = orientation1(1,17);
g32 = orientation1(1,18);
g33 = orientation1(1,19);

Ori1 = [g11, g12, g13; g21, g22, g23; g31, g32, g33];

g11 = orientation2(1,11);
g12 = orientation2(1,12);
g13 = orientation2(1,13);
g21 = orientation2(1,14);
g22 = orientation2(1,15);
g23 = orientation2(1,16);
g31 = orientation2(1,17);
g32 = orientation2(1,18);
g33 = orientation2(1,19);

Ori2 = [g11, g12, g13; g21, g22, g23; g31, g32, g33];


% Calculating the misorientation matrices
MisRM = NaN(3,3,24*24);
counter = 1;
for i = 1:24
    for j = 1:24
        TOri1 = T(:,:,i)*Ori1;
        TOri2 = T(:,:,j)*Ori2;
        MisRM(:,:,counter) = TOri1 \ TOri2;
        counter = counter + 1;
    end
```

```
    end

    % Calculating misorientation angles
    % Formulas from Engler/Randle p. 41
    misorientations = NaN(1,24*24);
    for i = 1:24*24
        misorientations(1,i) = acos(0.5 * (MisRM(1,1,i) + MisRM
           (2,2,i) + MisRM(3,3,i) - 1));
    end

    % Choosing the disorientation angle
    disorientation = min(misorientations);
end
end % function
```

B.1.9. MedianOrientationFinder.m

Listing B.9: Matlab script used for finding macroscopic disorientations. Finds the median orientation in a window.

```
% MedianOrientationFinder
% Takes in an array (representing the data points in a window),
   calculates
% the disorientations between all data points, finds the median
   orientation
% and returns the data of the data point selected as the median

% Input data: MxN array
% M (:,N): different x data points inside a window
% N=1: phi1 Euler angle
% N=2: PHI Euler angle
% N=3: phi2 Euler angle
% N=4: x coordinate
% N=5: y coordinate
% N=6: IQ value
% N=7: CI value
% N=8: Phase ID
% N=9: Detector intensity
% N=10: Fit
% N=11: g11
% N=12: g12
% N=13: g13
% N=14: g21
% N=15: g22
% N=16: g23
% N=17: g31
% N=18: g32
% N=19: g33

% Output data: 1xN array with data point representing the median
   orientation
% N=1: phi1 Euler angle
% N=2: PHI Euler angle
% N=3: phi2 Euler angle
```

```
% N=4: x coordinate
% N=5: y coordinate
% N=6: IQ value
% N=7: CI value
% N=8: Phase ID
% N=9: Detector intensity
% N=10: Fit
% N=11: g11
% N=12: g12
% N=13: g13
% N=14: g21
% N=15: g22
% N=16: g23
% N=17: g31
% N=18: g32
% N=19: g33


function medianArray = MedianOrientationFinder(singleWindowArray)


arraySize = size(singleWindowArray,1);
centerIndex = ceil(arraySize/2);
disorientationMatrix = NaN(arraySize-1); % pre-allocating


if sum(~isnan(singleWindowArray(:,1))) > 2
    % Calculate disorientations between all data points and store
       in an upper
    % triangular matrix. Only if at least 3 values in the window
       are non-NaN

    for i = 1:arraySize-1
        for j = i+1:arraySize
            if isnan(singleWindowArray(i,1)) || isnan(
               singleWindowArray(j,1))
                disorientationMatrix(i,j-1) = NaN;
```

```
            else
                disorientation = DisorientationCalculator(
                    singleWindowArray(i,:),singleWindowArray(j,:));
                disorientationMatrix(i,j-1) = disorientation;
            end
        end
    end


    % Calculate the sums of disorientations for each data point
    disorientationSums = NaN(1,arraySize);

    % First sum
    row = disorientationMatrix(1,:);
    nancheck = sum(~isnan(row)); % Check if this data point is a
        NaN
    if nancheck == 0
        disorientationSums(1) = NaN;
    else
        disorientationSums(1) = sum(row(~isnan(row)));
    end

    % Second to second to last sum
    for i = 2:arraySize-1
        row = disorientationMatrix(i,:);
        col = transpose(disorientationMatrix(:,i-1));
        rowcol = [row col];
        nancheck = sum(~isnan(rowcol)); % Check if this data point
            is a NaN
        if nancheck == 0
            disorientationSums(i) = NaN;
        else
            disorientationSums(i) = sum(rowcol(~isnan(rowcol)));
        end
    end

    % Last sum
```

```
    col = transpose(disorientationMatrix(:,arraySize-1));
    nancheck = sum(~isnan(col)); % Check if this data point is a
       NaN
    if nancheck == 0
        disorientationSums(arraySize) = NaN;
    else
        disorientationSums(arraySize) = sum(col(~isnan(col)));
    end


    % Find the index of the lowest sum
    [~, index] = min(disorientationSums);



elseif sum(~isnan(singleWindowArray(:,1))) == 2 % If only 2 values
    in the window are non-NaN
    indices = find(~isnan(singleWindowArray(:,1)));
    xdiff1 = abs(indices(1) - centerIndex);
    xdiff2 = abs(indices(2) - centerIndex);
    if xdiff1 > xdiff2 % distinguish by distance
        index = indices(2);
    elseif xdiff1 < xdiff2 % distinguish by distance
        index = indices(1);
    elseif xdiff1 == xdiff2 % distinguish by CI
        CIdiff = singleWindowArray(indices(1),7) -
           singleWindowArray(indices(2),7);
        if CIdiff > 0
            index = indices(1);
        else
            index = indices(2);
        end
    end
    fprintf('Candidate (x=%f, y=%f) surrounded by too many NaNs. 2
        valid values found in the window. Value closest in x
       distance chosen as median value.\n',...
```

```
        singleWindowArray(centerIndex,4),singleWindowArray(
            centerIndex,5));

elseif sum(~isnan(singleWindowArray(:,1))) == 1 % If only 1 value
    in the window is non-Nan
     index = find(~isnan(singleWindowArray(:,1))); % Set the only
        available value for the candidate
     fprintf('Candidate (x=%f, y=%f) surrounded by too many NaNs. 1
         valid value was found in the window and chosen as median
        value.\n',...
         singleWindowArray(centerIndex,4),singleWindowArray(
            centerIndex,5));

elseif sum(~isnan(singleWindowArray(:,1))) == 0 % If no values in
    the window are non-Nan
     index = centerIndex; % Leave the candidate unchanged as a NaN
     fprintf('Candidate (x=%f, y=%f) surrounded by NaNs only,
        consider increasing window size.\n',...
         singleWindowArray(centerIndex,4),singleWindowArray(
            centerIndex,5));
end %if


% Return this array
medianArray = singleWindowArray(index,:);

end %function
```

B.1.10. WindowSelection.m

Listing B.10: Matlab script used for finding macroscopic disorientations. Restructures a data set into windows.

```
% WindowSelection
% Takes in an array of orientation data istropic in y (!) and
   selects data
% points inside a window around each candidate data point

% Input data 1: MxN array
% M (:,N): different data points in x
% N=1: phi1 Euler angle
% N=2: PHI Euler angle
% N=3: phi2 Euler angle
% N=4: x coordinate
% N=5: y coordinate
% N=6: IQ value
% N=7: CI value
% N=8: Phase ID
% N=9: Detector intensity
% N=10: Fit
% N=11: g11
% N=12: g12
% N=13: g13
% N=14: g21
% N=15: g22
% N=16: g23
% N=17: g31
% N=18: g32
% N=19: g33

% Input data 2: Number of nearest neighbors on each side of the
   candidate

% Output data: MxNxO array
% M (:,N,O): different x data points inside a window
% N=1: phi1 Euler angle
% N=2: PHI Euler angle
```

```
% N=3: phi2 Euler angle
% N=4: x coordinate
% N=5: y coordinate
% N=6: IQ value
% N=7: CI value
% N=8: Phase ID
% N=9: Detector intensity
% N=10: Fit
% N=11: g11
% N=12: g12
% N=13: g13
% N=14: g21
% N=15: g22
% N=16: g23
% N=17: g31
% N=18: g32
% N=19: g33
% O (M,N,:): windows around different x candidates

% Candidate is always M = #(nearest neighbors)+1 (i.e. center of M
   -length)

function windowArray = WindowSelection(array,NNs)
dataPoints = size(array,1);
windowArray = NaN(2*NNs+1,19,dataPoints);
for i = 1:dataPoints % each candidate
    if i <= NNs % left side boundary condition
        overshootingPoints = NNs+1-i;
        windowArray(overshootingPoints+1:2*NNs+1,:,i) = array(1:i+
           NNs,:);
    elseif dataPoints-i < NNs % right side boundary condition
        overshootingPoints = i+NNs-dataPoints;
        windowArray(1:2*NNs+1-overshootingPoints,:,i) = array(i-
           NNs:i+NNs-overshootingPoints,:);
    else
        windowArray(:,:,i) = array(i-NNs:i+NNs,:);
    end
```

```
end % i-for
end % function
```

B.1.11. PODOCalculator.m

Listing B.11: Matlab script used for finding macroscopic disorientations. Calculates the point-to-origin disorienations for an array for a given origin.

```
% PODOCalculator
% Take an array isoptropic in y(!) and calculate the point-to-
   origin
% disorientation angles for the array

% Input data: MxN array
% M (:,N): different data points in x
% N=1: phi1 Euler angle
% N=2: PHI Euler angle
% N=3: phi2 Euler angle
% N=4: x coordinate
% N=5: y coordinate
% N=6: IQ value
% N=7: CI value
% N=8: Phase ID
% N=9: Detector intensity
% N=10: Fit
% N=11: g11
% N=12: g12
% N=13: g13
% N=14: g21
% N=15: g22
% N=16: g23
% N=17: g31
% N=18: g32
% N=19: g33

% Output data: 1xN array
% N: disorientation value between N and N_origin

function podoVector = PODOCalculator(array,origin)
%str = sprintf('Enter number between 1 and %i to set origin\n',
   size(array,1));
%while origin < 0
```

```
%     origin = input(str);
%     if isnan(array(origin,1))
%         fprintf('Origin is NaN, choose again\n');
%         origin = -1;
%     end
%end

if origin > size(array,1) && origin < 1
    str = sprintf('Enter number between 1 and %i to set origin\n',
       size(array,1));
end

podoVector = zeros(1,size(array,1));
for i = 1:size(array,1)
    if i == origin
        podoVector(i) = 0;
    elseif isnan(array(i,1))
        podoVector(i) = NaN;
    else
        podoVector(i) = DisorientationCalculator(array(i,:),array(
           origin,:));
    end
end
end%function
```

B.1.12. PPDOCalculator.m

Listing B.12: Matlab script used for finding macroscopic disorientations. Calculates the point-to-point disorienations for an array.

```
% PPDOCalculator
% Take an array isoptropic in y(!) and calculate the point-to-
   point
% disorientation angles for the array

% Input data: MxN array
% M (:,N): different data points in x
% N=1: phi1 Euler angle
% N=2: PHI Euler angle
% N=3: phi2 Euler angle
% N=4: x coordinate
% N=5: y coordinate
% N=6: IQ value
% N=7: CI value
% N=8: Phase ID
% N=9: Detector intensity
% N=10: Fit
% N=11: g11
% N=12: g12
% N=13: g13
% N=14: g21
% N=15: g22
% N=16: g23
% N=17: g31
% N=18: g32
% N=19: g33

% Output data: 1xN array
% N: disorientation value between N and N-1

function ppdoVector = PPDOCalculator(array)

ppdoVector = zeros(1,size(array,1));
for i = 2:size(array,1)
```

```
    if isnan(array(i,1)) || isnan(array(i-1,1))
        ppdoVector(i) = NaN;
    else
        ppdoVector(i) = DisorientationCalculator(array(i,:),array(
           i-1,:));
    end
end
end % function
```

B.2. EBSDCustomScanGenerator.m

Listing B.13: Matlab script for producing setting file for EBSD custom scans.

```
% EBSD Custom scan generator
% Do all alignments of the sample in the EBSD prior to using the
   script and find the stage positions indicating the desired scan
    area
% Enter xstep, ystep, xstart, ystart, xsize, ysize values to match
    desired scan area values
% The timePerPointEstimate variable may be changed on the basis of
    empirical observations
% The example values below covers the area x=(15200,...,35200) y
   =(1000,...,68000)
% Load the produced file in the OIM DC software when starting a
   Custom scan

clear all

xstep = 100; % microns
ystep = 500; % microns
xstart = 15200; % microns, moving positively
ystart = 1000; % microns, moving positively
xsize = 20000; % microns
ysize = 67000; % microns
timePerPointEstimate = 6; % seconds

if xsize/xstep ~= floor(xsize/xstep)
    xmultiples = floor(xsize/xstep);
    xdiff = multiples - xsize;
    xsize = xsize - diff;
end
if ysize/ystep ~= floor(ysize/ystep)
    ymultiples = floor(ysize/ystep);
    ydiff = multiples - ysize;
    ysize = ysize - diff;
end
```

```
datestring = datestr(datetime('now'));
filename = strcat('CustomScan ',datestring(1:14),datestring(16:17)
   ,datestring(19:20),'.txt');
fileID = fopen(filename,'w');

for i = 0:(ysize/ystep)
    for j = 0:(xsize/xstep)
        x = xstart + xstep*j;
        y = ystart + ystep*i;
        fprintf(fileID,'sx \t %i \t sy \t %i \t bx \t 0 \t by 0 \t
            rx \t %i \t ry \t %i \t\n',x,y,x,y);
    end
end
fclose(fileID);
dataPoints = (i+1)*(j+1);
sumsec = timePerPointEstimate * dataPoints;
if sumsec > 3600
    timelapsed = hours(seconds(sumsec));
    timestring = 'hours';
elseif sumsec > 60
    timelapsed = minutes(seconds(sumsec));
    timestring = 'minutes';
else
    timelapsed = sumsec;
    timestring = 'seconds';
end
fprintf('File written, %i data points, expected duration %.2f %s \
   n',(i+1)*(j+1),timelapsed,timestring);
```

B.3. Error Estimation

B.3.1. ErrorEstimationRegression.m

Listing B.14: Matlab script used for making the regressions of disorientation profiles.

```
% ErrorEstimationRegression
% Makes the regression and exports the regression data


function ErrorEstimationRegression()
clear all
close all

%load('strings accepted horizontal.mat');
%load('strings accepted vertical.mat');
strings{1} = 'mono/horizontal bottom.txt';
strings{2} = 'mono/horizontal center.txt';
strings{3} = 'mono/horizontal top.txt';
strings{4} = 'mono/vertical center.txt';
strings{5} = 'mono/vertical left.txt';
strings{6} = 'mono/vertical right.txt';

f = fopen('results.txt','w');
fprintf(f,'Col 1: Profile\n');
fprintf(f,'Col 2: n\n');
fprintf(f,'Col 3: b0_pp (deg)\n');
fprintf(f,'Col 4: b1_pp (deg/mm)\n');
fprintf(f,'Col 5: b0_po (deg)\n');
fprintf(f,'Col 6: b1_po (deg/mm)\n');
fprintf(f,'Col 7: s2_pp (deg^2)\n');
fprintf(f,'Col 8: s_pp (deg)\n');
fprintf(f,'Col 9: s2_po (deg^2)\n');
fprintf(f,'Col 10: s_po (deg)\n');
fprintf(f,'Col 11: R2_pp\n');
fprintf(f,'Col 12: R2_po\n');
for s = 1:length(strings)
    clearvars -except strings f s
    table = readtable(strings{s});
```

```
n = size(table,1)-3;

% Create array with distance values. Padded with ones for
   regression.
x = zeros(n,1);
cells = table{:,1};
for i = 1:n
    x(i) = str2double(cells{i}); % Distance from origin,
       microns
end
X = [ones(n,1) x];

% Create array with misorientation values
y_pp(:,1) = table{1:n,2}; % Point-to-point misorientation,
   degrees
y_po(:,1) = table{1:n,3}; % Point-to-origin misorientation,
   degrees

% Do regression for y = b0 + b1*x
b_pp = X\y_pp; % first value b0, second b1
b_po = X\y_po; % first value b0, second b1

% Calculate trendlines
trend_pp = X*b_pp;
trend_po = X*b_po;

% Calculate probability maximation estimators
SSE_pp = sum((y_pp-trend_pp).^2);
SST_pp = sum((y_pp-mean(y_pp)).^2);
R2_pp = 1-SSE_pp/SST_pp;
s2_pp = SSE_pp/(n-2);
s_pp = sqrt(s2_pp);

SSE_po = sum((y_po-trend_po).^2);
SST_po = sum((y_po-mean(y_po)).^2);
R2_po = 1-SSE_po/SST_po;
```

```
    s2_po = SSE_po/(n-2);
    s_po = sqrt(s2_po);

    % Write to file
    fprintf(f,'%25s; \t %i; \t %.4f; \t %.4f; \t %.4f; \t %.4f; \t
        %.4f; \t %.4f; \t %.4f; \t %.4f; \t %.4f; \t %.4f;\n',...
                strings{s},n,b_pp(1),b_pp(2)*1e3,b_po(1),b_po(2)*1
                   e3,s2_pp,s_pp,s2_po,s_po,R2_pp,R2_po);

    % Plot
    figure(s)
    plot(x,y_pp)
    hold on
    plot(x,y_po)
    plot(x,trend_pp)
    plot(x,trend_po)
    title(strings{s})
end %for
fclose(f);
end
```

B.3.2. ErrorEstimation.m

Listing B.15: Matlab script used for finding the statistical values of the regressions.

```
% ErrorEstimation
% Load result data from ErrorEstimationRegression and find the
   values of
% interest

clear all
tableH = readtable('results horizontal.txt');
tableV = readtable('results vertical.txt');
tablemono = readtable('results mono.txt');

b1_po_h = tableH{:,6};
b1_po_v = tableV{:,6};
s2_po = [tableH{:,9}; tableV{:,9}];
b1_po_h_mono = tablemono{1:3,6};
b1_po_v_mono = tablemono{4:6,6};
s2_po_mono = tablemono{:,9};

fprintf('b1_po_h mean \t = %.4f deg/mm\n',mean(b1_po_h));
fprintf('b1_po_h median \t = %.4f deg/mm\n',median(b1_po_h));
fprintf('b1_po_h max \t = %.4f deg/mm\n',max(b1_po_h));
fprintf('b1_po_h min \t = %.4f deg/mm\n',min(b1_po_h));
fprintf('b1_po_h var \t = %.4f deg^2/mm^2\n',var(b1_po_h));
fprintf('b1_po_h std \t = %.4f deg/mm\n',std(b1_po_h));

fprintf('b1_po_v mean \t = %.4f deg/mm\n',mean(b1_po_v));
fprintf('b1_po_v median \t = %.4f deg/mm\n',median(b1_po_v));
fprintf('b1_po_v max \t = %.4f deg/mm\n',max(b1_po_v));
fprintf('b1_po_v min \t = %.4f deg/mm\n',min(b1_po_v));
fprintf('b1_po_v var \t = %.4f deg^2/mm^2\n',var(b1_po_v));
fprintf('b1_po_v std \t = %.4f deg/mm\n',std(b1_po_v));

fprintf('s2_po mean \t = %.4f deg^2\n',mean(s2_po));
fprintf('s2_po median \t = %.4f deg^2\n',median(s2_po));
fprintf('s2_po max \t = %.4f deg^2\n',max(s2_po));
fprintf('s2_po min \t = %.4f deg^2\n',min(s2_po));
```

```
fprintf('s2_po var \t = %.4f deg^4\n',var(s2_po));
fprintf('s2_po std \t = %.4f deg^2\n',std(s2_po));

fprintf('b1_po_h_mono mean \t = %.4f deg/mm\n',mean(b1_po_h_mono))
   ;
fprintf('b1_po_h_mono median \t = %.4f deg/mm\n',median(
   b1_po_h_mono));
fprintf('b1_po_h_mono max \t = %.4f deg/mm\n',max(b1_po_h_mono));
fprintf('b1_po_h_mono min \t = %.4f deg/mm\n',min(b1_po_h_mono));
fprintf('b1_po_h_mono var \t = %.4f deg^2/mm^2\n',var(b1_po_h_mono
   ));
fprintf('b1_po_h_mono std \t = %.4f deg/mm\n',std(b1_po_h_mono));

fprintf('b1_po_v_mono mean \t = %.4f deg/mm\n',mean(b1_po_v_mono))
   ;
fprintf('b1_po_v_mono median \t = %.4f deg/mm\n',median(
   b1_po_v_mono));
fprintf('b1_po_v_mono max \t = %.4f deg/mm\n',max(b1_po_v_mono));
fprintf('b1_po_v_mono min \t = %.4f deg/mm\n',min(b1_po_v_mono));
fprintf('b1_po_v_mono var \t = %.4f deg^2/mm^2\n',var(b1_po_v_mono
   ));
fprintf('b1_po_v_mono std \t = %.4f deg/mm\n',std(b1_po_v_mono));

fprintf('s2_po_mono mean \t = %.4f deg^2\n',mean(s2_po_mono));
fprintf('s2_po_mono median \t = %.4f deg^2\n',median(s2_po_mono));
fprintf('s2_po_mono max \t = %.4f deg^2\n',max(s2_po_mono));
fprintf('s2_po_mono min \t = %.4f deg^2\n',min(s2_po_mono));
fprintf('s2_po_mono var \t = %.4f deg^4\n',var(s2_po_mono));
fprintf('s2_po_mono std \t = %.4f deg^2\n',std(s2_po_mono));

% Using the following found values for the report:
% b1_horizontal = mean(b1_po_h) = 1.1754 deg/mm
% b1_vertical = mean(b1_po_v) = 1.7024 deg/mm
% s2 = mean(s2_po) = 0.0299 deg^2 => s = 0.1729 deg => 99.6%
   values are
% within +/- 3*0.1729 deg = 0.5187 deg
```

```
% mono values:
% b1_h mean = 0.1497 deg/mm
% b1_v mean = 1.9557 deg/mm
% s2 mean = 0.0317 deg^2
```